THESIS FOR THE DEGREE OF LICENTIATE OF ENGINEERING

Nanoplasmonic hydrogen sensors for technologically relevant environments

ATHANASIOS THEODORIDIS

Department of Physics

CHALMERS UNIVERSITY OF TECHNOLOGY

Gothenburg, Sweden 2025

Nanoplasmonic hydrogen sensors for technologically relevant environments
ATHANASIOS THEODORIDIS

Department of Physics
Chalmers University of Technology
SE-412 96 Gothenburg
Sweden
Telephone + 46 (0)31-772 1000

Cover:
Light coupled from an optical fiber shines onto a metallic nanodisk. The nanodisk is surrounded by molecules such as H_2, O_2 and H_2O. The image of a cog and a brain represent the two aspects in this thesis: materials' engineering and neural network-based data analysis.

Printed by Chalmers Digitaltryck
Gothenburg, Sweden 2025

"You miss 100% of the shots you don't take. - Wayne Gretzky"

- *Michael Scott*

Abstract

The high flammability of hydrogen (H_2) when mixed with air makes H_2 sensors crucial in the development of hydrogen energy technologies across the Globe. Their development follows standards, in the form of performance metrics, with the most stringent and well-known ones established by the U.S. Department of Energy. Despite extensive research, key targets, such as the 1-second response time in 1000 ppm H_2, remain challenging, often achieved only in ideal environmental conditions. Additionally, the influence of poisoning gas species (such as CO,CO_2, NO_x) in general and humidity in particular are rarely addressed. Among the plethora of different H_2 sensing technologies nanoplasmonic optical sensors stand out as particularly promising. They rely on spectral shifts or intensity changes of the localized surface plasmon resonance of hydrogen-sorbing metal nanoparticles as the signal transduction scheme and have been boosted by advances in nanofabrication and the implementation of tailored nanostructured materials. Beyond materials engineering, advanced data analysis methods, such as the use of artificial intelligence (AI) that can greatly enhance data processing, are a to-date widely unexplored yet highly promising approach to improving the performance metrics of plasmonic hydrogen sensors. In this thesis, I apply both strategies and present three projects that aim to address both the response time and the humidity performance metric of plasmonic H_2 sensors. In the first study (**Paper I**), we demonstrate a Pt-based catalytic-nanoplasmonic H_2 sensor that can operate within 0-80% relative humidity (RH) and can detect concentrations as low as 600 ppm in air, at T≥ 50 ºC, while also exhibiting a decrease in the limit of detection with increasing humidity. In the second study (**Paper II**), we demonstrate the use of a tailored neural network ensemble model and showcase its ability to accelerate the response of a PdAu alloy nanoplasmonic H_2 sensor by a factor of 40 by eliminating the H_2 concentration/response time dependence. In the third study (**Paper III**) we employ a deep dense neural network to analyze data acquired from a PdAu alloy nanoplasmonic sensor operating under varying humidity (0-80% RH). With this AI-based treatment, we can eliminate the negative influence of H_2O in the sensor's response and achieve a limit of detection of 100 ppm at the highest measured 80 % RH.

List of Appended Papers

This thesis is based on the following appended papers:

Paper I: Theodoridis, A., Andersson, C., Nilsson, S. & Langhammer, C. A Catalytic-Plasmonic Pt Nanoparticle Sensor for Hydrogen Detection in High Humidity Environments. (In manuscript)

Paper II: Martvall, V., Moberg, H. K., **Theodoridis, A.**, Tomeček, D., Ekborg-Tanner, P., Nilsson, S., Volpe, G., Erhart, P. & Langhammer, C. Accelerating Plasmonic Hydrogen Sensors for Inert Gas Environments by Transformer-Based Deep Learning. *ACS Sensors* **2025**, 10 (1), 376-386

Paper III: Tomeček, D., Moberg, H. K., Nilsson, S., **Theodoridis, A.**, Darmadi, I., Midtvedt, D., Volpe, G., Andersson, O. & Langhammer, C. Neural network enabled nanoplasmonic hydrogen sensors with 100 ppm limit of detection in humid air. *Nature Communications* **2024**, 15, 1208

My Contribution to Appended Papers

Paper I: I performed the sensor nanofabrication, all the hydrogen-related measurements (sensor performance, long-term stability measurement, titration measurements), QMS measurements and SEM imaging. I wrote the manuscript together with Christoph Langhammer.

Paper II: I performed the sensor nanofabrication and did the hydrogenation measurements (pulses and simulated gradual leaks) together with David Tomeček. I have written the "Hydrogen Sensing Experiments" and "Sample Fabrication" sections in Methods. I have also written the "Hydrogenation protocols" and "Experimental Setup" in the Supporting Information.

Paper III: I performed the long-term stability measurements depicted in Figures 6-8 together with Sara Nilsson and David Tomeček.

Contents

1 Introduction

The concept of a world powered by renewable energy, such as hydrogen (H_2), was early envisioned in 1923 by geneticist J. B. S. Haldane, who believed that 400 years into the future, England will be covered in wind farms that supply energy to power stations, which in turn produce H_2 through electrolysis[1]. However it wasn't until 1972[2,3] that the term "hydrogen economy" first emerged and was coined by John Bockris.

H_2 itself has been used in several different ways in history; from lighting in the early 1800s, to heating and transportation the following century (which led to the infamous Hindenburg disaster in 1937), to powering NASA's spacecrafts in the mid-20[th] century. Nowadays H_2 is commonly used in many important industries, such as ammonia production or steel manufacturing, to name a few.

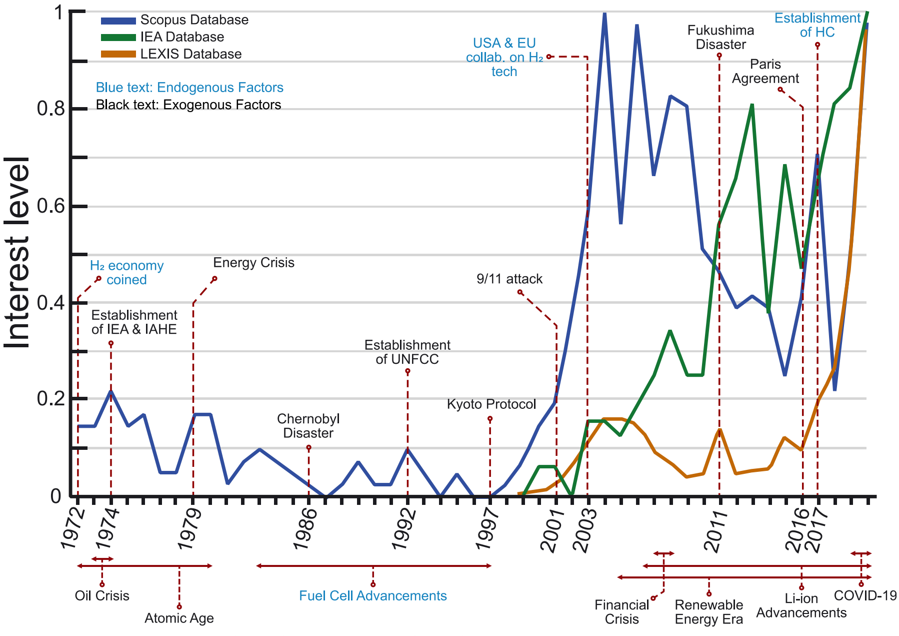

Figure 1: *Normalized interest level in H_2 over the years, based on publications from 3 different databases; The Scopus database analyzes the research trends in peer-reviewed academic literature. The IEA database evaluates industrial perspectives, and the LEXIS database covers international media (newspapers, press releases, web publications) (adapted from ref.*[4]).

Over the past couple of decades public interest in the hydrogen economy has grown significantly (**Figure 1**). This interest has been accompanied by parallel advancements in H_2 production methods, storage and transportation infrastructure, safety protocols and policies, as well as technological solutions. Among these, safety considerations are particularly critical, since the immediate hazards associated with H_2 gas, along with the potential environmental impacts of its increasing global use, should remain a top priority for stakeholders.

1.1 Why H_2 sensors?

The Hindenburg disaster is perhaps the most devastating and well-known incident involving H_2. The leading theory attributes the disaster to static electricity igniting leaked H_2 gas, which highlights the inherent risks associated with H_2. The reason for the ignition is that H_2 has a wide flammability (4-75%) and explosivity (13-65%) range, when mixed with air[5,6]. More importantly, the minimum ignition energy (in air) is only 0.02 mJ, i.e., low enough for a static discharge to ignite the gas.

For reference, methane and petrol both require an order of magnitude higher ignition energy than H_2[6]. Furthermore, H_2 is odorless, colorless and significantly prone to leakage due to its high diffusion coefficient and tiny size. Finally, the indirect warming impacts of H_2 emitted into the atmosphere have sporadically been part of discussions with some studies addressing this issue[7-11]. Recently, Ocko et al.[11] attempted to evaluate the climate impact of H_2 emissions as a consequence of dramatically increasing H_2 production and consumption. In this scenario, H_2 emissions into the atmosphere are expected to rise substantially, both from unavoidable small leakages (due to the inherent difficulty of containing H_2) and deliberate venting and purging of H_2, a mechanism that is critical for (the safety of) certain applications. This rise in emissions results in an increased amount of H_2 reacting with naturally occurring hydroxyl radicals (OH) in the troposphere, which is particularly concerning considering that OH acts as a methane sink. Therefore, the reduced OH availability leads to longer lifetime of methane (a greenhouse gas), while also the presence of H_2 and its further oxidation in the troposphere and lower levels of the stratosphere, result in a cooling effect and disturbance of the ozone chemistry[8]. Finally, the authors investigated different scenarios for blue (produced from natural gas) and green (produced from renewable energy sources) H_2, while also considering plausible emission rates. It is noteworthy that for green H_2 applications and with high emission rates (10%) the climate impact from fossil fuel technologies could be cut only in half for the first 20 years, which is far from the public's perception of climate neutrality regarding green H_2.

Therefore, not only should greater attention be given to improving H_2 emission estimations across the entire value chain, but it is also important to develop safety measures, that can: (i) prevent unwanted emissions (e.g. leakages) from occurring, and (ii) take measures against them when prevention is not possible, by accurately, fast and reliably detecting H_2 leakages. My project contributes to the latter, where I investigate and develop H_2 sensors that have the potential to be implemented in large-scale applications and aim at pushing the performance of current H_2 sensing solutions.

1.2 Current state of the art and unexplored challenges

The detection of H_2 for safety purposes is not a new concept; Already since the 1960s, when NASA began using hydrogen fuel for the Centaur program, safety guidelines (including instruments for leak detection) were implemented. Over the years these guidelines have been revised to incorporate new technologies and insights from the ongoing research in this field[12]. Today, and after many decades of research, a plethora of different H_2 sensing technologies exist, both at a commercial and research level. The common denominator is the induced change to a sensing material's properties in the presence of H_2. Regardless of the operating principle, important H_2 sensor properties (i.e. performance metrics) include the response time, limit of detection, resistance in complex environments (e.g. in the presence of CO, CO_2, NO_X, H_2O) and power consumption. The different H_2 sensing technologies are listed as follows[13,14]:

- **Thermal**

  These sensors operate on the principle of thermal conductivity differences between gases. H_2 has the highest thermal conductivity of all gases (0.174 W m^{-1} K^{-1} at 20 ºC) followed closely by helium. The thermal conductivity of air is one order of magnitude lower, which makes it suitable for detecting H_2 in air. A Wheatstone bridge (an electrical circuit for measuring an unknown resistance) is used to connect two resistors; one for the reference gas and one for the target gas (H_2). The higher heat loss induced to one of the resistors, due to the presence of H_2, leads to an imbalance in the Wheatstone bridge, manifested as a change in the overall resistance, which is the descriptor used in these types of sensors. Thermal conductivity-based sensors can operate up to 100 vol% H_2 (making them suitable also for oxygen-free detection) and are resistant to interference from poisoning species (CO, CO_2, NO_x, etc.) due to the absence of any catalytic surface. However, they typically have a higher limit of detection (LoD) than other H_2 sensing technologies (0.2 vol.% H_2[15]). Finally, they are non-selective, which can influence the sensor output signal, especially in complicated gas mixtures (including H_2O[16]), thus affecting the overall thermal conductivity. Advances in micro-machining and miniaturization have allowed for lower power consumption (3.32 μW[17]), decreased LoD (50 ppm in N_2[18]) and improved stability[17,19-21].
- **Electrochemical**

  An electrochemical sensor is based on the charge transfer phenomena occurring when a sensing electrode reacts with H_2, inside an electrolyte medium[22]. Two electrodes, coated with a catalyst material (e.g. Pt) that enables H_2 oxidation, are separated by either a liquid or solid electrolyte, depending on the operating temperature. At the sensing electrode (anode), H_2 oxidizes forming $2H^+$ and $2e^-$. The flow of electrons from the anode to the cathode results in current generation proportional to the H_2 gas concentration. Electrochemical sensors have typically very low LoD (40 ppm in air[23]) and consume very little power. However due to the catalyst present, they are susceptible to poisoning by species such as sulfuric compounds and CO.

- **Resistive**

  A resistance-based sensor detects the presence of H_2 due to changes in the electric resistivity of a sensing material upon exposure to the gas. Two main categories exist: (i) semiconductor-based and (ii) metallic resistors[24,25]. For the former, metal oxides (MO_x) are typically used, such as WO_3, TiO_2, In_2O_3, SnO_2[26]. The change in resistance occurs when the oxygen-covered sensing layer is exposed to H_2 and indicates that such sensors need the presence of molecular oxygen to be able to function. Initially the surface of the oxide is covered with adsorbed oxygen species, which capture free electrons and increase the resistance of the material. When H_2 is introduced, it reacts with the adsorbed oxygen, forming H_2O and releasing free electrons, effectively changing the resistance depending on the doping of the material (n or p-type). Traditional MO_x sensors are generally low cost and easily mass produced. However, these sensors require elevated temperatures (>500 ºC) to operate, which limits their applicability, and they are significantly cross-selective to other hydrogen-containing species (CH_4, H_2O, etc.). To further improve their sensitivity, doping of the MO_x is done with metals such as Pd, Pt, Cu, etc., which improve the catalytic performance (and at the same time reduce the temperature requirements) and can exhibit good response times (2 sec at 100 ppm in Air[27]) and significantly low LoD (5 ppm in N_2[28] for a Pd-based 2DEG system). In metallic resistors, as the name suggests, metallic hydride-forming structures are employed (such as Pd or Pd-based alloys[29,30]) which have the ability to readily dissociate and absorb hydrogen atoms into the bulk forming a metal hydride (MH_x). This leads to a transition from a metallic to a “less-metallic” state, resulting from a significant change in the electronic properties of the sensing material and consequently, an increase in resistance. These sensors have been long studied and exhibit overall great properties, such as ppb-range LoD[31], but usually suffer from CO or SO_x poisoning, due to the strong binding of such molecules to the surface of the sensing material. The metal-hydrogen interactions and hydride formation will be discussed in more detail in Chapter 2.

- **Acoustic**

  Acoustic sensors are typically based on piezoelectric materials which are very sensitive to changes in their surface properties. The most popular device is a quartz crystal microbalance (QCM) which consists of a quartz disc with 2 electrodes present on each side. When an AC voltage is applied, the disc will oscillate at its natural frequency. These devices are typically coated with a hydride-forming material, such as Pd, that allows for high sensitivity to H_2. The adsorption (and consequent absorption) of gas molecules changes the overall mass of the disc, causing a change in the resonance frequency which is related to the H_2 concentration. In a similar manner, surface acoustic waves (SAW) can be generated from the electrodes and utilized as a detection scheme of H_2, since they also exhibit high sensitivity to changes in the surface properties of the piezoelectric material. These sensors are reasonably fast (4.1 s at 1000ppm in N_2[32]) and with a low LoD (3.7 ppm in N_2[32]) however they show poor long-term stability and can be influenced by temperature modulations and other interfering gas species (non-selective).

- **Mechanical**
  Mechanical sensors utilize a micro-sized cantilever with a hydrogen-absorbing material, such as Pd, deposited onto it. The metal thus will absorb H_2 leading to an expansion of its lattice. This expansion translates to a deflection of the cantilever and is used to detect H_2. An advantage of these sensors is that they can operate in O_2 free environments, but they come with multiple shortcomings, such as the complex fabrication process, susceptibility to poisoning (due to the presence of a hydrogen-absorbing material) and aging effects (such as delamination).
- **Electronical**
  Electronical, or work function-based sensors employ a catalyst material deposited over an oxide layer. When the hydrogen atoms dissociate onto the metal, they spill-over at the metal-oxide interface, effectively altering the work-function of the metal (due to the rise of a dipole layer). These sensors are generally cheap and easy to fabricate, provide accurate measurements and reasonable LoD (10 ppm in N_2[33]), however they usually suffer from baseline drifts and hysteresis effects.
- **Catalytic**
  Catalytic sensors are one of the most employed type of H_2 sensors, and operate on the basis of heat generation, due to the combustible reaction

between O_2 and H_2 at a catalyst's surface. The high exothermicity of this reaction (-241.8 kJ/mol[34]) leads to a substantial increase of the temperature which is used to change the resistance (in Pellistor-type sensors[35]) or generate an electrical signal (thermoelectric sensors[36]). In the latter case the Seebeck effect is utilized, where the temperature difference between two points in a material induces a voltage difference. Most typical materials used here are Pt and Pd, due to their good catalytic performance for this reaction. Such sensors can operate in a wide range of environmental conditions, including high humidity (usually at the expense of sensor performance[37]) and can have fast response (~1 sec) however at quite high H_2 concentration (2 vol%[38]). Additionally, since Pellistor-type sensors require elevated temperatures to operate, they are non-selective to H_2, as other combustible gases such as CO or hydrocarbons can induce a temperature change. This problem is omitted in thermoelectric sensors since they can operate at, or near, room temperature and therefore show a decreased cross-sensitivity, since only H_2 can be effectively oxidized by Pt or Pd at these temperatures. Finally, and as with most methods using a catalytic surface, these sensors are susceptible to poisoning by CO, or sulfuric compounds, and can only operate in the presence of O_2.

- **Optical**

  Optical sensors take advantage of the changes in the electronic (and consequently optical) properties of a material when it interacts with H_2. The most commonly used material is Pd and Pd-based alloys, since i) Pd can form a hydride (PdH_x) at ambient conditions with a negligible energy barrier[39] and ii) the optical contrast induced by this change is huge, which allows for low LoD. Other materials such as Mg[40], Ta[41] or Hf[42,43] have been effectively used as optical sensors, however usually combined with Pd, either in the form of an alloy, or as a capping layer to promote H_2 dissociation and diffusion. Optical sensors possess several advantages; for one, they can operate in a wide variety of environments (oxygen-rich or free, vacuum, inert). Also, using optical fibers, the readout can be done remotely, thus avoiding the risk of spark generation (no electronics close to the sensor). Additionally, nanostructuring of the sensing material allows for faster response times (1s at 1000 ppm in N_2 or vacuum[41,44]) and exceptionally low LoD (250 ppb in Ar[45]). On the downside, and as with any Pd-based sensor, they are prone to poisoning, which however can be alleviated by means of alloying[46,47] or the application of protective coatings, such as polymers[44,48-50]. Optical *nanoplasmonic* H_2 sensors are the core of this thesis and will be discussed in more detail in Chapters 2 & 3.

Having summarized the different H_2 sensing technologies, two things become clear: i) Pd, either pristine or combined with other materials, plays an important role in multiple different detection schemes, due to its unique interaction with H_2. ii) All of the technologies have several advantages and disadvantages. Therefore, in recent years, a common pattern found in literature is the interplay between different sensing solutions, where the goal is to combine the good features and eliminate the weaknesses.

To this end, extensive research has been focused on developing H_2 sensors that, irrespective of the operating principle, aim to meet performance targets set by various stakeholders, with the most stringent and well-known ones established by the U.S. Department of Energy (DoE)[51-53]. Recently, Darmadi et al.[54] conducted a comprehensive study summarizing the efforts by researchers to achieve these targets (**Figure 2**), while also highlighting current challenges and proposing strategies to overcome them.

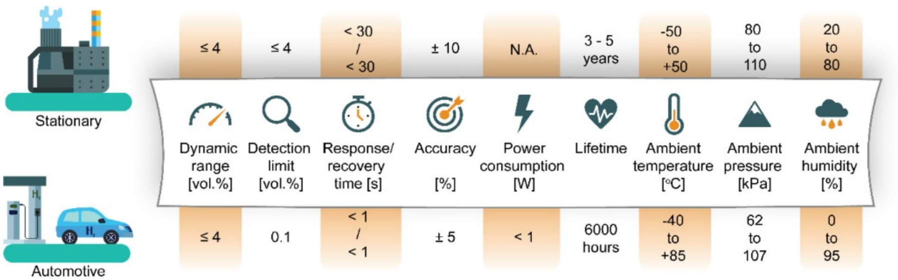

Figure 2: *Schematic illustration of the US DoE performance targets for* H_2 *sensors aimed for stationary and automotive applications (adopted from ref.*[54]*).*

One of the most critical and challenging targets is achieving a 1-second response and recovery time for H_2 sensors. Over the past two decades and with the progress in nanofabrication and miniaturization techniques, numerous efforts have been made to address this challenge. While several sensors have successfully met the 1-second response target, they have often fallen short of doing so at the 0.1 vol.% detection limit[55-57]. For instance, a cracked sputtered Pd thin film on an elastomeric substrate demonstrated a response time of <1 second, but only for H_2 concentrations ranging from 0.4 to 4 vol.%[55]. Similarly, SnO_2 nanowires decorated with POSS-stabilized Pd nanoparticles achieved a response time of <1 second, but at a H_2 concentration of 3 vol.%[56]. It was only in recent years that this target was successfully met; Nugroho et al.[44] were the first to demonstrate it, albeit in vacuum/pure H_2, using an ultrafast Pd-Au alloy sensor, combined with a tandem PTFE/PMMA capping layer, that was able to achieve response times < 1 second for 0.1 vol.% H_2. A few years later, Bannenberg et al.[41] developed a Ta-Pd alloy sensor that exhibited sub-second response times times at 100 Pa partial pressure (100% H_2 pulses applied in vacuum) under room temperature conditions. At the same time Luong et al.[58] developed a Pd-Co alloy sensor with 0.85 s response time at 0.1 vol.% (in vacuum/pure H_2) and a LoD of 2.5 ppm. Today, more sensors have been able to achieve this target, however at elevated temperatures[59-61].

One of the targets set by stakeholders which has remained relatively unaddressed is the stable operation of H_2 sensors in humid environments[52,62] (**Figure 2**). Such conditions are exceptionally relevant, like for example the highly humidified H_2 gas feed in fuel cells, which is crucial for the stable operation of the polymer exchange membrane, or the largely humidity-fluctuating open environment (due to weather, or geographical factors), where a sensor can be deployed for process monitoring or safety applications. Since the conditions can vary from dry to highly humid in such environments, it is very important to use sensors that can reliably operate in many different humidity scenarios.

In Pd-based sensors, operating in humid environment is challenging because the availability of catalytically active surface sites for H_2 dissociation is critical to enable subsequent absorption of H into the particles, and thereby generate the sensor signal in both optical, mechanical and electric resistance-based sensors[16,63,64]. Adsorbed water and hydroxyl groups effectively block these sites and thus hinder the ability of H_2 molecules to reach the surface and dissociate. This results in increased response time, increased LoD and instabilities in the baseline signal all the way to complete sensor deactivation.

Only a limited number of studies in the literature investigate this "humidity challenge" in H_2 sensing applications[37,65-69]. Among these, most studies either tackle the issue only partially, i.e., for a narrow and low humidity range, or demonstrate solutions under conditions that are limiting from an application perspective. A recent effort to address the humidity challenge is the work of Rahamim et al.[68], where they fabricated a current-based ITO sensing layer, combined with Pd-Ni or Pt nanoparticles via a colloidal synthesis approach. They report low LoD, repeatability, and tolerance to humidity up to 60% relative humidity (RH). Regarding a limited applicability, a prime example is the investigation of the H_2 sensing behavior of SnO_2 and In_2O_3 thin films, at very low H_2 concentrations and in a wide humidity range. Specifically, Murthy et. al.[69] demonstrated a limit of detection of 25 ppm H_2 with a humidity-independent response to H_2 (for SnO_2) in the range of 20-95% RH. However, this study was conducted at a significantly elevated temperature (623 K), which limits the practical applicability of the sensor, since such a device would not only require high power to operate, but also runs the risk of H_2 self-ignition[6]. Another noteworthy example is the work of Geng et al.[37], where grain-boundary-rich Pt nanoparticles were fabricated and drop-cast onto a thermocouple for thermocatalytic H_2 sensing. This sensor operates on the basis of the highly efficient and exothermic hydrogen oxidation reaction (HOR) on Pt surfaces causing a significant temperature increase in the presence of H_2 While the sensor is able to operate in a very wide humidity range (0-98%), the LoD increases with increasing humidity to ~3% H_2 at 98% RH.

From this summary, it is clear that more efforts are needed to design sensors that can reliably operate in high humidity levels with low LoDs and fast response time. Such conditions are particularly relevant for numerous H_2-related applications, including the highly humidified gas feed in fuel cells, or the fluctuating environmental conditions encountered when sensors are deployed in open ambient locations.

1.3 Goals of this thesis

The purpose and the goal of this thesis is to address two major technological challenges that the H_2 sensing community faces. The first thing is to design a sensor that can perform reliably under high humidity environments since, this is a case which is relevant in numerous applications where the presence of H_2O not only cannot be avoided, but in some cases (e.g. fuel cells) is crucial for their stable operation. For that reason, we have developed in **Paper I** a Pt-based dual function nanoplasmonic/catalytic H_2 sensor, that can detect H_2 in a wide relative humidity range (0-80% RH) with 600 ppm LoD. The second aim is to go beyond materials' engineering and utilize advanced data analysis techniques that can address both the humidity challenge, and improve upon one of the most stringent performance metrics, namely the sensor response time. As described previously, only a few sensors reported in the literature can reach the target of responding to 0.1 vol.% H_2 faster than 1 second, and in most cases do so either in idealized conditions (vacuum/H_2) or at impractical environmental conditions (e.g. strongly elevated temperature). Therefore, instead of *just* looking for new materials and structures that can achieve this target, it is also possible to optimize the way we analyze the data derived from a sensor. In many cases, and specifically for nanoplasmonic H_2 sensing, spectral information is typically collapsed into a single descriptor and thus most of the information is left unused. This is where neural-network based data treatment comes into play; such AI-based models can utilize the entirety of the acquired spectral information, and discern complex patterns within that, often hidden by noise. They can also find temporal correlations among the spectra, thus predicting not only H_2 concentrations, but also the presence of species that alter the sensor's response (e.g. H_2O). Therefore, in **Paper II & III** we utilize such neural network-based models to both accelerate the response time of a PdAu nanoplasmonic hydrogen sensor, and remove the negative effect that H_2O, present in the gas, has on the H_2 sensor's response.

2 Metal-Hydrogen interactions

Hydrogen is the lightest and most abundant element in the universe and possesses unique properties, such as high thermal conductivity, high diffusivity and high reactivity. These characteristics make hydrogen one of the most widely used elements across a broad range of applications. Since H_2 is a highly diffusive gas, it needs to be stored and used upon demand. With the energy crisis in the 1970s metal hydrides began to be explored as a means to potentially store hydrogen safely and efficiently for energy systems. This is made possible by the high solubility of hydrogen in numerous metals, such as Ta[70], Ti[71], Pd[39], as well as intermetallic and alloy compounds[72]. The conditions for forming a metal-H solid solution can vary significantly, where pressure and temperature are the key parameters. Additionally in the context of heterogeneous catalysis, hydrogen plays a crucial role in many catalytic reactions; from fuel cell applications[73], synthesis of ammonia via the Haber-Bosch process[74], to CO_2 hydrogenation[75]. Since transition metals and their oxides are predominately used in heterogeneous catalysis, understanding the metal-hydrogen interactions of these systems is particularly relevant. In this Chapter, I will delve deeper into the metal-hydrogen interactions, both from the perspective of hydride formation in pristine and alloy metals, as well as the hydrogen oxidation reaction (HOR) on transition metal catalyst surfaces. For the latter, I will focus on Pt-H interactions and introduce the role of humidity in the hydrogen sorption dynamics.

2.1 The Pd-H system

In H_2 sensing, Pd has attracted the most attention by far, due to its unique ability to dissociate H_2 into atomic hydrogen under ambient conditions, followed by H-species diffusion into the lattice where they occupy interstitial lattice sites. A H_2 molecule initially adsorbs on the surface of Pd and dissociates in two H atoms, essentially without an activation barrier (**Figure 3**). The next step towards diffusion into the bulk is to first reach the subsurface layer, which is considered to be the rate-limiting step in the absorption process[76]. Finally, H atoms diffuse into the bulk and occupy interstitial sites, forming a solid solution at low H_2 partial pressures and a hydride, PdH_x, above a temperature-dependent critical pressure[76,77]. As previously mentioned, Pd is unique in that aspect, since the absorption process occurs at room temperature and is fully reversible, in contrast to several other hydride- forming metals.[71,78]

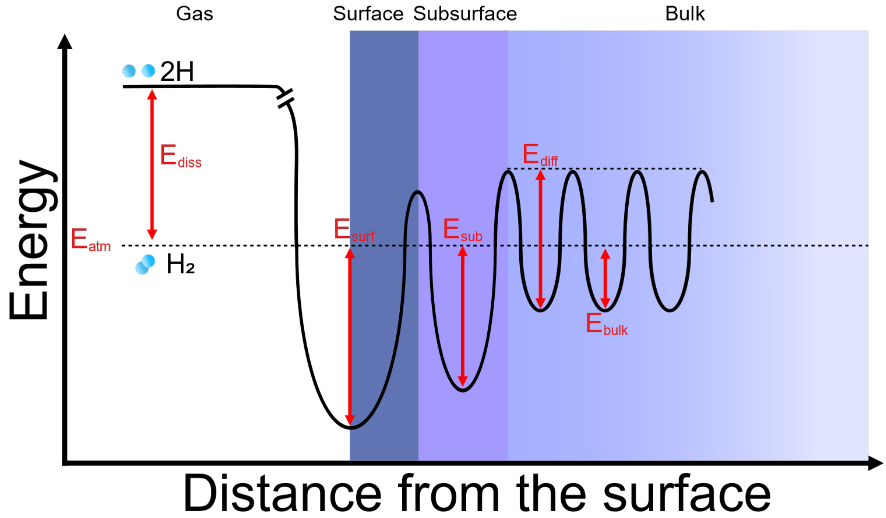

Figure 3: *The potential energy diagram of a H_2 molecule approaching a Pd surface. E_{atm} is the energy of a H_2 molecule in the gas phase. E_{diss} is the energy difference between a H_2 molecule and two dissociated H atoms on the Pd surface. E_{surf} and E_{sub} refer to the binding energies of a H atom at the surface and subsurface layers, respectively. E_{diff} is the energy barrier for diffusion into the bulk. E_{bulk} represents the binding energy of hydrogen within the bulk interstitial sites (adapted from ref.[76]).*

At low H_2 concentrations in the gas phase, the H atoms that have dissociated on the surface of Pd diffuse in the bulk and occupy interstitial sites in the fcc lattice, where they are sparsely distributed with minimal interaction among them, thus forming a dilute solid solution called the α-phase (**Figure 4**). At room temperature the maximum solubility for this phase is x= 0.017 (expressed in PdH_x) and the α lattice parameter of Pd increases from 3.887 Å to 3.895 Å due to the lattice expansion (which in turn leads to lattice strain) induced by the H atoms[39]. In this phase, the system follows Sieverts' law[77,79],

$$c_H = \sqrt{K p_{H_2}} \tag{2.1}$$

where c_H is the concentration of H in the metal, K is the equilibrium (Sievert's) constant and p_{H_2} is the partial hydrogen pressure. As the H_2 pressure increases, Sieverts' law ceases to apply, and above a critical pressure a new thermodynamic phase within the Pd-H system, called hydride or β-phase, begins to form due to the now effective attractive H-H interactions between interstitial H atoms, and thus marking the change from a dilute solid solution, to a system where H is more densely packed. When this β-phase starts to nucleate in the α -phase matrix, the system enters the two-phase (α+β) coexistence region, where both phases occur at the same time until system has completed the first order phase transformation into the hydride. Accordingly, at $PdH_{\sim 0.6}$ the system is fully converted to the β-phase, where the Pd lattice has expanded significantly, and hydrogen atoms occupy ca. 60 % of all interstitial sites. In the hydride phase, the lattice parameter has increased to 4.025 Å[39], yielding a total volume expansion of ~10%. Further increase in p_{H_2} will result in minimal increase of c_H. As it is visible in the pressure-composition schematic (**Figure 4**) the coexistence of the α- and β-phase happens below the critical temperature (T_c = 295 ºC). Above that temperature, the phase transition does not exhibit the characteristic plateau (miscibility gap) associated with it and is no longer a first-order transition.

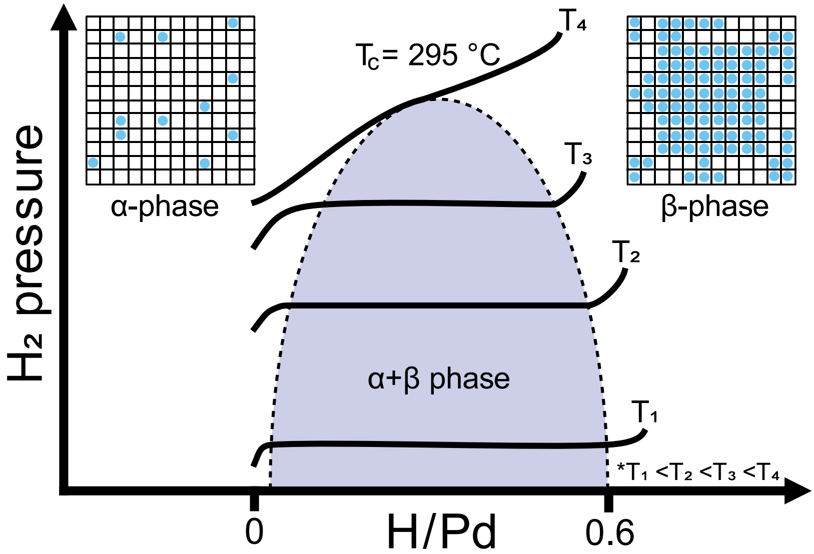

Figure 4: *A schematic of pressure-composition isotherms and the phase diagram for the Pd-H system. For a given temperature and at low H_2 pressure H atoms occupy random octahedral interstitial sites within the Pd host lattice and with minimal H-H interaction, thereby forming a dilute solid solution called the α-phase. As the pressure increases, the β-phase – the hydride- begins to nucleate at a critical pressure due to by then effective attractive H-H interactions and initiates the first order phase transformation to the hydride phase. This transformation causes an overall expansion of the Pd lattice. Below the critical temperature of 295 ºC, above which the phase transformation no longer is of first order, an α + β phase coexistence plateau exists, called the miscibility gap (adapted from ref.[80]).*

First-order phase transitions are usually accompanied by hysteresis[81], which is also present in the Pd-H system. The presence of hysteresis means that the relationship of the H_2 pressure and c_H is dependent on whether the pressure is increasing or decreasing. **Figure 5** shows an isothermal curve measured for H_2 sorption in Pd nanodisks (including example SEM images of nanodisks), during both H_2 loading and unloading. Clearly, the H_2 pressure required for the desorption process (β- to α-phase transition) is lower, than that of absorption (α - to β -phase transition). The origin of hysteresis has been investigated for many years, with two main theories explaining this effect.

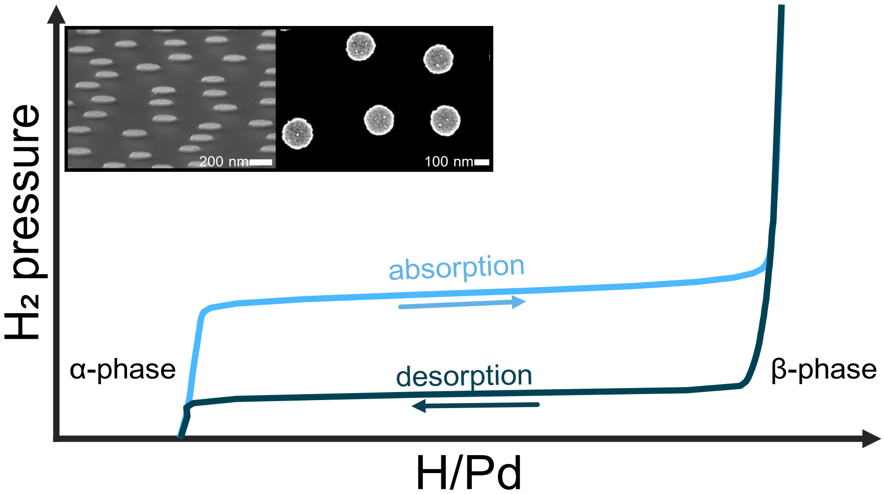

Figure 5: *Experimental curves of a pressure-composition isotherm for Pd nanodisks, measured at 30 ºC. The absorption and desorption pathways are different leading to the hysteresis gap. The two inset SEM images are an example of fabricated nanodisks (Pt in this case) used in this thesis.*

The earliest theory suggests an *incoherent* phase transformation where dislocations are created, plastically deforming the lattice and minimizing elastic stress. Here β-phase precipitates grow at the expense of the α-phase, until the entire system transitions to the β-phase. The energy required for the formation of dislocations during the α-to-β and β-to-α phase transitions are different, causing the hysteresis gap.[82,83].

A second, more recent theory describes a *coherent* phase transformation, where the lattice is deformed elastically and the lattice parameter between the two phases varies smoothly. This continuity minimizes the formation of dislocations or defects but causes significant strain at the phase boundaries[84-86], which introduces a higher energy barrier for the transition between phases. This effectively means that, compared to an *incoherent* phase transformation, higher H_2 pressure would be required for the α-to-β transition and lower H_2 pressure for the β-to-α transition, leading to a wider hysteresis gap[85].

It is important to emphasize that bulk Pd typically undergoes *incoherent* phase transition, since it is thermodynamically favorable; the lattice mismatch between the two phases is significant and therefore the system can relieve the strain through plastic deformation. On the other hand, *coherent* transitions are present in nanoscale systems (nanoparticles and thin films) where, below a critical size, coherency is favored due to reduced strain energy[87].

As a last point in this context it is also relevant to discuss the changes in the kinetics and thermodynamics of hydrogen sorption taking place for nanostructured, rather than bulk, Pd. Of particular interest are Pd nanoparticles, since they play an important role in the implementation of Pd in hydrogen sensors. Pd nanoparticles are found to exhibit size-dependent ab/desorption rates due to two reasons: i) decreasing the size increases the surface-to-volume ratio (SVR), effectively providing more surface sites for H_2 dissociation and fewer interstitial sites to occupy. ii) The hydrogen diffusion path length is shorter for smaller particles, which exponentially reduces the ab/desorption times[88]. Additionally, the surface properties of Pd have been reported to affect the kinetics of hydrogenation. Polycrystalline Pd with a high amount of grain-boundaries have been shown to greatly enhance hydrogen diffusion[89,90] and decrease the H_2 pressure required for hydride formation due to reduced strain barriers[91].

2.2 The concept of alloying

Since the Bronze Age, the concept of combining two or more elements (metallic or non) to create materials with enhanced properties has been pivotal to mankind's societal evolution. In the case of metals, alloying can be achieved in many different ways, such as melt-mixing[92], powder metallurgy[93], vapor deposition[94] or solid-state diffusion[95,96], to name a few. The latter method, used in this thesis, involves the annealing of two (or more) metals in contact with each other, at high temperatures, where atomic diffusion between them leads to the formation of an alloy if that is thermodynamically allowed. However, solid-state diffusion is a slow process. At best (near the metals' melting point) the rate at which atoms diffuse is in the µm/s range[97], and it only becomes slower at lower temperature. Therefore, the key parameters that dictate alloy formation in solid-state diffusion are temperature and time. Of course, other factors play a role as well, such as the elements' melting temperatures and diffusion coefficients, annealing environment, as well as structural and chemical compatibility. In many cases (including this thesis) annealing is performed at temperatures significantly below the melting point of the metals. This is especially beneficial for the alloying of nanosized systems, since the time required to do so is greatly reduced. Even at these relatively low temperatures, there is enough thermal energy provided to overcome diffusion barriers, increase atomic mobility and, thus, allowing diffusion of atoms across the interface of the two metals in contact. Given enough time, the atoms from one metal will diffuse into the crystal lattice of the other, forming either a homogeneous mixture or an intermetallic compound (**Figure 6**).

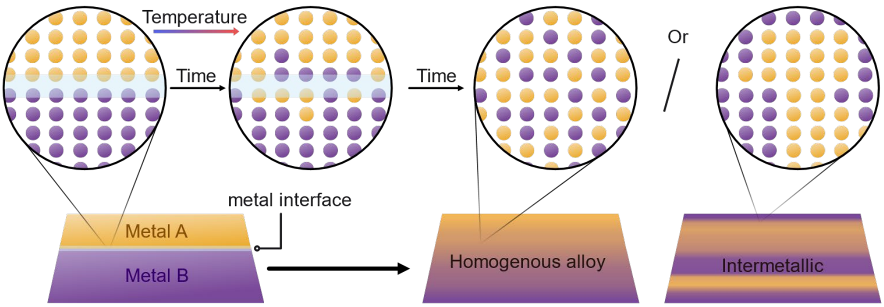

Figure 6: *Schematic illustration of the alloying process of two metals in contact. The structure depicted here is an example of a layer-by-layer deposition via e-beam physical vapor deposition (PVD) (see Chapter 5 for more details). Given a high enough temperature and time, the atoms at the metal interface will begin to diffuse across that interface. In the end, provided it is thermodynamically favored and any kinetic barriers can be surmounted, a homogeneous alloy or an intermetallic compound will be formed, dependent on the structural and chemical compatibility between the metals.*

2.3 Hydrogenation of Pd-based alloys

Based on the discussion in section 2.1, one of the major drawbacks of Pd is the presence of a large hysteresis gap during absorption and desorption of H_2. Therefore, a way to alter the thermodynamics, as well as the kinetics, of the Pd-H system is to alloy Pd with other metals.

Over the last years, there has been a lot of research done on Pd-alloy hydride materials (with a focus on thin-films and nanostructures) which have advanced the state-of-the-art hydrogen sensing schemes[46,47,98-102]. In this context, a particular system that has attracted considerable attention is Pd-Au. It has been shown that the introduction of Au atoms into the Pd crystal structure not only reduces the hysteresis gap but also improves the kinetics[101-103]. The former is attributed to the structural properties of the individual elements; Pd and Au both have an fcc structure. The lattice parameter of Au is larger (4.078 Å[104]) than that of Pd (3.887 Å[39]), and therefore the addition of Au atoms leads to an overall expansion of the crystal lattice structure (which is linear to the Au content according to Vegard's law[105]) which pre-strains the host's (Pd) lattice and reduces the energy barrier associated with the α-to-β phase transition. This is manifested in both a narrower hysteresis gap, where the absorption and desorption curves move to lower and higher pressures respectively, as well as a reduced H solubility, with increasing Au content[101,102]. Additionally, as Wadell et al.[101] demonstrated, the sensitivity (extinction change (ΔExt in %) per 1 mbar of H_2 pressure) actually increases (with increasing Au content) by a factor of 8, in the 1-10 mbar H_2 concentration regime. More specifically, by measuring absorption isotherms at 30 ºC (in vacuum/H_2), for different alloy compositions (0-25 at.% Au) the reported sensitivity was calculated as 0.0338 %/mbar, showcasing the usefulness of such a sensor for early stage H_2 leak detection. Finally, the presence of Au induces changes in the electronic properties of the Pd host, where the energy barrier for surface-to-subsurface H diffusion is reduced thus allowing for overall faster kinetics[101,106]. In terms of hydrogen sensing this translates into four key points: i) The addition of Au eliminates hysteresis, and the sensor is no longer dependent on the H_2 pressure history. ii) The response time is reduced allowing for faster H_2 detection. iii) A trade-off exists, where the reduced H solubility results in a smaller dynamic range for the sensor, i.e., lower optical contrast (e.g. at 1 bar) compared to Pd. iv)

In the more technologically relevant H_2 concentration regime, i.e., below the 4 vol.% (40 mbar) lower flammability limit, PdAu-based sensors exhibit enhanced sensitivity compared to pure Pd-based sensors[101].

Another shortcoming of Pd-based sensors, as can be seen in the summary of the different H_2 sensing technologies in Chapter 1, is their susceptibility to CO and SOx poisoning[107-109]. As an example, CO readily adsorbs onto Pd and blocks surface sites that are critical for H_2 dissociation and consequent absorption. The extent of this effect dependents on factors such as temperature, CO pressure and the Pd surface morphology[110].

One way to mitigate CO poisoning is by means of alloying. It has been shown that Cu is a great candidate for establishing a CO poisoning resistance in PdCu systems[111]. Here, the reduced CO poisoning effect is attributed to the lower availability of higher coordinated Pd sites (due to the presence of Cu) and which are the most favorable for CO binding[112].

In the context of hydrogen sensing, and with the aforementioned drawbacks of Pd, alloying with copper also affects the thermodynamics. From a structural point of view, Cu has a lattice parameter (3.627 Å[113]) that is smaller than Pd, which means that alloying Pd with Cu causes a contraction (compared to expansion in PdAu) of the Pd host lattice with increasing Cu content. The consequence of that is the narrowing of the hysteresis gap, increase in the H_2 pressure of the absorption/desorption plateaux, and an overall reduced sensitivity to H_2 [46,114].

In an attempt to get the best of both worlds, i.e., Au and Cu, Darmadi et al.[46,47] developed and optimized a ternary $Pd_{65}Au_{25}Cu_{10}$ alloy, that exhibits excellent CO resistance up to 500 ppm CO, hysteresis-free response, as well as enhanced sensitivity and kinetics compared to a neat Pd sensor.

To further discuss the potential of alloying to improve H_2 sensor performance, the Tantalum-Palladium system, even though not strictly a Pd-*based* sensor since Pd is the solute component, is particularly interesting[43,115]. The bulk Ta-H phase diagram shows multiple first order transitions across a large hydrogen content range[43,70], which leads to substantial hysteresis. However, above a critical temperature, i.e. > 61 ºC, things become simpler; A large solubility range exists within one thermodynamic phase (α-phase) making Ta promising for sensing applications. By alloying Ta with Pd, Bannenberg et al.[41] (discussed in Chapter 1.2 as a sensor that meets the 1s target in 0.1 vol.% H_2) recently demonstrated a $Ta_{88}Pd_{12}$-based thin-film optical H_2 sensor, that exhibits a hysteresis-free response at room temperature, with an outstanding dynamic range spanning over 7 orders of magnitude in H_2 pressure. They attribute this performance to both the alloying and nanoconfinement of the sensing material. For the former they have investigated different Pd contents within the alloy and found the optimal concentration (12 at.% Pd), where there is both hysteresis-free response, and almost constant sensitivity across the whole sensing range. The latter, i.e. nanoconfinement, allows for the suppression of the first-order transitions that occurs at T < 61 ºC due to an induced clamping effect of the nanometer sized TaPd layer to the support. Therefore, upon hydrogenation the unit cell expands in the out-of-plane direction, elastically deforming it across the entire H_2 pressure range.

2.4 Platinum-Hydrogen interactions

Unlike Pd, Pt does not absorb H under ambient conditions but rather requires highly elevated temperatures and pressures for stable hydride formation[116], where it exhibits unique features such as superconductivity[117,118]. However, Pt is still used in many different H_2-related technologies, including sensing[17,19,20,24,25,37,38], due to its excellent catalytic properties for the desired reactions. H_2 and O_2 adsorption and dissociation occur at ambient conditions[119-121] on Pt. Specifically, H_2 dissociation is favored at low-index surfaces[119] (e.g. 111) and surface defects, such as edge atoms[122], where the kinetics of dissociation are enhanced[120].

Pt finds itself in numerous heterogeneous catalytic reactions (where O_2 and/or H_2 are involved); from CO oxidation and NO reduction for the automotive industry[123-127], to hydrodesulfurization[128,129] for sulfur removal from fuels, to the most important reactions in fuel cell technologies, the Oxygen Reduction Reaction (ORR)[130] and Hydrogen Oxidation Reaction (HOR)[131,132].

In the context of sensing, Pt is present in many different detection schemes. For example, in resistance-based sensors, Pt is used either in combination with-, or as, the sensing material. In the former case, reports show a spillover mechanism, where H_2 first catalytically dissociates on the surface of Pt, and then migrates to the sensing layer (typically a metal or semiconducting oxide), where it causes a change in resistance[133,134]. In the latter case, i.e., Pt *as* the sensing element, the prevailing mechanism suggests a difference in the electron scattering between O- and H-covered surfaces, which can be traced back to the differences in the electronic properties of a H- and O-covered Pt surface (discussed in more detail in Chapter 3.1.1 and 3.2.2). Briefly explained the presence of O on the surface of Pt is accompanied by substantial inelastic electron scattering (i.e. diffusive scattering) which increases the electrical resistance of the material. Upon H_2 exposure, the O species on the surface will be partially replaced with H, whose electron scattering cross section is expected to be lower, leading to a decrease in the electrical resistance relative to an O-terminated surface[24]. This relative change is used as the sensing mechanism in resistive Pt sensors operated in an O_2 rich environment (i.e. air)[24,25,135,136].

In catalytic and thermocatalytic sensing, Pt-based sensors utilize the efficient HOR, a reaction that is highly exothermic and thus leads to a significant temperature increase of the sensor (which can be directly measured[37]), and consequently a change in resistance[38].

2.4.1 Platinum as a catalyst for the Hydrogen Oxidation Reaction

Pt constitutes a well-established catalyst material for the HOR in, e.g., fuel cells[137]. In this reaction H, O and OH react to form H_2O. As briefly mentioned in chapter 2.4, this reaction is also used as a detection mechanism in several different sensing technologies.

H_2 and O_2 can readily chemisorb and dissociate on the surface of Pt. For H_2, as aforementioned, the presence of defects, such as grain boundaries or steps, greatly influences dissociation rates[122], while O_2 is found in the dissociated state at ambient conditions[121,138]. Once dissociated, the HOR will proceed via the Langmuir-Hinshelwood mechanism, where the adsorbed atoms thermally diffuse on the surface and react[139]. The reaction can take place via different routes[139-141],

$$H_{(ads)} + O_{(ads)} \rightarrow OH_{(ads)} \tag{2.2}$$

$$H_{(ads)} + OH_{(ads)} \rightarrow H_2O_{(des)} \tag{2.3}$$

$$OH_{(ads)} + OH_{(ads)} \rightarrow H_2O_{(des)} + O_{(ads)} \tag{2.4}$$

where the subscripts "ads" and "des" refer to adsorbed species on the surface and desorbed species in the gas phase, respectively.

These reactions imply that dissociated H and O atoms react to form H_2O, and/or an intermediate step takes place, where H first reacts with O forming hydroxyl (OH) which further leads to the final product H_2O. Regardless, the overall reaction is highly exothermic (-241.8 kJ/mol)[34] and has been shown to occur at room temperature on polycrystalline, defect-rich Pt[37].

2.5 The role of humidity in hydrogen sorption dynamics

H_2O is at the core of many important H_2-related technologies, both as a key feedstock (green H_2 production) and as a primary product in many reactions involving H_2. Key examples are H_2O electrolysis[142], where H_2O is split into H_2 and O_2 using electricity, or in fuel cells, where H_2O is the main product formed at the cathode, as a result of the HOR and ORR. Besides that, H_2O is present also, in the form of vapor, in the gas feed, since it is not only crucial to keep the fuel cell proton exchange membrane from drying out, but also to maintain high ionic conductivity[143].

The interaction of metal surfaces with H_2O, is crucial in many physico-chemical phenomena, and extensive investigation has been carried out over the last decades to understand the H_2O structure and bonding properties on surfaces. Structures of H_2O can range from clusters, to chains and to two-dimensional (2D) layers depending on the metal and its surface properties, H_2O coverage, as well as environmental conditions[144,145].

For example, in the case of Pt and Pd (111) and at low coverages, H_2O adsorption (in the case of clusters) is more stable on atop sites compared to bridge or hollow sites[144,146]. At higher coverages, bilayers and multilayers have been reported on both Pt and Pd, where depending on the surface, H_2O can adsorb molecularly (Pt(011), Pt(111) and Pd(111)[147]), or dissociatively (Pt(001)[144,148,149]).

In the context of hydrogen sensing, H_2O (in the form of humidity) can significantly impact the H_2 sorption dynamics of both hydride-forming and catalytic materials. Taking Pd and Pt as an example, they are often used in applications in the form of polycrystalline materials with multiple facets, where water adsorption is more complex than previously described. In other words, H_2O can exist on their surfaces in both molecular and dissociated forms, leading to various adsorbed species such as O and OH. These species (including adsorbed H_2O) not only occupy surface sites that are necessary for H_2 dissociation (thereby reducing the H_2 dissociation rate) but also readily and catalytically react with adsorbed H to form H_2O since both Pd and Pt are effective catalysts for that reaction. More specifically for the Pd case, a competing reaction occurs, where H is consumed for H_2O formation, hindering the formation of PdH[64]. In terms of sensing performance, this leads to an increase in the response time and LoD, as well as instabilities in the baseline signal. In this thesis, I address the humidity issue in two ways: in **Paper I** we investigate a Pt-based catalytic/nanoplasmonic H_2 sensor that actually exhibits *enhanced* response in highly humid environments, showcasing a 600 ppm LoD in a wide relative humidity range of 0-80%. In **Paper III**, we address this issue by employing a machine learning technique to process the data from a (hydride-forming) PdAu nanoplasmonic sensor operating in a wide-humidity range, thus eliminating the negative influence of H_2O.

3 H_2 sensing

In the previous chapter, I discussed the metal-hydrogen interactions, both from the perspective of Pd and Pd-based materials for hydride formation, and from the perspective of Pt-H_2 interactions giving rise to important catalytic reactions in the presence of O_2. Here, I will delve deeper into the induced changes to the materials' fundamental properties, i.e., electronic properties, focusing on the localized surface plasmon resonance (LSPR) which is the main feature that is utilized in the H_2 sensing technology presented in this thesis. Finally, further attention will be given to catalytic hydrogen sensing, and more specifically to the role of Pt as a sole, and combined with other materials, catalytic/plasmonic sensor.

3.1 Nanoplasmonic sensing

Nanoplasmonic sensing is an optical sensing technique, based on the LSPR, a feature that is present in metallic nanostructures (will be discussed in 3.1.2), and is based on the optical properties of a material which are ultimately determined by its electronic structure. Therefore, it is important to first understand what happens at a more fundamental level when H_2 interacts with a metal, and for that reason Pd is the best candidate to be used as an example, when it comes to hydride forming materials.

3.1.1 Electronic structure

I have already discussed in previous sections, the importance of Pd-based materials in H_2 sensing technologies, due to their unique interaction with H_2. Pd ([Kr]$4d^9 5s^1$), in its pure metallic form, has a strong d-band contribution near the Fermi level (E_F)[150], where the metallic character of Pd, results from the high density of states (DOS) near that. The transition from pure Pd to a PdH_x induces substantial changes in the electronic structure (**Figure 7**), where the addition of interstitial H atoms in the host metal, which carry new electronic states, effectively causes a redistribution of the electronic states of the system and a shift of the d-band below the E_F[150]. With increasing H content inside the lattice, the DOS shift increases, until the complete formation of the β-phase, where the DOS at the E_F are greatly reduced[151]. In addition to the much lower DOS (at the E_F), the presence of H atoms inside the fcc lattice causes significant scattering of the conduction electrons, due to the induced lattice expansion, and thus increases the resistance of the system[152,153]. This effect is utilized in resistance-based H_2 sensors[29-31], as described in Chapter 1.

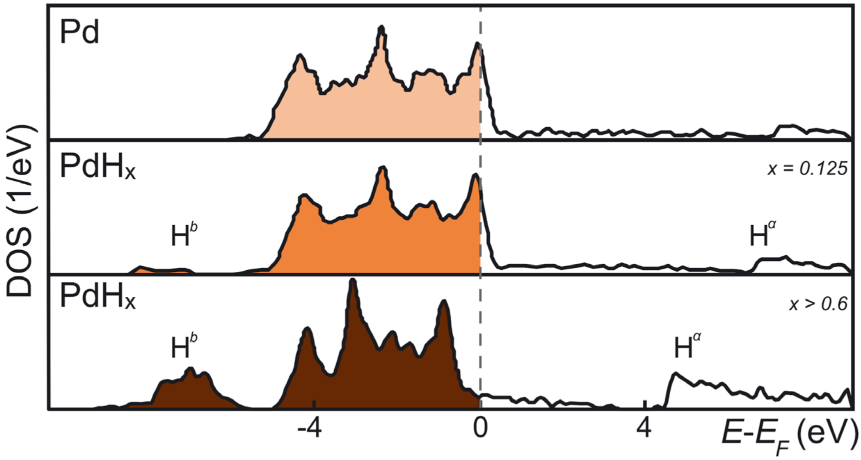

Figure 7: *The evolution of the density of states (DOS) in pure Pd, $PdH_{0.125}$ and PdH_x (x > 0.6, β-phase). The dashed line denotes the Fermi level (E_F). As H is introduced into the Pd host metal, the d-band is filled, and the DOS shift to the left, below E_F. At x > 0.6 the DOS at the E_F is greatly reduced. The Pd-H chemical bond results in the formation of the bonding (H^b) and antibonding (H^a) states below and above the E_F respectively. The colored parts represent filled electronic states (adapted from ref.[151]).*

The changes in the electronic properties of Pd give rise to a consequent change in the optical properties of PdH_x. This is manifested by the dielectric function, a material property that describes its interaction with an electromagnetic field. The dielectric function $\varepsilon^*(\lambda) = \varepsilon_1(\lambda) + i\varepsilon_2(\lambda)$ consists of the real part, $\varepsilon_1(\lambda)$, which describes the dispersion properties of a material, i.e. how easily/fast it responds to an oscillating external field (e.g. light). In metals $\varepsilon_1(\lambda)$ is negative, indicating a strong screening effect of the electric field, possible due to the abundance of valence electrons close to the E_F, and is therefore indicative of their metallic character (reflective characteristics in the visible). On the other hand, the imaginary part $\varepsilon_2(\lambda)$ is a positive value describing losses, and specifically represents energy dissipation in the form of absorption or scattering. **Figure 8** shows how the real and imaginary part of $\varepsilon^*(\lambda)$ change over time, with increasing H-content inside the Pd host. Here, the continuous absorption of H results in i) increase of $\varepsilon_1(\lambda)$, indicating a "less metallic" character, ii) a decrease in $\varepsilon_2(\lambda)$ which corresponds to weaker absorption of the electromagnetic wave. It is therefore

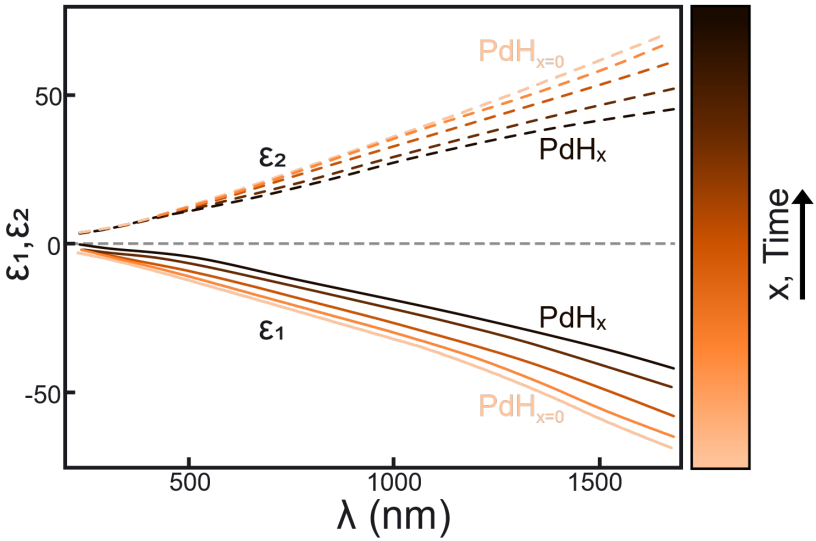

this change that forms the basis for Pd-based optical H_2 sensing.

Figure 8: *The real (ε_1) and imaginary (ε_2) part of the dielectric function of Pd, and its evolution during PdH_x formation. As time (and x) increases, ε_1 increases, representing a "less metallic" character. At the same time, ε_2 decreases indicating the reduced absorption/scattering properties of the system (adapted from ref.[154]).*

In the context of this thesis, it is important also to delve deeper into the electronic structure of the materials used here, i.e., PdAu and Pt. Starting with the former, in Chapter 2, I discussed the structural implications of alloying Au with Pd, and how it affects the thermodynamics of hydrogenation. However, looking at the electronic structure, useful information can be extracted regarding both the optical properties of the material and the optical contrast induced upon hydrogen absorption.

Pd and Au have distinctly different electronic structures. Au ($[Xe]4f^{14}5d^{10}6s^1$) as a noble metal, has a full d-band located 2-2.5 eV below

E_F[155,156], which is responsible for strong plasmon peaks in the visible regime, due to i) d-sp interband transitions that occur when the material absorbs light (specifically at the frequency range where the 5d-band is located) and ii) weak interband damping at the NIR region (The importance and relevance of plasmons will be discussed in Chapter 3.1.2). On the other hand, as already shown in **Figure 7**, neat Pd has a partially filled d-band, that overlaps the E_F. Zooming-in closer to energies around the E_F (**Figure 9**), we can see the evolution of the DOS, where the increasing Au content (in a Pd host) shifts the d-band of Pd below the E_F. The reduced solubility of H in a PdAu alloy that was discussed in Chapter 2.3, can be explained via the electronic structure. In the case of neat Pd, the (partially filled) d-band has many available states near E_F favorable for the hybridization of H s-orbitals[151]. Since the alloying with Au, shifts the d-band below the E_F the number of available d-states reduces, thus weakening the Pd-H interactions leading to reduced H-solubility (compared to neat Pd), and consequently an overall lower optical contrast[101,102].

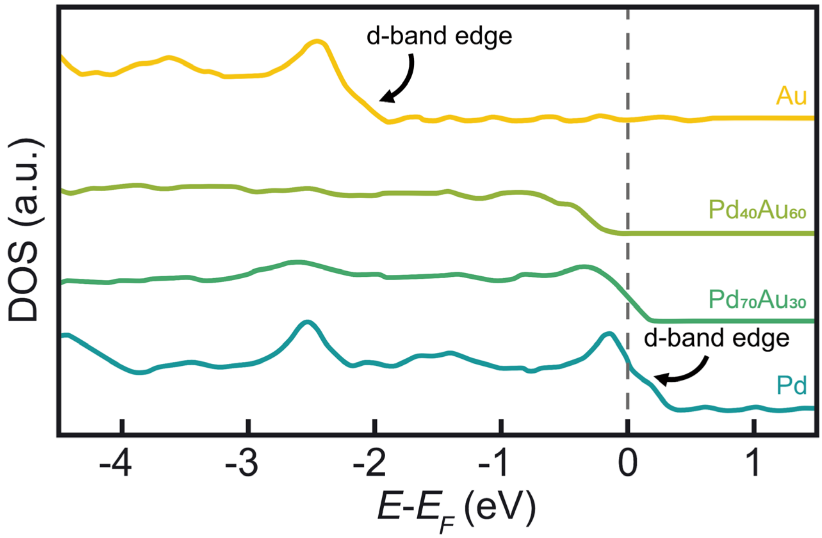

Figure 9: *Density of states (DOS) for Pd, Au and PdAu alloy nanodisks. As Au atoms replace Pd atoms in the lattice, the d-band is shifted below the E_F. The dashed line denotes the Fermi level (E_F) (adapted from ref.*[155]*).*

Finally, Pt ([Xe]5d^{9}6s^1) also has a partially filled d-band similar to Pd, where the d-band overlaps (and extends above) the E_F (**Figure 10**), therefore enabling strong adsorption of molecules such as H_2 and O_2, and weakening intermolecular bonds leading to dissociation[157-159].

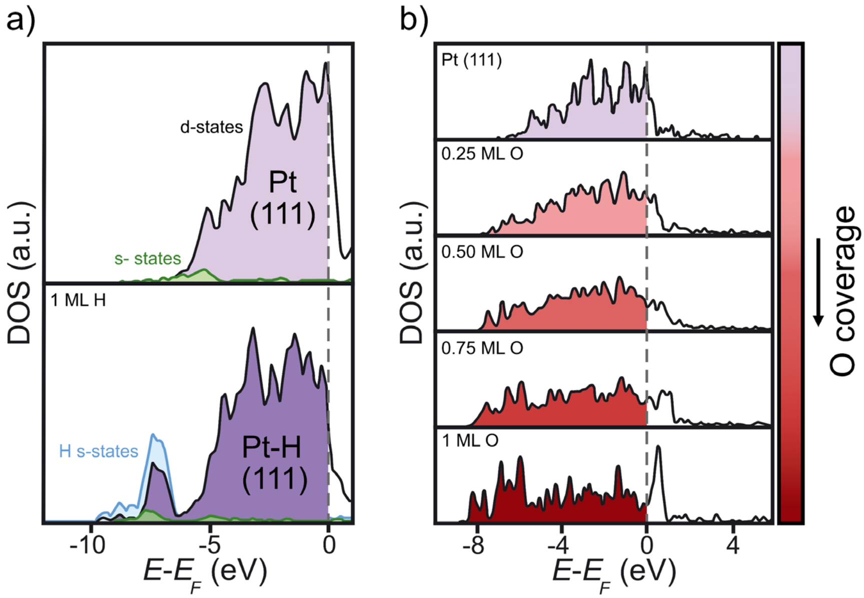

Figure 10: *a) Density of states (DOS) for a clean and a H-covered Pt (111) surface. The adsorption of H introduces s-states (hybridized with Pt's d states) increasing the DOS at ~ -7 eV, while the DOS at the E_F decreases and the d-band center shifts away from the E_F. (Adapted from ref.[157]). b) The DOS evolution with increasing coverage of O on a Pt (111) surface. As the coverage increases, the d-band broadens, and the center shifts away from the E_F. New states appear below and above E_F, referring to bonding and antibonding states of O. The dashed lines denote the Fermi level (E_F) (adapted from ref[158]).*

When H_2 adsorbs on a Pt surface, the DOS is altered, due to the hybridization of the H s-states and Pt's d-states and 6s orbitals[160], leading to the emergence of new H s-states at ~ -7eV (**Figure 10a**). Additionally, a reduction of the DOS at the E_F (i.e. shift of the d-band center below E_F) is a result of the chemical Pt-H bond which produces a chemical passivation of the surface, i.e. reduced reactivity for further H adsorption[157,160-162]. Similarly, in the case of O (**Figure 10b**), the increase in O coverage leads to a broadening of the d-band and a shift of the center away from the E_F, indicating a decrease in the strength of the Pt-O interactions with increasing coverage. Finally, new states appear below and above the E_F, a result from the hybridization of the O s- and p-states with Pt d-states[158].

3.1.2 Localized surface plasmon resonance

The localized surface plasmon resonance (LSPR) is an optical phenomenon that occurs primarily in metallic nanostructures, when the conduction electrons couple to an incident electromagnetic field (i.e. light) and collectively oscillate at specific frequencies[163] (**Figure 11a**). The key features associated with LSPR is that i) it refers to non-propagating excitations where the electric field is greatly enhanced at the surface of the particle, but quickly falls off with distance and ii) many metals (including the historically important metals such as Ag, Au and Cu) experience resonance conditions in the visible regime, thus allowing for their use in many applications, some of which date back to antiquity, like the Lycurgus cup[164,165] (**Figure 11b**).

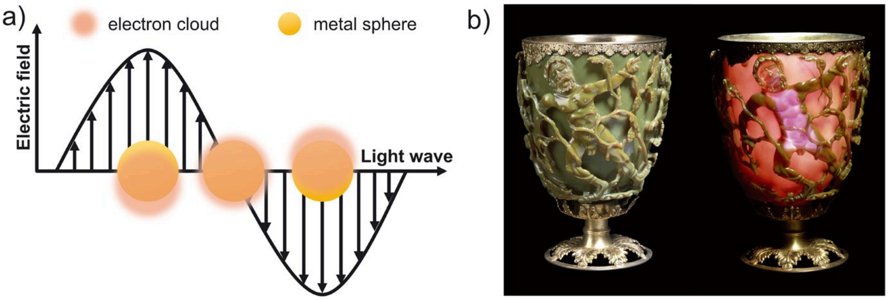

Figure 11: a) *Schematic depiction of the localized surface plasmon resonance (LSPR). Driven by the incident electric field, the conduction electrons of the metal sphere will oscillate collectively (resonance). b) The Lycurgus Cup, a relic from the late Roman period, showcasing the use of metal nanoparticles in glassmaking, exhibiting unique optical properties, such as different colors depending on the angle of the incident light. (© The Trustees of the British Museum. Adapted and shared under CC 4.0 license[165]).*

To understand the resonance conditions giving rise to this phenomenon we can first look at the simplest example of a small metal sphere, where the particle-light interactions can be described by the *quasi-static approximation*. Here the diameter *d* of the sphere is considered much smaller than the incident wavelength of light ($d \ll \lambda$). This ensures that the phase of the electromagnetic field is constant over the entire particle, allowing us to consider the simplified problem of a particle in a static electric field. The incident electromagnetic field induces a dipole moment $\boldsymbol{p}$ on the particle, which is defined as:

$$\boldsymbol{p} = \varepsilon_0 \varepsilon_m \alpha \boldsymbol{E_0} \quad (3.1)$$

Where ε_0 is the permittivity of free space, ε_m is the dielectric constant of the surrounding medium, $\boldsymbol{E_0}$ is the applied field, and α is the polarizability, which can be described as,

$$\alpha = 4\pi r^3 \frac{\varepsilon(\lambda) - \boldsymbol{\varepsilon_m}}{\varepsilon(\lambda) + 2\boldsymbol{\varepsilon_m}} \quad (3.2)$$

where r is the radius of the sphere and $\varepsilon(\lambda)$ is the complex dielectric function of the material. Polarizability describes how easily the electron cloud of a metal nanoparticle can be influenced by an external field, and as is apparent from Eq. 4.2 a resonance condition exists when $|\varepsilon(\lambda) + 2\varepsilon_m|$ is minimized or, in other words, when

$$\mathrm{Re}[\varepsilon(\lambda)] = -2\varepsilon_m \quad (3.3)$$

Based on that, the scattering (σ_{scat}), extinction (σ_{ext}), and absorption (σ_{abs}) cross-sections can be expressed analytically (for the case of a small metal sphere) using Mie Theory[163,166]:

$$\sigma_{scat} = \frac{k^4}{6\pi} |\alpha|^2 = \frac{8\pi}{3} k^4 r^6 \left| \frac{\varepsilon(\lambda) - \boldsymbol{\varepsilon_m}}{\varepsilon(\lambda) + 2\boldsymbol{\varepsilon_m}} \right|^2 \quad (3.4)$$

$$\sigma_{abs} = kIm(\alpha) = 4\pi k r^3 Im\left(\frac{\varepsilon(\lambda) - \boldsymbol{\varepsilon_m}}{\varepsilon(\lambda) + 2\boldsymbol{\varepsilon_m}} \right) \quad (3.5)$$

The total extinction cross-section represents the sum of absorption and scattering and therefore for a particle of volume V, it can be expressed as,

$$\sigma_{ext} = \sigma_{abs} + \sigma_{scat} = \frac{18\pi\varepsilon_m^{3/2}V}{\lambda}\frac{\varepsilon_2(\lambda)}{[\varepsilon_1(\lambda)+2\varepsilon_m]^2+\varepsilon_2(\lambda)^2} \tag{3.6}$$

where λ is the wavelength of light, and ε_1, ε_2 are the real and imaginary parts of the dielectric function of the material, respectively. As briefly described in Chapter 3.1.1, ε_2 is associated with losses and specifically energy dissipation in the form of absorption/scattering. As can be seen from Eq. 4.6, the resonance conditions (maximum σ_{ext}) are achieved when $\varepsilon_1 = -2\varepsilon_m$, leading to the modified Eq. 4.6 at resonance:

$$\sigma_{ext}^{res} = \frac{18\pi\varepsilon_m^{3/2}V}{\lambda_{res}}\frac{1}{\varepsilon_2(\lambda_{res})} \tag{3.7}$$

From Eq. 4.7 it is clear that the size of the extinction cross-section and therefore the strength of the particle-light interactions is determined by both the material's properties, i.e., size, shape, ε_2, and the surrounding medium. Additionally, materials with inherently small ε_2, such as Au and Ag, scatter light more efficiently and therefore are widely used in many plasmonic-related applications[166,167]. It is important to remind the reader that while this approximation only strictly applies for $d \ll \lambda$ $(d < 10nm)$, a good approximation can also be provided for larger particles.

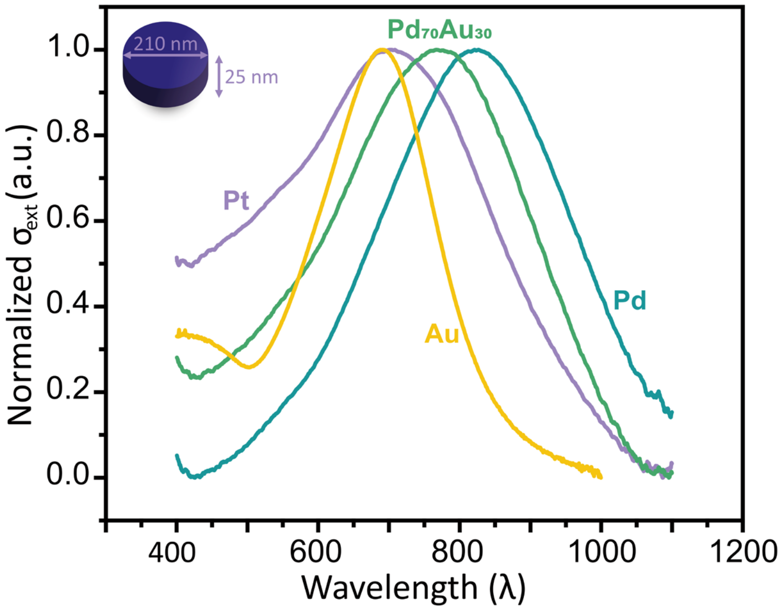

Figure 12: *Normalized extinction cross-section (σ_{ext}) for Pd, Au, $Pd_{70}Au_{30}$, Pt fabricated nanodisks, of identical nominal size (210 nm diameter, 25 nm height) on fused-silica substrates. The extinction exhibits clear peaks, whose widths are determined primarily by the imaginary part of the dielectric function of each material (ε_2), as well as the size distribution associated with the nanodisk fabrication. The position of the peak is determined by the size, shape, surrounding medium, as well as the real part of the dielectric function (ε_1) as described in Eq. 4.6.*

In the context of this thesis and looking at the σ_{ext} in the far-field, i.e. measuring with a spectrometer in the visible regime, the resonance appears as a broad peak. This is reasonable by looking again at Eq. 4.7. Even at resonance condition the σ_{ext} remains a finite number, since ε_2 will always be a positive number and there will always be losses associated with the material. **Figure 12** shows the normalized σ_{ext} from samples comprised of quasi-random arrays of Pd, Au, $Pd_{70}Au_{30}$, and Pt nanodisks (i.e. an average σ_{ext} of all the light-illuminated nanodisks in the respective array), fabricated on fused silica substrates (details regarding the fabrication method and measuring technique in Chapter 5 & 6, respectively). The nominal size of these disks is the same, i.e. 210 nm in diameter, and 25 nm in height. As depicted, the peaks appear broad, where the width is determined by the ε_2 of each material, associated with plasmon damping. Furthermore, a collection of small metallic nanostructures, in most fabrication methods (including the method used in this thesis), would yield a size distribution that in turn will translate to slightly different resonance conditions (due to the volume factor in Eq. 4.7) and therefore a broadening of the plasmon peak.

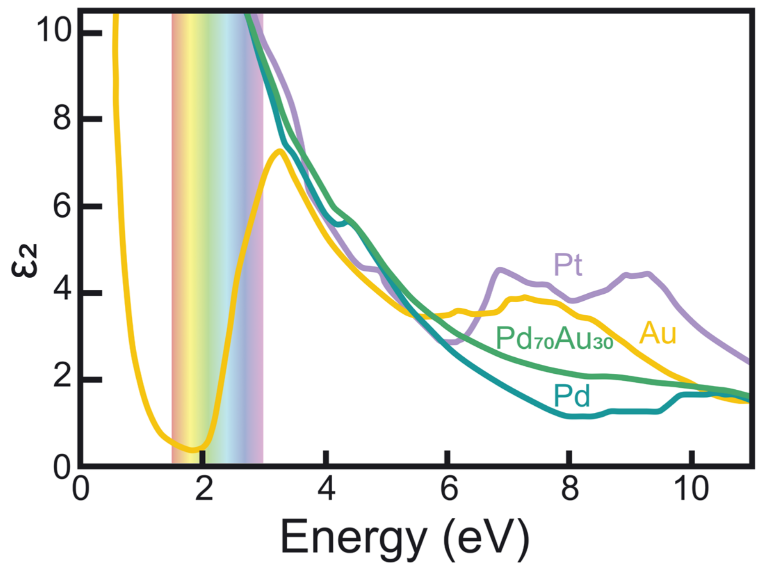

Figure 13: *TDDFT calculations for the imaginary part (ε_2) of the dielectric function for Pd, Au, $Pd_{70}Au_{30}$, and Pt. The gradient rectangle represents the visible regime. Au has the smallest ε_2 in the visible regime, resulting in weaker plasmon damping and therefore efficient light extinction (adapted from ref.[155]).*

It is evident from **Figure 11**, that Au possesses the strongest plasmon peak, i.e. the narrowest, of all four, which can be traced back to its low ε_2. **Figure 13** shows the calculated[155] ε_2 for all four materials, with Au exhibiting the lowest ε_2 in the visible regime, with a minimum at ~2 eV (620 nm) and sharp rise in ε_2 at higher (lower) energies (wavelengths), associated with the position of the d-band in respect to Au's E_F, and the d-sp interband transitions that occur, leading to efficient absorption of light in the blue region.

When it comes to plasmonic sensing in general and H_2 sensing in particular, by controlling the nanostructures' size, shape, surrounding medium and material composition one can tailor the optical properties in a way to optimize optical contrast and achieve better sensor performance. On that note, and beyond the description given above, collective light-particle interactions in particle ensembles can also be achieved, such as near-field enhancement due to coupling effects between ordered, neighboring particles.[45,168]

3.1.3 Plasmonic H_2 sensing

As described in the previous section, the basis for LSPR sensing stems from the strong interaction of light with metal nanoparticles, and the dependence of the resonance conditions on both the material's properties and the surrounding medium. Additionally, due the plasmonic effect, a field enhancement is achieved in the vicinity of the particle (dependent on the material's dielectric function), which allows for enhanced optical effects and therefore ultrasensitive detection[169,170].

In an LSPR-based H_2 detection scheme, it is possible to utilize both changes in the sensing material, and changes in the surrounding medium. For the former, named *direct* sensing and in the case of a hydride-forming material, the absorption of H_2 leads to i) changes in the electronic properties of the material, and therefore changes in the optical properties. In the case of Pd that leads to a decrease in the σ_{ext} and consequently a shift of the resonance conditions due to changes in the dielectric function. Similarly for Pt, the adsorption of O and H lead to changes in the electronic properties of the surface and are expressed in different positions of the plasmon peak with respect to wavelength. ii) The absorption of H, as described in Chapter 2, leads to structural changes in the particle, which are manifested in a change of the resonance conditions (through the geometrical volume factor) and therefore further shift of the peak. For the latter case, called *indirect* sensing, changes in the surrounding medium can lead to changes of the resonance conditions and consequently shift of the plasmon peak. This relationship can be derived from the Drude model[166], where the peak position is proportional to the refractive index of the medium, i.e., $\lambda_{res} \propto n_m$.

In most cases this is utilized by placing a reactive (towards specific molecules) material, within the plasmonic near-field of an inert plasmonic nanoparticle, e.g. Au or Ag. In this way, the plasmonic nanoparticle acts as an antenna, which can detect changes in the "active" element. Particularly for H_2 sensing, a small hydride-forming particle (e.g. Pd) can be placed next to a larger Au or Ag particle and thus "sense" the absorption of H. This is particularly useful from an application point of view, since on one hand, the smaller size of the sensing particle, would both introduce higher surface-to-volume ratio (more dissociation sites), decrease the absorption time (shorter diffusion path) and therefore increase the response speed, but on the other hand the small size would dramatically decrease the optical cross-section and shift the plasmonic peak outside of the visible range (in the UV). Therefore, the use of an antenna nanoparticle, with its plasmonic features in the visible regime allows for fast kinetics with high sensitivity. This method has been used in various applications such as biosensors[171] and gas sensors[172] including H_2 detection[173,174].

From a technical perspective, the detection of H_2 can be achieved by multiple spectral descriptors including the shift of the peak ($\Delta\lambda_{peak}$), the change in peak extinction (ΔExt_{peak}), or the change in the FWHM (**Figure 14**). Another descriptor which takes into account a larger portion of the peak is the centroid[175]. The position of the centroid differs from the actual peak position since the plasmonic peak is asymmetrical. The centroid is calculated by fitting a high-degree polynomial to the data (20^{th} order). This approach has been demonstrated to provide the least noise, i.e. highest SNR, due to the elimination of external influences, such as intensity variations from the light source, or possible changes in lens alignment which are wavelength-independent disturbances[175]. It is important to note that these descriptors are proportional to the H_2 pressure and therefore the hydrogen concentration in the hydride forming metal nanoparticle, and that they are universal for any to-date studied Pd-based alloy, thus making them highly useful for H_2 concentration prediction/detection[102].

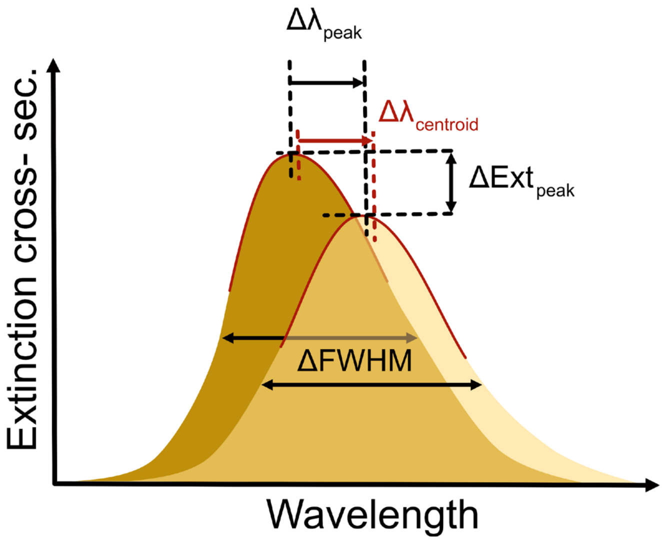

Figure 14: *Schematic illustration of the plasmonic peak before (dark color) and after (light color) H-absorption. The different peak descriptors typically used as sensor readouts are depicted, such as the shift of the peak ($\Delta\lambda_{peak}$), the change in peak extinction (ΔExt_{peak}), the change in the FWHM ($\Delta FWHM$) or the shift of the centroid position ($\Delta\lambda_{centroid}$). The latter expresses the center of mass of the peak, and is calculated via fitting of a 20^{th} degree polynomial*[175].

3.2 Catalytic H_2 sensing

As already discussed in Chapter 1, catalytic H_2 sensors are one of the most common type of sensors on the market. The operation principle is based on the catalytic properties of the sensing element, and specifically on the combustible reaction of H_2 and O_2 on its surface, leading to the release of heat. This reaction, which is highly exothermic (described in Chapter 2.4.1) leads to an increase in temperature which can be directly observed[37], or is used to induce a change in resistance (Pellistor-type sensors[35]) or generate an electrical signal (thermoelectric sensors[36]). In this section I will present the use of Platinum in catalytic H_2 sensing and introduce the Pt-based dual function catalytic/plasmonic H_2 sensor concept I have developed as part of this thesis.

3.2.1 Platinum as a catalytic H_2 sensor

Pt has long been the favored material in catalytic H_2 sensors, due to its unique ability to effectively catalyze the HOR. Traditionally, Pellistor-type sensors consist of a Joule-heated wire (often Pt), and a support material (usually a porous ceramic) coated with a catalyst layer (Pt or Pd). The catalytic combustion of H_2 and O_2 results in a temperature increase in the wire, causing an increase in resistance[13]. One of the main drawbacks of Pellistor-type sensors is the high-power consumption requirements associated with their high temperature of operation. Additionally, due to the high temperature requirement these sensors are non-selective to H_2 and can combust other gases as well. Finally, due to the nature of this detection scheme, these sensors can only be operated in an oxygen-containing environment. However, in the last years, advances in miniaturization have allowed for the fabrication of smaller devices incorporating microfabricated heating elements, thus significantly reducing power consumption. As an additional advantage, miniaturization of the device in general and the microheater in particular leads to a reduction in the thermal response time[38,176,177].

Another type of catalytic H_2 sensors are thermoelectric sensors based on the Seebeck effect, where a change in temperature between two points causes an observable voltage difference[13]. Unlike the Pellistor-type, these sensors do not require an external power source and can operate at significantly reduced temperatures compared to Pellistor-based. By primarily employing Pt as the catalyst element, they are also highly selective, since only H_2 that can be oxidized by Pt at low temperatures.

The catalytic properties of Pt make it an attractive candidate also in other types of sensing technologies such in resistance-based sensors[24,25,133-136] as described in Chapter 2.4.

3.2.2 Dual function catalytic/plasmonic H_2 sensing

A dual function catalytic/plasmonic H_2 sensor utilizes the capabilities of a catalytic material in an LSPR-based detection scheme. In the context of this thesis, and specifically in **Paper I**, we employ Pt nanodisks fabricated on a fused silica substrate and use them in an optical transmission-based spectroscopy setup. Even though Pt is not one of the "best" plasmonic materials in terms of losses and "sharpness" of the plasmonic peak, as described in Chapter 3.1.2 and seen in **Figure 13**, where the ε_2 is large in the visible regime (similar to Pd), a broad plasmonic peak is still present (**Figure 12**) and can be utilized in LSPR-based H_2 sensing. When investigated in an oxygen-rich environment (here synthetic air background gas), the HOR catalytic activity of Pt is evident, as a blue-shift of the LSPR spectrum is observed always in the presence of H_2 and found proportional to the applied H_2 concentrations (Figures 4 &5 in **Paper I**). Specifically, in **dry conditions**, the blue-shift can be associated with changes on the surface, where the initially O-covered Pt surface is i) reduced due to the dissociation and reaction of H with O to form H_2O and ii) replaced by a partially H-covered surface. This relative change of the surface coverage with O- and H-species modifies the electronic structure of the Pt surface and consequently alters the real part of its dielectric function, ε_1, which is responsible for the resonance condition described in the *quasi-static approximation* ($\varepsilon_1 = -2\varepsilon_m$). Comparing the 2 different states of the Pt surface, i.e. O-covered and H-covered, we can make the following observations: When O_2 dissociatively adsorbs on a clean Pt surface it withdraws electrons from the Pt surface, due to its high electronegativity. This leads to a reduction in the local (surface) electron density, an increase of ε_1 (associated with the "metallic" character of the material) and consequently a red-shift of the plasmon resonance. On the other hand, H-adsorption and dissociation is accompanied by charge donation to the Pt surface, leading to an increase in the local electron density, a decrease of ε_1 and hence a blue-shift of the plasmon resonance.

When measured in **humid conditions**, the Pt nanoparticle surface is initially covered with mono/multilayers of water, as well as -OH groups bound to the surface. This presence of adsorbed H_2O on the Pt surface (either molecularly or dissociatively adsorbed, as described in Chapter 2.5) will induce a red-shift of the plasmon resonance compared to a non-water-covered Pt nanoparticle surface, as derived from the Drude model[166] where $\lambda_{res} \propto n_m$. As a consequence, in these conditions two processes/sensing mechanisms are expected to occur at the same time: i) The HOR that takes place in the presence of O_2 and H_2 in humid environment and is highly exothermic, leads to a local increase in temperature on the Pt particles, which thermally desorbs the H_2O layer(s) that initially were present. This desorption leads to a blue-shift of the plasmon peak since the refractive index of the Pt nanoparticle surroundings is reduced. ii) the HOR that occurs in the presence of H_2 reduces the O-coverage of the surface and occupies a sizable fraction of the surface with H, which in concert is responsible for further blue-shifting of the peak according to the mechanism explained above for dry conditions. Taken together, this explains the increasing sensor response magnitude to a given H_2 concentration with increasing humidity that we observed in **Paper I**.

4 Deep learning for optical sensing

Even though the use of Artificial Intelligence (AI) has become more popularized in recent years, the groundwork for what AI is today began in the early 1950s, where both Alan Turing[178] and John McCarthy are considered to be the fathers of AI. The term was coined by McCarthy, who in 1955 held a workshop in Dartmouth College on "Thinking Machines".

Over the years, progress in AI, and more specifically in Machine Learning (ML) techniques, had been small, until the first breakthrough at the end of 1980s. LeCun et al.[179] demonstrated one of the first uses of a Convolutional Neural Network (CNN) used for handwritten zip-code recognition. After that, progress has been exponential; From the revolutionizing image classification using a deep CNN (marking the beginning of modern Deep Learning (DL)-based techniques) developed by Krizhevsky et al. in 2012[180], the creation of chatbots and Large Language Models (LLMs)[181] such as ChatGPT, image generators[182] like Dall-E and Midjourney, to the use of Deepfake technology in mainstream media and art[183].

Besides these well-known applications of AI in society, in recent years, the use of AI in experimental and theoretical science has taken tremendous steps, transforming the landscape of scientific research. Many fields of science and industry are implementing AI-based methods, like in autonomous driving[184], medical diagnosis[185], biology[186], astronomy[187], meteorology[188], or material science[189,190], to name a few (An excellent popular science video titled "*The Most Useful Thing AI Has Ever Done*" can be found in ref.[191])

It's important to emphasize that the term 'AI' is a broad field referring to intelligent machines that can perform tasks like humans do. As seen in **Figure 15**, within the context of AI different subfields exist. Machine learning (ML) which is the main subset of AI, was first introduced by A. L. Samuel in 1959[192], defining the field as a way to enable the learning of patterns and the consequent decision making from computers, without explicit programming. Instead a process called *training* is used, to handle the problem at hand[193] (e.g. a game of checkers[192]). ML has given birth to different technologies including brain-inspired computation methods. The idea is that an algorithm/program based on that, would contain features similar to how a human brain works, i.e. connecting, artificial neurons and synapses. Within the brain-inspired subset, Spiking Neural Networks (SNNs) are the ones that most closely mimic the behavior of human brains; here, communication within the neurons is based on spike-like pulses, where the relationship between both the temporal and spatial parameters are taken into account (instead of just the amplitude of the spike). The idea with SNNs, in contrast to traditional NNs which are known to be computationally demanding, is to provide a much higher energy efficiency, similar to that of the human brain[194,195].

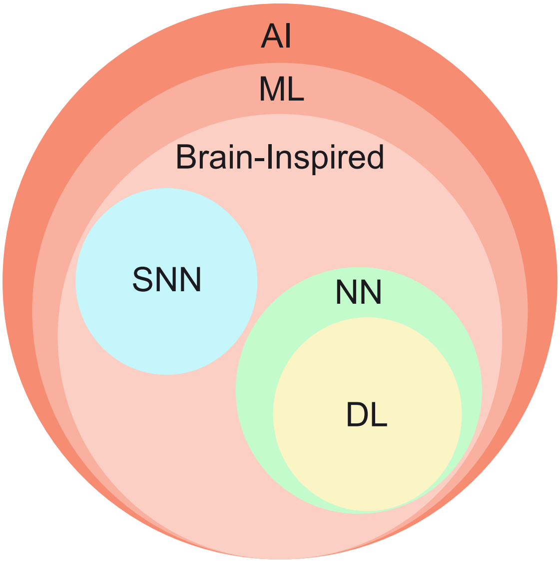

Figure 15: *Euler diagram of the subsets within the broad field of Artificial Intelligence (AI). Machine learning (ML) encompasses brain-inspired processes such as Spiking Neural Networks (SNNs) and traditional Neural Networks (NNs) which include Deep learning (DL) (adapted from ref.[193,196]).*

Within the NN subset, the DL method utilizes neural networks with multiple layers, to learn complex patterns and features from data automatically. This process is the foundation of many modern, state-of-the-art AI, where the simplest (and historically significant) example are CNNs, which are designed to process, grid-like data (e.g. images)[197].

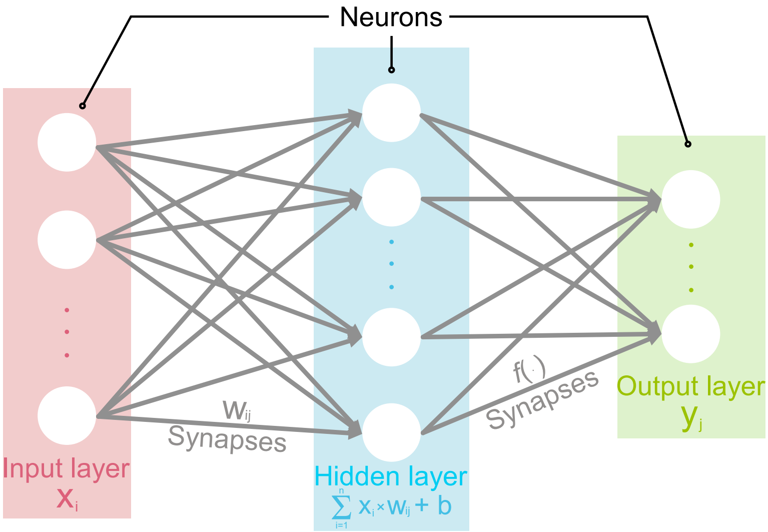

Figure 16: *A schematic of a simple neural network. Neurons in the input layer transmit the information through the synapses ($w_{ij} \times x_i$), to the middle layer often called the hidden layer. The weighted sum from the hidden layer is propagated to the neurons in the output layer (y_j) after being multiplied by a non-linear activation function (f). In more complex NNs multiple hidden layers are present, which is the basis for Deep Learning (DL) (adapted from ref.[193]).*

Going back to the fundamentals of NN-based technologies, the artificial neuron and synapse stand as the basic elements. In a simplified biological neural network example, a neuron receives an input signal from another neuron through synapses. Above a certain signal threshold, the neuron will activate, and the information will be transmitted to the next neuron, again through a synapse. The synapse therefore allows for the transferring of information from one neuron to another. In a similar way, the artificial neurons compute a weighted linear function, by receiving input directly from the input data or from other neurons (input layer), and multiplying that with a weight, which represents the importance of the input (in terms of neuron decision-making). Finally, a bias is applied representing the activation threshold, as well as a non-linear function (activation function) used to introduce non-linearity into the model and enable the learning of complex patterns[193]. The computation at each layer is the following,

$$y_j = f \cdot (\sum_{i=1}^{n} w_{ij} \times x_i + b) \qquad (4.1)$$

where w_{ij} represents the weights transferred from each neuron in the input layer, x_i and y_i are the inputs and outputs respectively, b is the bias (which represents the activation threshold) and f is the non-linear activation function.[193] A schematic of a simple neural network can be seen in **Figure 16**. As previously mentioned, in the sphere of NNs (**Figure 15**) and relevant for this thesis, the subset of Deep Learning (DL) exists, which utilizes multiple hidden layers for computing. This way the algorithm is capable of learning significantly more complex patterns, especially when the complexity and size of the initial dataset is large. Networks that fall under this category are called Deep Neural Networks (DNNs) and are the topic of this thesis.

4.1 Purpose of deep learning in sensing

As aforementioned, AI-based technologies in general, and DNNs in particular, have already been implemented in many fields of science including sensing[198]. The need for the implementation of deep learning approaches for data acquisition/treatment, stems from the fact that often the raw data acquired from sensor systems are not only complex but also high in volume. A prime example is computer vision-based sensing, such as autonomous driving[199] or face recognition[200]. In the former case, multiple sensors are deployed on a vehicle, including cameras, LiDARs, GPS units or ultrasonic sensors, among others, that continuously collect relevant data (e.g. images, satellite position, spatial parameters, etc.). This huge amount of information is fed to a DNN-based model (in real-time) capable of processing and consequently deciding on actions based on object/pedestrian detection, or for collision evasion[199]. Other important sensor- and DL-based applications include wearable health sensors[201] or environmental monitoring systems[202].

In the context of hydrogen sensing, and regardless of the detection principle, the ability to detect minute quantities of H_2, especially in chemically complicated environments, where multiple other gas species are present and there exists a risk for cross-sensitivity and/or deactivation, is not only particularly challenging, but also technologically relevant. That is because many conventional approaches of analysis are limited by the fact that i) the H_2-induced signal change is so small that is hidden within the background noise, and/or ii) the changes in the descriptor(s) used for H_2 detection are particularly complex, especially when the sensor is cross-sensitive to other species present in the gas phase. The use of DNNs therefore has the potential to allow for the identification of these complex patterns, and distinction of signal changes from background noise, through the training of DL-based models on various environmental conditions (e.g. different gas species and concentrations). This is also particularly relevant in spectroscopy-based optical sensing, such as plasmonic hydrogen sensing in focus in this thesis, where the acquired data, i.e. spectra, contain useful information across the entire wavelength range, that are most often collapsed into a single descriptor when using conventional data analysis (**Figure 17**). Additionally, DNNs are expected to be able to learn and extract information from the relationship between H_2 gas concentrations and the temporal evolution of the spectral information which is particularly useful for fast and accurate predictions.

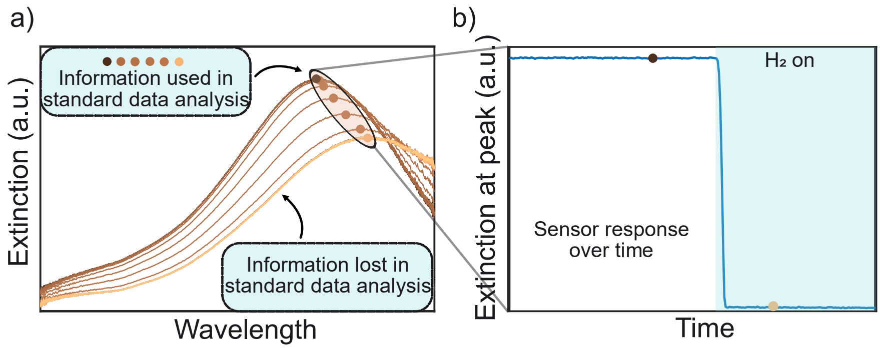

Figure 17: *Example of the optical response from a Pd nanoplasmonic sensor. a) Extinction spectra at different points in time (during a H_2 pulse) showing the evolution of the optical response. In a standard data analysis method, the spectra are usually collapsed into a single descriptor (here the extinction at peak position is shown as an example), and the remaining spectral information is left unused. b) The sensor's response to H_2 can be extracted by tracking the peak extinction value over time in a standard analysis method.*

There are already a few examples of DL approaches used in H_2 sensing; Cho et al[203] investigated the potential of a DNN used to analyze signals from chemical sensors of different sensing elements (Au, Cu, Mo, Ni, Pt, Pd) with the goal to identify hidden patterns in the background noise signal, that can further enhance the sensing capabilities below the intrinsic LoD. As a test case system, they used H_2 gas (in N_2) and report a signal detection within the noise at 10 ppm. Another example involves the work of Lin et al.[204], who used a CNN for acceleration of the response time in a Pd-based plasmonic sensor, measured in the range of 0.03-4 % H_2 showing up to 3.7 times enhancement of the response speed, 5.3 times reduction in the LoD and a maximum factor of 9.3 increase in the signal-to-noise ratio (SNR), however in an idealized vacuum/H_2 system.

To further showcase the potential of DL in H_2 sensing we have investigated both the acceleration of state-of-the-art nanoplasmonic H_2 sensors in technologically relevant environments (**Paper II**), and its use in analyzing data acquired in complex environments, such as high humidity, where we achieve both a reduction in the LoD and the elimination of the negative influence of H_2O on the sensor (**Paper III**). In the next subsections I will present the DL architectures used to achieve that and summarize the key results.

4.2 Acceleration of H_2 sensors

To accelerate the performance of nanoplasmonic H_2 sensors, it is important to employ an architecture that can consider the entire spectral data provided by the sensor, i.e., its light transmission, extinction, reflection or scattering spectrum, in an extended timespan. This is possible via the combination of two principal architectures:

- **Recurrent Neural Networks (RNNs):** An RNN is a type of DL architecture that is designed to treat sequential data. Unlike in traditional NNs, it contains a built-in memory that allows it to process short time-series data, where the model uses past information to make decisions. RNNs process data one at a time, where the information of one layer is passed onto the next. To improve on that and allow for handling of long(er) sequences, a new variant of an RNN has been developed, the

Long Short-term Memory (LSTM). This architecture builds on the standard RNN and eliminates long-term dependency issues via the use of gates. These gates basically control which past information to forget, and which new information to store and send to the next layer.[205]

- **Transformers:** Initially developed by Vaswani et al.[206] in 2017, transformers are DL architectures that are designed to handle data *in parallel*, making them significantly more powerful for applications involving sequential and time-evolving data, and also much faster than sequential RNN architectures. Transformers rely on the concept of *self-attention* in order to determine the relationship between sequential data points. They do so by computing attention scores, for each input sequence, using three parameter matrices that contain an encoded representation of the input data[207]. Simply put, two main elements make up a transformer: the encoder, that processes the input data (sequence) and extracts meaningful information, such as the relationship between data points, and the decoder that ultimately collects the encoder's output and produces the final prediction. Within those two elements, a stack of identical layers exist, where the self-attention mechanism is at its core.[207,208]

The architecture used in **Paper II**, is a *Long Short term Transformer (LSTR)* which combines the strengths of a transformer and an LSTM model, i.e., the capabilities of parallel processing and long-range sequences handling. One of the main features of this architecture is the so called Local-Global attention mechanism, where the attention is divided in two components; local attention is focused on analyzing fine details in short time windows while global attention takes into account long-range dependencies. In the context of a nanoplasmonic H_2 sensor, which is presented in this thesis, this is important for several reasons:

i) The intrinsic noise in the raw data associated with both the light source and the spectrometer, is in many cases comparable to the magnitude of the signal change caused by the presence of H_2. In the case of distinct H_2 pulses of decreasing concentration, the LoD is limited by the noise level, while also in cases of a simulated slow and gradually increasing H_2 leak, the time of detection and LoD are determined by the SNR. To overcome this, the selection of an LSTR architecture is crucial, since their ability to model long data sequences allows it to differentiate trends in the extinction spectrum associated with the presence of H_2, from noise, and thus accurately predict the H_2 concentration.

ii) For a robust performance of the LSTR model, preprocessing techniques are used for the input extinction spectra, that are then fed to the LSTR model.

iii) Due to the nature of the application, i.e., a H_2 sensor developed for safety applications, it is important to provide robust and reliable predictions, as well as information relating to the uncertainty of those. Therefore, combining multiple LSTR models as an *ensemble*, not only yields rapid H_2 concentration predictions, but also provides information on the computed mean and standard deviation of the ensemble's prediction.

The model presented in **Paper II** is therefore named *Long Short-term Transformer Ensemble Model for Accelerated Sensing (LEMAS)* and is shown to excel in two distinct ways: i) The model is able to achieve up to a 40-fold improvement in the response time, compared to a standard analysis, for measurements in the 0.06-1.97 vol.% H_2 range (in Ar), while also providing a prediction on its accuracy due to the ensemble feature. Therefore, LEMAS can provide an additional metric, the LEMAS settling time t_s^{LEMAS}, which refers to the first time where the predicted H_2 concentration is within ±10% of the target value, and the relative standard deviation is smaller than 10%. This metric is used to complement the predicted response time, t_{90}^{LEMAS}, and is particularly useful in cases of over- or underprediction. Additionally, and quite interestingly, the predicted response time from LEMAS is H_2 concentration independent, a striking difference from the standard analysis method, where the response time increases with decreasing H_2 concentration. This effect is related to the intrinsic kinetics of the sensing material which is highly dependent on H_2 pressure, where at low H_2 concentrations (within the α-phase), the response time is dependent on the diffusion rate which in turn is determined by the amount of H atoms that dissociate and diffuse into the material, per unit time. Therefore, with decreasing H_2 concentration, less H_2 dissociation and diffusion events take place leading to increased response times[209]. ii) in cases of simulated H_2 leaks, LEMAS can predict both the presence and amount of H_2 much faster, primarily due to the considerably lower noise that LEMAS predictions have, compared to the standard analysis. This way LEMAS gives a lower LoD (defined here as the smallest

H_2 concentration required to discern but not quantify the presence of H_2), especially at low leak rates, and an overall lower limit of quantification (LoQ), which refers to the minimum amount of H_2 required to give an accurate prediction of the concentration.

4.3 Reducing the LoD in high humidity

As already described in previous chapters, humidity plays a significant role in H_2-related technologies including sensing. Many applications where a sensor needs to be deployed, are characterized by complex environmental conditions, such as high humidity (e.g. gas feed in fuel cells). Additionally, and more specifically in the context of hydride-based H_2 sensors, humidity can significantly impact the performance of hydride-forming sensors and consequently affect important metrics, such as the LoD, response time or baseline signal stability.

In **Paper III** we investigate this issue by first presenting the effect of humidity (in synthetic air) on a PdAu nanoplasmonic H_2 sensor, where the response magnitude decreases with increasing relative humidity (RH), highlighted by the almost complete deactivation at 80% RH and 30 ºC. In addition to that, the presence of H_2O on the surface of the particles not only occupies surface sites favorable for H_2 dissociation, but also partially dissociates forming OH groups. This results in an important competing effect, as discussed in chapter 2.5, where dissociated H atoms on Pd-based sensors are both absorbed into the lattice, and catalytically react with adsorbed O and OH species to form H_2O. The sensor therefore exhibits a combined effect of a spectral red-shift associated with hydride formation, and a spectral blue-shift associated with the HOR. The equilibrium of this effect is shifted towards the latter in cases of high RH, and especially for low H_2 concentration, where all the dissociated H atoms are consumed for the HOR. In terms of sensor performance this translates to ambiguous results at low concentrations, effectively increasing the LoD above the desired 0.1 vol.% H_2, even at elevated temperatures where the negative effect of H_2O is less pronounced.

To mitigate this effect, we employed a *Deep Dense Neural Network* (DDNN) architecture, a specific type of DNN where every neuron in one layer is *fully connected* to every neuron in the next layer. In the context of this work, each neuron in the input layer represents each input data of the extinction spectrum (i.e., each extinction value calculated from each raw intensity data acquired from the spectrometer), thus incorporating the entire spectral information. To handle the high sensitivity to noise and drifts associated with that, we include batch normalization layers[210], a technique used in DL, to improve the stability, as well as speed up, the training of the model, by normalizing the weighted inputs received from neurons. Additionally dropout layers[211] are implemented, a regularization technique that helps prevent overfitting, by randomly resetting network weights during training. This ensures that instead of relying on specific neurons, the network is able to learn more robust correlations resistant to random variability. By employing the DDNN-based model we were able to achieve as low as 600 ppm LoD in 80% RH (in synthetic air) at 80 ºC operating temperature, thus meeting the DoE performance target for 0.1 vol.% H_2 in humid air.

As the final aspect of the sensor's evaluation, we also investigated the long-term performance and stability, under constant high humidity. Here the DDNN architecture was replaced by a Transformer (previously described in chapter 4.2), since it is tailored to handle longer sequences. Another aspect of this investigation is also to understand the model's predictive accuracy outside of the conditions used for training. We reveal that the Transformer model's performance deteriorates when used in conditions different than what it was initially trained for, however an issue that can easily be mitigated by incorporating new data into the training (in this context a wider range of H_2 concentrations/RHs). The re-trained Transformer model is therefore able to achieve 100 ppm LoD for H_2 at 80% RH in synthetic air, thus exceeding the DoE target of 0.1 vol.% H_2 by one order of magnitude, and showcasing the opportunities provided by employing a NN-based data analysis in a H_2 sensor, regardless of the underlying sensing mechanism.

5 Nanofabrication by Hole-Mask Colloidal Lithography

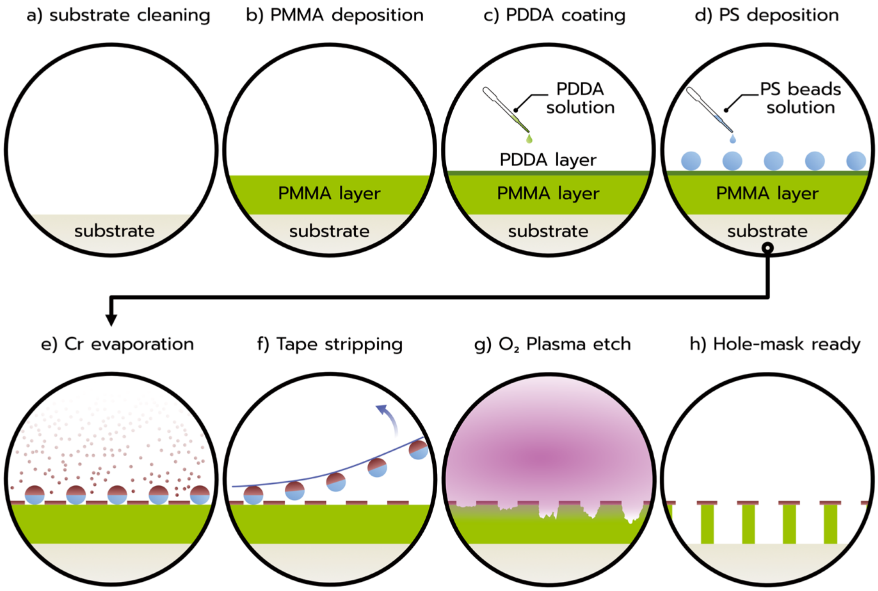

Figure 18: *Schematic illustration of the steps followed during the hole-mask colloidal lithography (HCL) process: a) substrate cleaning, b) PMMA deposition via spin-coating, c) applying a positively charged PDDA coating, d) PS bead electrostatic self-assembly, e) Cr deposition via e-beam evaporation, f) tape-stripping to create exposed areas at the former positions of the PS beads, g) O_2 plasma etch through the exposed areas to create holes. The final mask is shown in h).*

The samples used in all appended papers, were fabricated using hole-mask colloidal lithography (HCL), initially developed by Fredriksson et al.[212]. A schematic illustration of the nanofabrication process is presented in **Figure 18**. HCL is used to create quasi-random arrays of nanostructures, where one of its main advantages is the scalability aspect. Due to the use of a polystyrene (PS) beads solution from which the PS beads electrostatically self-assemble on the surface, which is the basis for the mask, substrates ranging from a few cm to large scale wafers take the same time to fabricate, allowing for high throughput. This also makes it an attractive and cost-effective method of producing masks that can later be used to fabricate nanostructures of different materials. All of the nanofabrication took place at Chalmers' cleanroom facilities (MyFab).

a) *Substrate cleaning:* In this thesis, I have used fused silica or Si substrates (10×10×0.5 mm^3). The fused silica substrates are used for optical transmission measurements, while the Si substrates are used for scanning electron microscopy (SEM) imaging, due to their higher conductivity, which eliminates charging effects that occur when imaging insulating substrates (see Chapter 6.1 for further details). The substrates are initially cleaned in an ultrasonicator in 2 steps; first for 5 minutes in acetone, followed by 5 minutes in isopropanol (IPA). The substrates are then blown-dried using N_2 gas. The purpose of the cleaning process is to remove dust and organic compounds that could have been accumulated during pre-processing (e.g. dicing).
b) *PMMA deposition:* Polymethyl methacrylate (PMMA) is deposited as a sacrificial layer, via spin coating, where I used an anisole-diluted PMMA (4 wt.%, Mw = 950 000, Microlithography Chemicals Corp.) solution. The substrate is placed on the spinning chuck and a few drops of the solution are applied. The final thickness is determined both by the solution itself (i.e. viscosity, concentration) and by the spinning speed. In this case, ~260 nm of PMMA layer is acquired by spinning at 2000 rpm for 60 seconds. The next step is to soft-bake the coated substrate at 170 ºC for 3 minutes, in order to evaporate any remaining solvent. Finally, the coated substrate is subjected to a short (5 seconds) oxygen plasma treatment (50W, 250 mTorr, 10 sccm) to reduce surface hydrophobicity.
c) *PDDA coating.* The next step is to deposit a solution of positively charged Poly(diallyldimethylammonium chloride) (PDDA). To acquire a very thin layer, PDDA (Mw = 100 000 – 200 000, Sigma Aldrich) is diluted in H_2O, achieving a concentration of 0.2 wt.%. in H_2O. The solution is drop-cast onto the PMMA layer, using a pipette and is then incubated for 1 minutes, followed by washing in Milli-Q water. Finally, the substrate is blow-dried with N_2 ensuring the formation of a thin PDDA layer.

d) *PS deposition.* A negatively charged PS bead solution (0.2 wt.% in H_2O) is drop-casted onto the positively charged PDDA layer. This ensures adhesion of the PS beads to the surface due to electrostatic attraction. On the other hand, the PS beads repel each other, and thus electrostatically self-assemble into a quasi-random sparse monolayer, with short-range ordering. To allow that, the drop-cast solution is incubated for 2 minutes followed by a 10 second rinse in Milli-Q water and finally blow-dried in an N_2 gas stream. The surface coverage of the PS beads can be controlled by adjusting the beads concentration in the solution. In this thesis (where we exclusively used a 0.2 wt.% PS bead solution) the surface coverage on the sensor chips is 13-14%. **Figure 19** depicts a side-view SEM image of PS beads (140 nm) self-assembled onto a surface where in some cases, agglomerates (e.g. bead dimers) can also occur, highlighted in the figure by the red boxes, and which will be transferred to the final mask.

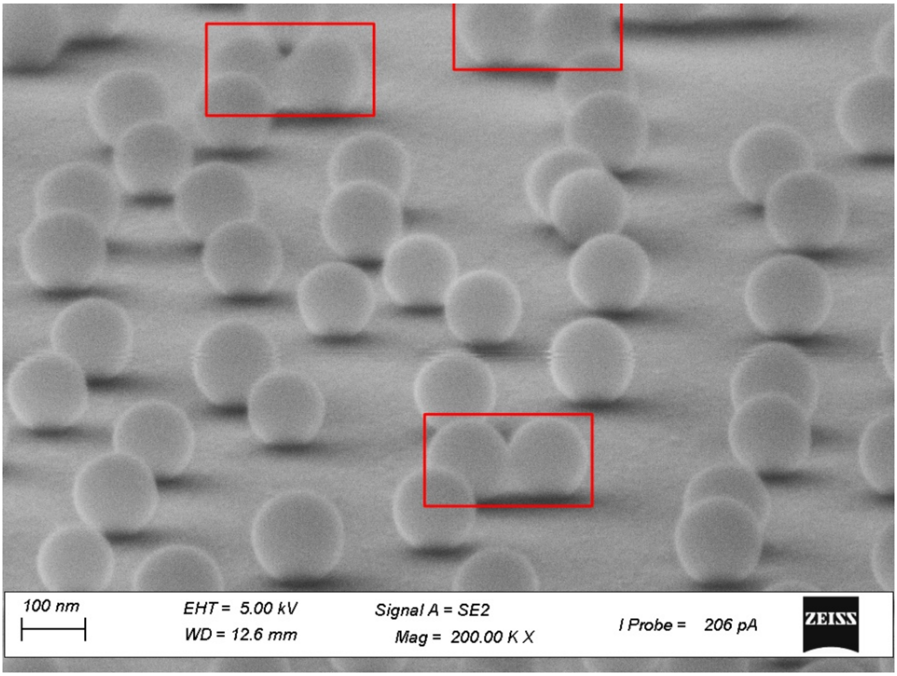

Figure 19: *A side-view SEM image depicting PS beads (140 nm), self-assembled monolayer onto a surface. In some cases, agglomerates can also occur (red boxes) which will be then transferred in the final mask.*

e) *Cr evaporation.* A thin layer of Cr (15 nm) is deposited onto the sample, via e-beam physical vapor deposition (PVD).
f) *Tape stripping.* The nanobeads are removed via tape-stripping, which introduces holes in the areas under the beads, which were not covered by Cr. The shape of the hole is directly connected to the beads cross-section. In other words, spherical beads would yield a circular hole while potential agglomerates (as described in *d)*) would yield irregular shaped holes. In both cases the hole diameter is equivalent to the diameter of the beads used.
g) *O_2 plasma etch.* The sample is exposed to 5 minutes of O_2 plasma treatment (50 W, 250 mTorr, 10 sccm), which will etch the exposed PMMA while leaving the areas covered by Cr intact. Note that 5 minutes is more than enough to completely etch down to the substrate (i.e. ~260 nm PMMA), but also create an undercut, that will be beneficial for the lift-off process (described below).
h) *Hole-mask ready.* The mask is now ready, where the final structure consists of undercut holes that reach down to the substrate.

Once the mask is ready it can now be used to create the nanodisks used throughout this thesis. Using e-beam PVD, we can easily select the desired material to deposit, i.e., Pd, Pt, Au in this thesis. **Figure 20** shows a schematic of the material deposition process through the mask. In the case of only 1 element (**Paper I**, Pt) the material is deposited through the mask (**Figure 20a**) and the mask is lifted off by immersing the sample in acetone that dissolves the PMMA sacrificial layer (**Figure 20c**). This yields a surface covered with nanodisks where their dimensions are determined both by the initial PS beads' size (disk diameter) and the metal deposition rate (disk height).

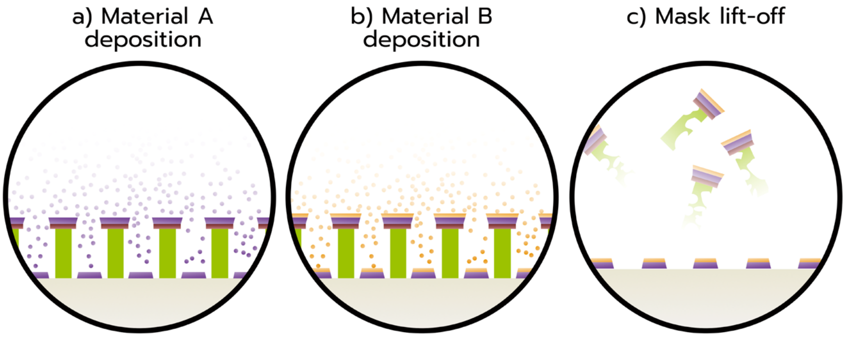

Figure 20: *Schematic illustration of the material deposition process. In the case of only 1 element (e.g. Pt), the material is deposited via e-beam PVD, a), while in the case of multi-element nanodisks (e.g. PdAu) a second deposition occurs, forming a layered structure, b). Finally, the mask is lifted-off in a solvent, leaving a surface with nanodisks, whose diameter depend on the initial PS beads' size, and height determined by the PVD process, c).*

As depicted in the figure, during material deposition the holes gradually shrink, a consequence of material accumulation on the surface of the mask and along the rim of the hole. Therefore, the final structure resembles a truncated cone. In the case of 2 elements (**Paper II & III**, PdAu) Pd is deposited first, followed by an immediate second deposition of Au (**Figure 20b**), thus forming a layered structure. Finally, the mask is lifted-off in the same way as described previously (**Figure 20c**).

Since the purpose of the layered structure is to ultimately form an alloy, the alloy composition (in at.%) can be controlled by i) adjusting the ratio (thicknesses) of the Pd and Au layers, and ii) taking into account the shape of the structures where, as described, are in the form of truncated cones. The composition (number of atoms) can be calculated as,

$$n = \frac{\rho \cdot V}{M} N_A \qquad (5.1)$$

where n is the number of atoms, ρ, V, M are the density,volume and molar mass of the material respectively, and N_A is the Avogadro number[101]. Knowing the number of atoms (i.e., each material's at.% that I want to fabricate) and considering the diameter, total height, and angle α between the cone's slant height and its central axis (where in this fabrication process has been measured to be ~60º [101]), I can calculate the height of each layer. **Figure 21** shows the top and side view of the final result for Pt nanodisks, fabricated using HCL.

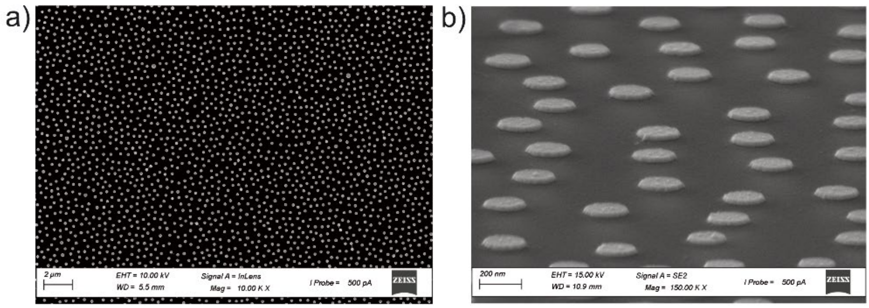

Figure 21: *a) top-view and b) side view of Pt nanodisks fabricated onto a Si substrate using the HCL process. Images taken with an SEM, using the signal from secondary electrons in both cases (see Chapter 6.1 for details).*

In the case of a layered structure like Pd and Au, the process continues with a final thermal annealing process, which increases atomic mobility and induces homogenous alloy formation if it is thermodynamically favorable (described in Chapter 2.2). In **Paper II & III** the PdAu layers were annealed in a reducing atmosphere (2% H_2 in Ar) dealing with oxygen that leaks into the annealing reactor and thus avoiding the formation of an oxide layer. The samples were annealed at 500 ºC for 18 hours, with a gas flow rate of 200 ml/min.

6 H_2 sensing setups & material characterization

In this chapter, I will present the techniques used for characterization as well as H_2 sensing performance experiments, in the appended papers. SEM was used to image the particles and acquire statistics regarding their size distribution (**Paper I, II, III**), energy dispersive X-ray spectroscopy (EDX) was performed on PdAu samples to collect information regarding the alloy composition (**Paper II, III**), and transmission electron microscopy (TEM) imaging was performed on the Pt samples (**Paper I**) to investigate structural changes that occur after exposure to H_2. In **Paper I**, quadruple mass spectrometry (QMS) was employed to investigate the HOR on the Pt surface, while in **Paper II**, QMS was used to identify trace amounts of contaminants present in the supplied gases. Regarding the H_2 sensor performance measurements, the atmospheric pressure flow reactor (X1) was used in **Paper I, III** to investigate the performance of the respective sensors in humid environments. Finally, in **Paper II**, the fast-switch mini reactor (FSM) was used to assess the performance of the sensor and collect the data used in the *LEMAS* model, since it is most suited for kinetics measurements.

6.1 Scanning Electron Microscopy & Energy Dispersive X-Ray Spectroscopy

Scanning electron microscopy (SEM) is a powerful technique used to obtain high resolution images of structures at the micro- and nanoscale. **Figure 22** shows a simplified schematic illustration of the key components of an SEM, alongside an inset showing the *interaction volume*, i.e. the volume at which the electron beam interacts with the sample.

An electron source (gun) emits a beam of high-energy electrons (standard acceleration voltage is 0.1 – 30 kV) which is then focused and directed towards the sample using a series of electromagnetic lenses; the condenser and objective lenses. The purpose of the lenses is to reduce the beam size, (typical beam size from a tungsten-based electron gun is 50 μm) down to a few nanometers (depending on the features of interest), in order to acquire useful images[213]. The focused beam scans the surface of the sample in a raster pattern where the impinging electron beam produces various signals, such as the emission of x-rays, visible photons and electrons.

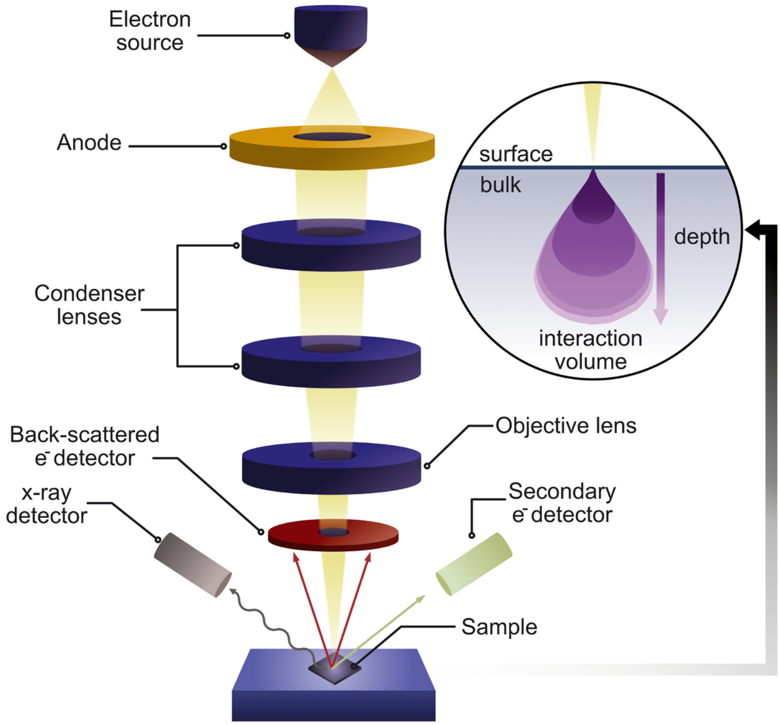

Figure 22: *Simplified illustration of the key components in a scanning electron microscope (SEM). A high energy electron beam travels from the electron source (gun) to the sample, where it is focused via the condenser and objective lenses. Different detectors are used to collect different signals (e.g. x-rays, elastically and inelastically scattered electrons) that derive from the interaction of the beam with the sample. The inset shows the interaction volume, i.e. the volume at which the beam interacts with the sample and causes the emission of different types of the aforementioned signals (adapted from ref.[213]).*

Three main signals are depicted in the schematic via the three different detectors used to collect them. i) The back-scattered electrons (BSE) are high energy electrons that originate from a high depth within the sample (~ 1 μm within the surface). These electrons strongly interact with the material via elastic scattering and are typically used to acquire compositional information by utilizing the optical contrast between different materials with different atomic numbers (Z). ii) Secondary electrons (SE) are ejected from the surface of the sample (~ 100 nm within the surface and correspond to inelastic scattering of loosely bound outer shell electrons of the specimen's surface atoms. These electrons are significantly lower in energy compared to BSE and carry information of the surface structure and topography. iii) When the electron beam interacts with the specimen, *characteristic* X-rays are produced. This is a result of the interaction of the beam with inner shell electrons, which upon impingement of the high energy electron beam, are ejected. The vacancy that is created is immediately filled by an outer-shell electron, which in turn releases energy in the form of an X-ray photon. The emitted X-rays are produced from a volume that extends to ~5 μm deep within the sample, carry energies that are *characteristic* of specific elements and therefore can be used to identify the elemental composition of the sample[213].

These characteristic X-rays are used in energy dispersive X-ray spectroscopy (EDX), which is an analytical technique used for elemental composition characterization of a material. This is done by combining an SEM with a detector that collects the emitted X-rays (SEM/EDX) (**Figure 22**) thus providing a way for both imaging and compositional analysis. In the context of this thesis, SEM using the SE detector was used to image Pt and PdAu nanodisks, while EDX was used to verify the $Pd_{70}Au_{30}$ composition after alloying.

From a practical perspective there are several conditions for acquiring a good image: i) *conductive material.* The sample should be sufficiently conductive to transfer the excessive charge that arrives with the electron beam, to the ground. That is a particular issue when imaging insulating samples, which causes the accumulation of negative charge known as charge buildup. The consequences of this are reduced image quality, irregular contrast, beam shift or image distortion. To avoid this issue, when making a sensor device, I simultaneously fabricated the nanostructures on a fused silica (used for transmission measurements) and Si (used for SEM) substrates. ii) *acceleration voltage*. The acceleration voltage determines how deep the electron beam will 'penetrate' and therefore how broad the interaction volume will be. High acceleration voltage broadens the interaction volume and therefore reduces surface sensitivity (obscuring of fine surface details). In this thesis I have used acceleration voltages that range from 10-15 kV. iii) *working distance.* The working distance is directly connected to the depth of focus where, depending on the imaging conditions, different working distances can be suitable. For example, when imaging at an angle (**Figure 21b**), a larger working distance is more suitable while in the case of imaging at a normal angle (**Figure 21a**), a short working distance can yield higher resolution images. iv) *chamber pressure.* The pressure inside the chamber should be sufficiently low to minimize electron scattering from molecules.

6.2 Transmission Electron Microscopy

When finer features need to be observed (in the context of this thesis the nanodisk surface morphology and grain boundaries), transmission electron microscopy (TEM) is used instead (**Figure 23**), which can provide structural information with atomic resolution. The operating principle of TEM is very similar to SEM with a few key differences, one of which is that the electron beam emitted by a TEM is significantly higher in energy and typically ranges between 60-300 kV. The reason is that, as the name suggests, electrons need to be transmitted through the specimen, where the electrons impinge onto a fluorescent screen, and the image is formed. The energy of the electrons hitting the fluorescent screen is directly connected to the thickness of the specimen, as well as the local mass and electron density, and is therefore translated into a contrast difference in the final image. To allow for the electrons to pass through, TEM requires very thin samples (~50-100 nm) making sample preparation more complex. We have used TEM in **Paper I**, where I have fabricated Pt nanodisks via HCL, onto a thin SiN TEM membrane.

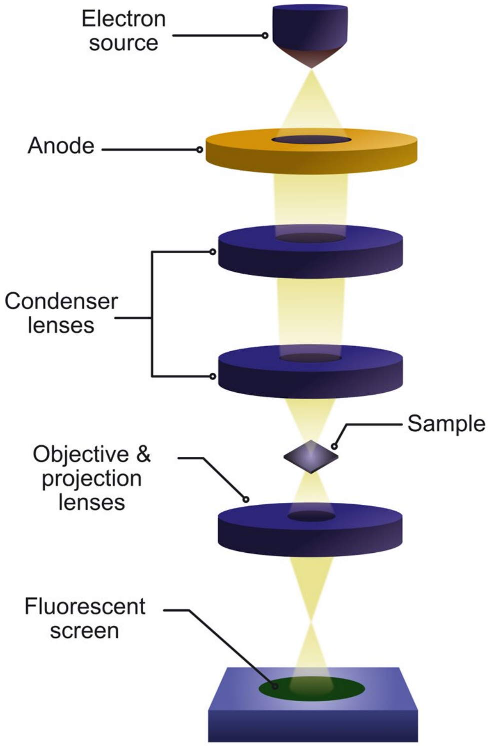

Figure 23: *Simplified illustration of the key components in a transmission electron microscope (TEM). Note that in contrast to an SEM, the sample is placed above a series of lenses (objective and projection), and the high energy electron beam (60 - 300 kV) passes through the sample, before reaching the fluorescent screen where the image is depicted (adapted from ref.*[214]*).*

6.3 Quadruple Mass Spectrometry

Quadruple mass spectrometry (QMS) is a mass analysis technique that is extensively used in catalysis, and specifically to study products from catalytic reactions on surfaces, both qualitatively and quantitatively. The basic operating principle of a QMS is to ionize molecules and separate them based on their mass-to-charge ratio (m/z), which is accomplished by using four parallel cylindrical rods that form a dynamic electric field, where both

DC and RF voltages are applied. This way a selective transmission of ions is possible by controlling the applied voltages. The electric field that is generated will determine which ionized molecules will have a stable trajectory and consequently reach the detector. **Figure 24** shows a simplified illustration of a QMS. Here, neutral, gas-phase molecules desorb from the sample surface and continue towards the detector. First, they pass through an ionization filament which is heated up to a high enough temperature (typically 2000-2500 K for tungsten or rhenium) where it starts emitting free electrons. The electrons are then accelerated via an applied potential and collide with neutral molecules from which they eject an electron and thus form ionized molecules. When the ions enter the quadrupole, they will experience a complex oscillatory motion that is determined by the combined DC and RF fields. Their trajectory is then determined by the ion mass, where heavier ions are less affected by high-frequency oscillations, and their charge, where higher charge leads to stronger field interactions[215].

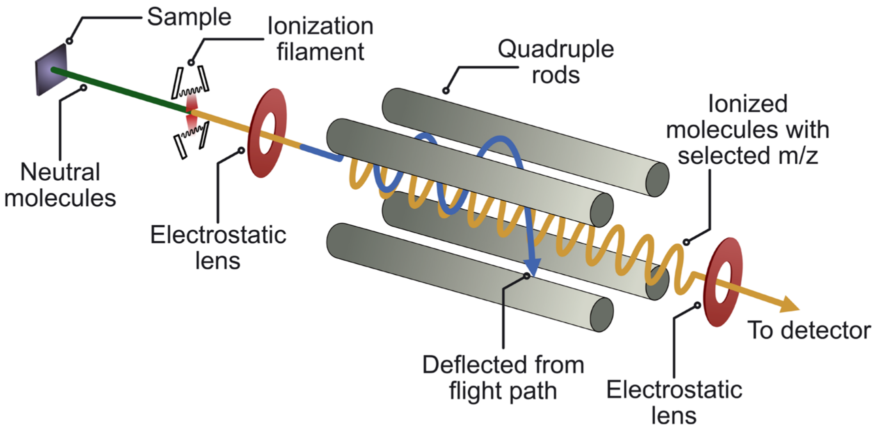

Figure 24: *Simplified illustration of the quadruple mass spectrometry (QMS) principle. Neutral gas-phase molecules pass through a filament that causes ionization. The ions pass through electrostatic lenses and slits (not shown), that aim at focusing and restricting the ion beam. Ions with a stable trajectory will reach the detector while others will be deflected from the flight path. A stable trajectory is determined by the applied DC and RF fields, and the ion mass and ion charge (adapted from refs[215,216].)*

The QMS (here we used the OmniStar GSD320, Pfeiffer Vacuum GmbH) can be operated in a scanning mode, where the instrument scans different voltages in a stepwise manner and therefore collects all ions that have a stable trajectory for a given voltage, forming a mass spectrum. This is useful for determining molecules present on the surface or in the gas stream (particularly in the context of this thesis), as we did for **Paper II**. Additionally, the QMS can be operated in *selected ion monitoring* (SIM) mode, where it monitors only specific pre-selected m/z values. In **Paper I** we have used SIM to monitor the signal from H_2O produced via the HOR and desorbed in the gas phase.

6.4 Humidified flow reactor

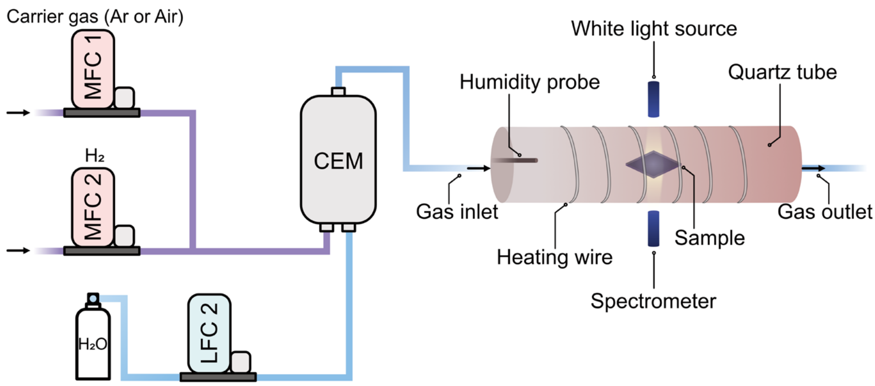

Figure 25: *Schematic illustration of the humidified flow (X1) reactor setup. The humidified gas mixture and flow rate are controlled by a series of mass (or liquid) flow controllers (M(L)FCs) and are mixed in a controlled evaporator mixer (CEM), forming humidified gas. The sample is positioned inside a heated quartz tube with two optically transparent viewports allowing for transmission measurements. The humidity is measured using a humidity probe positioned close to the gas inlet.*

The humidified flow (X1) reactor (Insplorion AB) can accommodate hydrogenation experiments in humid environments, and has been used extensively in this thesis, specifically in **Paper I & III**. In both papers it was used to perform sensor performance measurements and the long-term stability investigation, while in **Paper I** we used it for humidity titration measurements. The setup consists of a quartz tube (effective volume ≈190 mL) with optical access for transmittance measurements (**Figure 25**). It is equipped with mass flow controllers (MFCs, Bronkhorst High-Tech B.V.) that control the flow rate and gas composition. A liquid flow controller (LFC, Bronkhorst High-Tech B.V.) is also incorporated to control the flow rate of H_2O. Gases and H_2O are introduced into a controlled evaporator mixer (CEM, Bronkhorst High-Tech B.V.) where they mix forming humidified gas. In all measurements the water supplied from the LFC (into the CEM for humidifying the gas) is referenced to RH values at 30 ºC, 1.013 bar, 200 ml/min total gas flow rate. (see **Paper I & III,** *Methods* for more details). The humidity level was measured by a calibrated humidity and temperature probe (HMP7, Vaisala) positioned at the chamber inlet. The reactor temperature was controlled using a closed-loop temperature control system (Eurotherm 3216) in a feedback loop manner, where the sample surface temperature inside the chamber (measured via a K-type thermocouple) was continuously used as the input. The chamber can accommodate up to two samples, which are illuminated using an unpolarized halogen white light source (AvaLight-HAL, Avantes) coupled through a bifurcated optical fiber (FCB-UV600-2, Avantes BV) equipped with collimated lenses. The transmitted light from each sample is collected and analyzed by a dual channel fiber-coupled fixed-grating spectrometer (AvaSpec-ULS2048CL-2-EVO, Avantes BV).

6.5 Fast-switch mini reactor

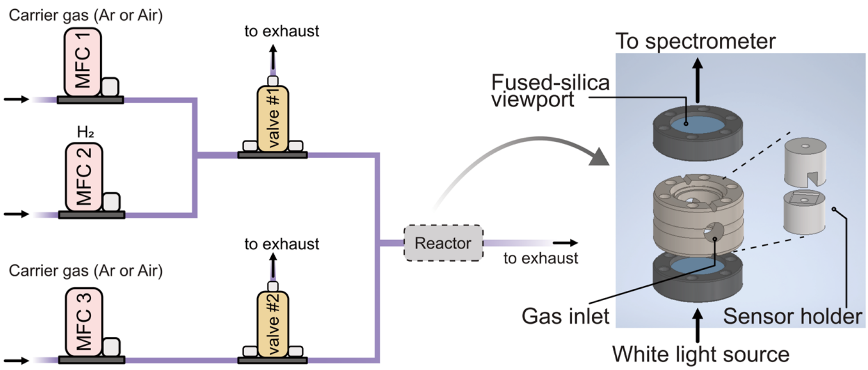

Figure 26: *Schematic illustration of the fast-switch mini (FSM) reactor. Similar to X1, the gases are controlled via MFCs and are then introduced into the reactor directly or via two 3-way valves (optional). The purpose of the 3-way valves is to negate the inherent delay associated with MFCs and pre-mix the desired H_2 gas concentration. The sample is placed inside a small (1.5 mL) custom-built reactor, with two optically transparent viewports allowing for transmission measurements (adapted from ref.[80]).*

The fast-switch mini (FSM) reactor is a custom built setup designed to perform kinetics experiments, i.e. to temporally resolve the interactions of our sensors with hydrogen (**Figure 26**). Unlike X1, the volume of this chamber is significantly smaller (1.5 mL) allowing for faster exchange of gases. This is important when investigating sensors with ultra-fast response time, where the limitation is usually not the intrinsic response time but the experimental setup, i.e. sensors placed in large reactors, yield slower response, due to the gas exchange constant. As an example, the gas exchange constant can be calculated as,

$$\tau = \frac{V}{q} \tag{6.1}$$

where V is the volume of the reactor (here 1.5 mL) and q is the gas flow rate (typical is 300 ml/min or 5 ml/s). Adding these values yields a gas exchange constant of 300 ms. To further push the exchange constant to lower values, a higher flow rate can be selected (possible up to 2000 ml/min in FSM). Additionally, since MFCs inherently have a delay of ~ 2 seconds (from when they receive a signal), they can cause ambiguity during analysis of the response time. For this reason, we have introduced two additional 3-way valves as an option. These valves aim at premixing the desired gas concentration, before introducing the premixed gas into the reactor when needed. This is accomplished by operating them in an alternating manner (switching); when one is supplying gas into the reactor, the other is directing the gas to the exhaust. The FSM reactor has been used in **Paper II**, to perform hydrogenation measurements on a PdAu sensor, where we used the spectral data to further push the response time via the *LEMAS* model. In this case, the 3-way valves were not used due to technical issues associated with them at the time, which however did not pose an issue, since the inherent response time was higher than the gas exchange constant (including MFCs delay) for the measured H_2 concentration range.

Moving to the technical specification, the custom-built reactor is composed of a customized DN 16 CF spacer flange (Pfeiffer Vacuum GmbH), equipped with a gas in- and outlet, and two fused-silica viewports (1.33 in. CF Flage, Accu-Glass) The sample inside the chamber is illuminated via an unpolarized halogen white light source (AvaLight-HAL, Avantes BV) and an optical fiber equipped with a collimating lens. The transmitted light is collected and analyzed by using a fiber-coupled fixed-grating spectrometer (SensLine AvaSpec-HS1024TEC, Avantes BV). The temperature is controlled with a heating coil wrapped around the chamber and a temperature controller (Eurotherm 3216) in a feedback loop manner, where the sample surface temperature inside the chamber is continuously used as the input.

7 Conclusions & outlook

One of the main goals of this thesis was to shed light onto, and attempt to address, the humidity challenge introduced in Chapter 1. Taking advantage of our knowledge and expertise in nanoplasmonic optical sensing, and inspired by other work[37], we demonstrate in **Paper I** a Pt-based H_2 sensor that can operate in a wide RH range of 0-80% and that can detect H_2 concentrations as low as 600 ppm in air, at T≥ 50 ºC. Furthermore, our findings reveal that the LoD *improves* with increasing humidity, a unique feature that, to the best of our knowledge, has not been reported in previous studies, where the presence of humidity across the board lowers the LoD of H_2 sensors, as well as decelerates them. Finally, it is important to emphasize that the sensor most likely can operate effectively at RH levels higher that 80%, since I was limited to this upper limit by the experimental setup used.

As a retrospective, it is evident that the main driving force behind the accelerating progress in H_2 sensing has been primarily the growing ability to design complex nanoarchitectures and deepen our understanding of nanoscale phenomena. However, to further push the performance of H_2 sensors, materials engineering is not expected to be the sole solution and may not carry us all the way. Hence, as a complement, building on the rapid advancements in machine learning and artificial intelligence, it is crucial to also consider implementing these techniques. Such methods can greatly enhance the treatment of sensor output data (particularly in nanoplasmonic sensors, by utilizing the entire spectral response and not just a single descriptor), thereby dramatically improving sensor performance, and potentially mitigating the influence of undesirable factors. For this reason, part of my thesis has been focused on collaborating with experts in this field, in order to push the performance of the existing, state-of-the-art nanoplasmonic H_2 sensors in two distinct different ways:

In **Paper II** we demonstrate the use of a tailored *Long short-term transformer Ensemble Model for Accelerated Sensing* (LEMAS) and showcase the acceleration of a PdAu alloy nanoplasmonic sensor by a factor of 40 (compared to the standard data treatment) and eliminate the dependance of the response time on H_2 concentration. This is realized by predicting the thermodynamic sensor saturation level to a specific H_2 concentration before that is physically reached by the hardware.

In **Paper III** we employ a Deep Dense Neural Network (DDNN) and Transformer model to process data from a PdAu nanoplasmonic sensor operating under varying relative humidity levels (0-80% RH). This treatment effectively eliminates the negative influence of H_2O in the sensor's response, enabling robust and reproducible sensor performance with a limit of detection of 100 ppm even at the highest measured RH.

Reflecting back to the time I've spent as a doctoral candidate, and in the context of the work presented here, I am very happy with what we have achieved so far, and I am very excited for what is yet to come. Of course, the road was not always paved with gold and many technical issues concerning our experimental setups have delayed parts of my projects. Therefore, I wish that I would have acquainted myself with the "nitty-gritty" of the experimental setups (that I use primarily) much earlier in the PhD so I would be able to tackle any issues in due time.

Looking forward to the remaining of my PhD journey, I believe that further implementation of advanced AI-based methods in data analysis, combined with materials engineering may indeed be the key for addressing the important challenges present in the H_2 sensing community. Since a single material sensor device is not expected to be capable of meeting all of the performance targets, we have initiated efforts into bi- or multiplexing of different materials in a single sensing platform, capable of handling highly complex environments (including H_2O, NOx, CO, CO2), where the use of AI-based data analysis can bring us closer to a "master" H_2 sensor, capable of high-performance operation under most environmental conditions.

Going also back to the fundamentals, the search for new materials that can challenge the current state-of-the-art H_2 sensors, is something I am very interested in pursuing. Combining that with more advanced nanofabrication techniques, such as electron beam lithography, we can take advantage of unique plasmonic properties (e.g. field enhancement via a plasmonic metasurface) and *possibly* push metrics such as the limit of detection, to the low part-per-billion (ppb) regime.

Acknowledgments

First and foremost, I would like to acknowledge the excellent working environment that has been fostered in the Chemical Physics division, and thank all the people working here for making this a great place to work in. I really enjoy our scientific discussions during our bi-weekly division meetings, and the entertaining social discussions during fika.

I would also like to thank all the members of the Langhammer group (past and present), where, through collaboration and discussion, allowed my work to flourish. Many thanks specifically to my main supervisor, Prof. Christoph Langhammer, for always giving me timely feedback, confidence boost and new ideas during our discussions. Big thanks also to Dr. Joachim Fritzsche (co-supervisor) who, through his nanofabrication expertise, has further strengthened my cleanroom-related skills and knowledge and, in many cases, has assisted me greatly in pursuing new fabrication ideas.

Additionally, I would like to thank all my collaborators in the work presented in this thesis, for the many interesting and insightful discussions.

Also, my colleague, Carl Andersson with whom I've spent many hours discussing not only on H_2-related topics, but on many of our common personal interests.

I want to acknowledge also Dr. David Tomeček, with whom I overlapped for the first 4 months of my PhD, and who introduced me "practically" into the world of nanoplasmonic H_2 sensing. Even to this day he is always eager to answer my questions and help in any way possible.

I would also like to thank all my friends, both here in Sweden and in Greece, for supporting me along this journey and for the great times we've had. Also, my two families back home (Theo, Fanny, Kostas, Klara and Freddy) for their continuous support.

Special shoutout to my life partner, Eleni, who has been with me in this journey all along and supporting me from the sideline. She has been the unsung hero and the invisible force during all this time.

Finally I would like to acknowledge the funding provided by the Swedish Energy Agency, the Swedish Foundation for Strategic Research and the TechForH_2 competence center.

References

(1) Haldane, J. B. S. Daedalus or Science and the Future: a paper read to the Heretics, Cambridge on February 4th, 1923. (**1923**). https://archive.org/details/daedalus_or_science_and_the_future

(2) Bockris, J. O. M. A hydrogen economy. *Science* 176, 1323 (**1972**). https://doi.org/10.1126/science.176.4041.1323

(3) Gregory, D. P., Ng, D.Y.C., Long, G.M. in *Electrochemistry of Cleaner Environments* 226--280 (Springer US, **1972**).https://doi.org/10.1007/978-1-4684-1950-4_8

(4) Yap, J. & McLellan, B. A Historical Analysis of Hydrogen Economy Research, Development, and Expectations, 1972 to 2020. *Environments* 10 (**2023**). https://doi.org/10.3390/environments10010011

(5) Lower and Upper Explosive Limits for Flammable Gases and Vapors (LEL/UEL). https://www.chrysalisscientific.com/pg443-Lower-LEL-Upper-UEL-Explosive-Limits.pdf

(6) Accidentology involving hydrogen. (Ministry of ecology, energy, sustainable development and town and country planning, *Bureau for analysis of industrial risks and pollution,* France, **2009**). <https://www.aria.developpement-durable.gouv.fr/wp-content/files_mf/SY_hydrogen_GB_2009.pdf>

(7) van Ruijven, B., Lamarque, J.-F., van Vuuren, D. P., Kram, T. & Eerens, H. Emission scenarios for a global hydrogen economy and the consequences for global air pollution. *Global Environmental Change* 21, 983-994 (**2011**). https://doi.org/https://doi.org/10.1016/j.gloenvcha.2011.03.013

(8) Tromp, T. K., Shia, R.-L., Allen, M., Eiler, J. M. & Yung, Y. L. Potential Environmental Impact of a Hydrogen Economy on the Stratosphere. *Science* 300, 1740-1742 (**2003**). https://doi.org/doi:10.1126/science.1085169

(9) Schultz, M. G., Diehl, T., Brasseur, G. P. & Zittel, W. Air Pollution and Climate-Forcing Impacts of a Global Hydrogen Economy. *Science* 302, 624-627 (**2003**). https://doi.org/doi:10.1126/science.1089527

(10) Derwent, R. G., Stevenson, D. S., Utembe, S. R., Jenkin, M. E., Khan, A. H. & Shallcross, D. E. Global modelling studies of hydrogen and its isotopomers using STOCHEM-CRI: Likely radiative forcing consequences of a future hydrogen economy. *International Journal of*

Hydrogen Energy 45, 9211-9221 (**2020**). https://doi.org/10.1016/j.ijhydene.2020.01.125

(11) Ocko, I. B. & Hamburg, S. P. Climate consequences of hydrogen emissions. *Atmos. Chem. Phys.* 22, 9349-9368 (**2022**). https://doi.org/10.5194/acp-22-9349-2022

(12) Paul M. Ordin, C. A. V., William J. Brown. *Guidelines for Hydrogen Selection, Operations, System Design, Materials Storage, and Transportation* (National Aeronautics and Space Administration, Washington, DC, **1997**), https://ntrs.nasa.gov/api/citations/19970033338/downloads/19970033338.pdf

(13) Hübert, T., Boon-Brett, L., Black, G. & Banach, U. Hydrogen sensors – A review. *Sensors and Actuators B: Chemical* 157, 329-352 (**2011**). https://doi.org/10.1016/j.snb.2011.04.070

(14) Chauhan, P. S. & Bhattacharya, S. Hydrogen gas sensing methods, materials, and approach to achieve parts per billion level detection: A review. *International Journal of Hydrogen Energy* 44, 26076-26099 (**2019**). https://doi.org/10.1016/j.ijhydene.2019.08.052

(15) Berndt, D., Muggli, J., Wittwer, F., Langer, C., Heinrich, S., Knittel, T. & Schreiner, R. MEMS-based thermal conductivity sensor for hydrogen gas detection in automotive applications. *Sensors and Actuators, A: Physical* 305, 111670-111670 (**2020**). https://doi.org/10.1016/j.sna.2019.111670

(16) Emperhoff, S., Eberl, M., Dwertmann, T. & Wöllenstein, J. On the Influence of Humidity on a Thermal Conductivity Sensor for the Detection of Hydrogen. *Sensors* 24, 2697 (**2024**). https://doi.org/10.3390/s24092697

(17) Wu, Z., Zhang, X., Chen, L., Lou, Q., Zong, D., Deng, K., Cheng, Z. & Xia, M. Ultra-Low-Power, Extremely Stable, Highly Linear-Response Thermal Conductivity Sensor Based on a Suspended Device with Single Bare Pt Nanowire. *ACS Sensors* 9, 4721-4730 (**2024**). https://doi.org/10.1021/acssensors.4c01111

(18) Wang, C., Jiao, B., Liu, X., Zhao, C., Wu, G. & Liu, R. in *2023 IEEE 16th International Conference on Electronic Measurement & Instruments (ICEMI)* 204-208 (**2023**).https://doi.org/10.1109/icemi59194.2023.10270148

(19) Harumoto, T., Fujiki, H., Shi, J. & Nakamura, Y. Extremely simple structure hydrogen gas sensor based on single metallic thin-wire under

sweep heating. *International Journal of Hydrogen Energy* 47, 34291-34298 (**2022**). https://doi.org/10.1016/j.ijhydene.2022.08.001

(20) Simon, I. & Arndt, M. Thermal and gas-sensing properties of a micromachined thermal conductivity sensor for the detection of hydrogen in automotive applications. *Sensors and Actuators A: Physical* 97-98, 104-108 (**2002**). https://doi.org/10.1016/S0924-4247(01)00825-1

(21) Tardy, P., Coulon, J.-R., Lucat, C. & Menil, F. Dynamic thermal conductivity sensor for gas detection. *Sensors and Actuators B: Chemical* 98, 63-68 (**2004**). https://doi.org/10.1016/j.snb.2003.09.019

(22) Korotcenkov, G., Han, S. D. & Stetter, J. R. Review of Electrochemical Hydrogen Sensors. *Chemical Reviews* 109, 1402-1433 (**2009**). https://doi.org/10.1021/cr800339k

(23) Yi, J., Zhang, H., Zhang, Z. & Chen, D. Hierarchical porous hollow SnO2 nanofiber sensing electrode for high performance potentiometric H2 sensor. *Sensors and Actuators B: Chemical* 268, 456-464 (**2018**). https://doi.org/10.1016/j.snb.2018.04.086

(24) Yang, F., Donavan, K. C., Kung, S. C. & Penner, R. M. The surface scattering-based detection of hydrogen in air using a platinum nanowire. *Nano Letters* 12, 2924-2930 (**2012**). https://doi.org/10.1021/nl300602m

(25) Yoo, H.-W., Cho, S.-Y., Jeon, H.-J. & Jung, H.-T. Well-Defined and High Resolution Pt Nanowire Arrays for a High Performance Hydrogen Sensor by a Surface Scattering Phenomenon. *Analytical Chemistry* 87, 1480-1484 (**2015**). https://doi.org/10.1021/ac504367w

(26) Gu, H., Wang, Z. & Hu, Y. Hydrogen gas sensors based on semiconductor oxide nanostructures. *Sensors (Basel)* 12, 5517-5550 (**2012**). https://doi.org/10.3390/s120505517

(27) Zhang, Z., Zou, X., Xu, L., Liao, L., Liu, W., Ho, J., Xiao, X., Jiang, C. & Li, J. Hydrogen gas sensor based on metal oxide nanoparticles decorated graphene transistor. *Nanoscale* 7, 10078-10084 (**2015**). https://doi.org/10.1039/c5nr01924a

(28) Kim, S. M., Kim, H. J., Jung, H. J., Park, J. Y., Seok, T. J., Choa, Y. H., Park, T. J. & Lee, S. W. High-Performance, Transparent Thin Film Hydrogen Gas Sensor Using 2D Electron Gas at Interface of Oxide Thin Film Heterostructure Grown by Atomic Layer Deposition. *Advanced Functional Materials* 29 (**2018**). https://doi.org/10.1002/adfm.201807760

(29) Mirzaei, A., Yousefi, H. R., Falsafi, F., Bonyani, M., Lee, J.-H., Kim, J.-H., Kim, H. W. & Kim, S. S. An overview on how Pd on resistive-

based nanomaterial gas sensors can enhance response toward hydrogen gas. *International Journal of Hydrogen Energy* 44, 20552-20571 (**2019**). https://doi.org/10.1016/j.ijhydene.2019.05.180

(30) Yang, F., Taggart, D. K. & Penner, R. M. Fast, Sensitive Hydrogen Gas Detection Using Single Palladium Nanowires That Resist Fracture. *Nano Letters* 9, 2177-2182 (**2009**). https://doi.org/10.1021/nl9008474

(31) Lee, J. S., Kim, S. G., Cho, S. & Jang, J. Porous palladium coated conducting polymer nanoparticles for ultrasensitive hydrogen sensors. *Nanoscale* 7, 20665-20673 (**2015**). https://doi.org/10.1039/c5nr06193h

(32) Tsuji, T., Mihara, R., Saito, T., Hagihara, S., Oizumi, T., Takeda, N., Ohgi, T., Yanagisawa, T., Akao, S., Nakaso, N. & Yamanaka, K. Highly Sensitive Ball Surface Acoustic Wave Hydrogen Sensor with Porous Pd-Alloy Film. *Materials Transactions* 55, 1040-1044 (**2014**). https://doi.org/10.2320/matertrans.I-M2014816

(33) Anderson, T. J., Wang, H. T., Kang, B. S., Ren, F., Pearton, S. J., Osinsky, A., Dabiran, A. & Chow, P. P. Effect of bias voltage polarity on hydrogen sensing with AlGaN/GaN Schottky diodes. *Applied Surface Science* 255, 2524-2526 (**2008**). https://doi.org/10.1016/j.apsusc.2008.07.173

(34) Chase, M. W. NIST-JANAF Thermochemical Tables 4th ed. *J. of Physical and Chemical Reffernce Data*, 1529-1564 (**1998**).

(35) Lee, E.-B., Hwang, I.-S., Cha, J.-H., Lee, H.-J., Lee, W.-B., Pak, J. J., Lee, J.-H. & Ju, B.-K. Micromachined catalytic combustible hydrogen gas sensor. *Sensors and Actuators B: Chemical* 153, 392-397 (**2011**). https://doi.org/10.1016/j.snb.2010.11.004

(36) Nishibori, M., Shin, W., Izu, N., Itoh, T., Matsubara, I., Watanabe, N. & Kasuga, T. Thermoelectric hydrogen sensors using Si and SiGe thin films with a catalytic combustor. *Journal of the Ceramic Society of Japan* 118, 188-192 (**2010**). https://doi.org/10.2109/jcersj2.118.188

(37) Geng, X., Li, S., Heo, J., Peng, Y., Hu, W., Liu, Y., Huang, J., Ren, Y., Li, D., Zhang, L. & Luo, L. Grain-Boundary-Rich Noble Metal Nanoparticle Assemblies: Synthesis, Characterization, and Reactivity. *Advanced Functional Materials* 32 (**2022**). https://doi.org/10.1002/adfm.202204169

(38) Harley-Trochimczyk, A., Chang, J., Zhou, Q., Dong, J., Pham, T., Worsley, M. A., Maboudian, R., Zettl, A. & Mickelson, W. Catalytic hydrogen sensing using microheated platinum nanoparticle-loaded

graphene aerogel. *Sensors and Actuators, B: Chemical* 206, 399-406 (**2015**). https://doi.org/10.1016/j.snb.2014.09.057

(39) F.D. Manchester, A. S.-M., and J.M. Pitre. The H-Pd (Hydrogen-Palladium) System. *Journal of Phase Equilibria and Diffusion* 15 (**1994**). https://doi.org/10.1007/BF02667685

(40) Radeva, T., Ngene, P., Slaman, M., Westerwaal, R., Schreuders, H. & Dam, B. Highly sensitive and selective visual hydrogen detectors based on YxMg1−x thin films. *Sensors and Actuators B: Chemical* 203, 745-751 (**2014**). https://doi.org/10.1016/j.snb.2014.06.134

(41) Bannenberg, L., Schreuders, H. & Dam, B. Tantalum-Palladium: Hysteresis-Free Optical Hydrogen Sensor Over 7 Orders of Magnitude in Pressure with Sub-Second Response. *Advanced Functional Materials* 2010483, 1-9 (**2021**). https://doi.org/10.1002/adfm.202010483

(42) Boelsma, C., Bannenberg, L. J., van Setten, M. J., Steinke, N. J., van Well, A. A. & Dam, B. Hafnium-an optical hydrogen sensor spanning six orders in pressure. *Nat Commun* 8, 15718 (**2017**). https://doi.org/10.1038/ncomms15718

(43) Bannenberg, L. J., Boelsma, C., Schreuders, H., Francke, S., Steinke, N. J., van Well, A. A. & Dam, B. Optical hydrogen sensing beyond palladium: Hafnium and tantalum as effective sensing materials. *Sensors and Actuators B: Chemical* 283, 538-548 (**2019**). https://doi.org/10.1016/j.snb.2018.12.029

(44) Nugroho, F. A. A., Darmadi, I., Cusinato, L., Susarrey-Arce, A., Schreuders, H., Bannenberg, L. J., da Silva Fanta, A. B., Kadkhodazadeh, S., Wagner, J. B., Antosiewicz, T. J., Hellman, A., Zhdanov, V. P., Dam, B. & Langhammer, C. Metal–polymer hybrid nanomaterials for plasmonic ultrafast hydrogen detection. *Nature Materials* 18, 489-495 (**2019**). https://doi.org/10.1038/s41563-019-0325-4

(45) Anggoro Ardy Nugroho, F., Bai, P., Darmadi, I., Castellanos, G. W., Fritzsche, J., Langhammer, C., Gómez Rivas, J. & Baldi, A. Inverse designed plasmonic metasurface with parts per billion optical hydrogen detection. (**2022**). https://doi.org/10.1038/s41467-022-33466-8

(46) Darmadi, I., Anggoro Ardy Nugroho, F., Kadkhodazadeh, S., B. Wagner, J. & Langhammer, C. Rationally Designed PdAuCu Ternary Alloy Nanoparticles for Intrinsically Deactivation-Resistant Ultrafast Plasmonic Hydrogen Sensing. *ACS Sensors* 4, 1424-1432 (**2019**). https://doi.org/10.1021/acssensors.9b00610

(47) Darmadi, I., Khairunnisa, S. Z., Tomeček, D. & Langhammer, C. Optimization of the Composition of PdAuCu Ternary Alloy Nanoparticles for Plasmonic Hydrogen Sensing. *ACS Applied Nano Materials* 4, 8716-8722 (**2021**). https://doi.org/10.1021/acsanm.1c01242

(48) Darmadi, I., Stolaś, A., Östergren, I., Berke, B., Nugroho, F. A. A., Minelli, M., Lerch, S., Tanyeli, I., Lund, A. & Andersson, O. Bulk-processed Pd nanocube–poly (methyl methacrylate) nanocomposites as plasmonic plastics for hydrogen sensing. *ACS Applied Nano Materials* 3, 8438-8445 (**2020**). https://doi.org/10.1021/acsanm.0c01907

(49) Ostergren, I., Pourrahimi, A. M., Darmadi, I., da Silva, R., Stolas, A., Lerch, S., Berke, B., Guizar-Sicairos, M., Liebi, M., Foli, G., Palermo, V., Minelli, M., Moth-Poulsen, K., Langhammer, C. & Muller, C. Highly Permeable Fluorinated Polymer Nanocomposites for Plasmonic Hydrogen Sensing. *ACS Appl Mater Interfaces* 13, 21724-21732 (**2021**). https://doi.org/10.1021/acsami.1c01968

(50) Östergren, I., Darmadi, I., Lerch, S., da Silva, R. R., Craighero, M., Paleti, S. H. K., Moth-Poulsen, K., Langhammer, C. & Müller, C. A surface passivated fluorinated polymer nanocomposite for carbon monoxide resistant plasmonic hydrogen sensing. *Journal of Materials Chemistry A* 12, 7906-7915 (**2024**). https://doi.org/10.1039/D4TA00055B

(51) W. Buttner, R. B., M. Post, and C. Rivkin. Summary and Findings from the NREL/DOE Hydrogen Sensor Workshop. *National Renewable Energy Laboratory* (**2011**). https://www.nrel.gov/docs/fy12osti/55645.pdf

(52) Boon-Brett, L., Bousek, J., Black, G., Moretto, P., Castello, P., Hübert, T. & Banach, U. Identifying performance gaps in hydrogen safety sensor technology for automotive and stationary applications. *International Journal of Hydrogen Energy* 35, 373-384 (**2010**). https://doi.org/10.1016/j.ijhydene.2009.10.064

(53) Energy, U. S. D. o. The Hydrogen and Fuel Cell Technologies Office Multi-Year Research, Development, and Demonstration. *Hydrogen and Fuel Cell Technologies Office*, 1-28 (**2015**). https://www.energy.gov/sites/default/files/2015/06/f23/fcto_myrdd_safety_codes.pdf

(54) Darmadi, I., Nugroho, F. A. A. & Langhammer, C. High-Performance Nanostructured Palladium-Based Hydrogen Sensors - Current Limitations and Strategies for Their Mitigation. *ACS Sensors* 5, 3306-3327 (**2020**). https://doi.org/10.1021/acssensors.0c02019

(55) Lee, J., Noh, J.-S., Lee, S. H., Song, B., Jung, H., Kim, W. & Lee, W. Cracked palladium films on an elastomeric substrate for use as

hydrogen sensors. *International Journal of Hydrogen Energy* 37, 7934-7939 (**2012**). https://doi.org/https://doi.org/10.1016/j.ijhydene.2012.01.067

(56) Sirbuly, D. J., Létant, S. E. & Ratto, T. V. Hydrogen Sensing with Subwavelength Optical Waveguides via Porous Silsesquioxane-Palladium Nanocomposites. *Advanced Materials* 20, 4724-4727 (**2008**). https://doi.org/10.1002/adma.200800890

(57) Behzadi Pour, G., Fekri Aval, L. & Esmaili, P. Performance of gas nanosensor in 1-4 per cent hydrogen concentration. *Sensor Review* 39, 622-628 (**2019**). https://doi.org/10.1108/sr-06-2018-0155

(58) Luong, H. M., Pham, M. T., Guin, T., Madhogaria, R. P., Phan, M. H., Larsen, G. K. & Nguyen, T. D. Sub-second and ppm-level optical sensing of hydrogen using templated control of nano-hydride geometry and composition. *Nat Commun* 12, 2414 (**2021**). https://doi.org/10.1038/s41467-021-22697-w

(59) Meng, X., Bi, M. & Gao, W. PdAg alloy modified SnO2 nanoparticles for ultrafast detection of hydrogen. *Sensors and Actuators B: Chemical* 382, 133515 (**2023**). https://doi.org/10.1016/j.snb.2023.133515

(60) Jo, M. S., Kim, K. H., Lee, J. S., Kim, S. H., Yoo, J. Y., Choi, K. W., Kim, B. J., Kwon, D. S., Yoo, I., Yang, J. S., Chung, M. K., Park, S. Y., Seo, M. H. & Yoon, J. B. Ultrafast (approximately 0.6 s), Robust, and Highly Linear Hydrogen Detection up to 10% Using Fully Suspended Pure Pd Nanowire. *ACS Nano* 17, 23649-23658 (**2023**). https://doi.org/10.1021/acsnano.3c06806

(61) Xing, Q., Cai, Y. & Zhang, M. A sub-second response/recovery hydrogen sensor based on multifunctional palladium oxide modified heterojunctions. *Sensors and Actuators B: Chemical* 401 (**2024**). https://doi.org/10.1016/j.snb.2023.134956

(62) Standardization, I. O. f. Hydrogen detection apparatus — Stationary applications (ISO Standard No. 26142:2010). (**2010**). https://www.iso.org/standard/52319.html

(63) Gaman, V. I., Maksimova, N. K., Almaev, A. V. & Sergeychenko, N. V. Effect of Humidity on Characteristics of Hydrogen Sensors Based on Nanocrystalline SnO2 Thin Films with Various Catalysts. *Key Engineering Materials* 683, 353 - 357 (**2016**). https://doi.org/10.4028/www.scientific.net/KEM.683.353

(64) Zhao, Z., Knight, M., Kumar, S., Eisenbraun, E. T. & Carpenter, M. A. Humidity effects on Pd/Au-based all-optical hydrogen sensors.

Sensors and Actuators B: Chemical 129, 726-733 (**2008**). https://doi.org/10.1016/j.snb.2007.09.032

(65) Sanger, A., Kumar, A., Chauhan, S., Gautam, Y. K. & Chandra, R. Fast and reversible hydrogen sensing properties of Pd/Mg thin film modified by hydrophobic porous silicon substrate. *Sensors and Actuators B: Chemical* 213, 252-260 (**2015**). https://doi.org/10.1016/J.SNB.2015.02.098

(66) Yaqoob, U., Uddin, A. S. M. I. & Chung, G. S. Foldable hydrogen sensor using Pd nanocubes dispersed into multiwall carbon nanotubes-reduced graphene oxide network assembled on nylon filter membrane. *Sensors and Actuators B: Chemical* 229, 355-361 (**2016**). https://doi.org/10.1016/J.SNB.2016.01.138

(67) Sanger, A., Kumar, A., Kumar, A., Jaiswal, J. & Chandra, R. A fast response/recovery of hydrophobic Pd/V2O5 thin films for hydrogen gas sensing. *Sensors and Actuators B: Chemical* 236, 16-26 (**2016**). https://doi.org/10.1016/J.SNB.2016.05.141

(68) Rahamim, G., Mirilashvili, M., Nanikashvili, P., Greenberg, E., Shpaisman, H., Grinstein, D., Welner, S. & Zitoun, D. Hydrogen sensors with high humidity tolerance based on indium-tin oxide colloids. *Sensors and Actuators, B: Chemical* 310, 127845-127845 (**2020**). https://doi.org/10.1016/j.snb.2020.127845

(69) Murthy, A. S. R., Gnanasekar, K. I. & Jayaraman, V. Hydrogen sensing behavior of SnO2and in2O3thin films in wide range of humid conditions-An exploratory data analysis. *Journal of Environmental Chemical Engineering* 8, 104158-104158 (**2020**). https://doi.org/10.1016/j.jece.2020.104158

(70) Manchester, A. S. M. a. F. D. The H-Ta (Hydrogen-Tantalum) System. *Journal of Phase Equilibria and Diffusion* 12 (**1991**). https://doi.org/10.1007/BF02649922

(71) Manchester, A. S.-M. a. F. D. The H-Ti (Hydrogen-Titanium) System. *Bulletin of Alloy Phase Diagrams* 8 (**1987**). https://doi.org/10.1007/BF02868888

(72) Rusman, N. A. A. & Dahari, M. A review on the current progress of metal hydrides material for solid-state hydrogen storage applications. *International Journal of Hydrogen Energy* 41, 12108-12126 (**2016**). https://doi.org/10.1016/j.ijhydene.2016.05.244

(73) Wieckowski, A. *Fuel cell catalysis: a surface science approach*. (John Wiley & Sons, **2009**),

(74) Humphreys, J., Lan, R. & Tao, S. Development and Recent Progress on Ammonia Synthesis Catalysts for Haber–Bosch Process. *Advanced Energy and Sustainability Research* 2 (**2020**). https://doi.org/10.1002/aesr.202000043

(75) Ye, R.-P., Ding, J., Gong, W., Argyle, M. D., Zhong, Q., Wang, Y., Russell, C. K., Xu, Z., Russell, A. G., Li, Q., Fan, M. & Yao, Y.-G. CO2 hydrogenation to high-value products via heterogeneous catalysis. *Nature Communications* 10, 5698 (**2019**). https://doi.org/10.1038/s41467-019-13638-9

(76) Behm, R. J., Penka, V., Cattania, M. G., Christmann, K. & Ertl, G. Evidence for ''subsurface'' hydrogen on Pd(110): An intermediate between chemisorbed and dissolved species. *The Journal of Chemical Physics* 78, 7486-7490 (**1983**). https://doi.org/10.1063/1.444739

(77) Wicke, E., Brodowsky, H. & Züchner, H. in *Hydrogen in Metals II: Application-Oriented Properties* (eds Georg Alefeld & Johann Völkl) 73-155 (Springer Berlin Heidelberg, **1978**).https://doi.org/10.1007/3-540-08883-0_19

(78) Manchester, A. S.-M. a. F. D. The H-Mg (Hydrogen-Magnesium) System. *Bulletin of Alloy Phase Diagrams* 8 (**1987**). https://doi.org/10.1007/BF02893152

(79) Sieverts, A. Absorption of gases by metals. *Zeitschrift für Metallkunde* 21, 37-46 (**1929**).

(80) Darmadi, I. *Polymer-Nanoparticle Hybrid Materials for Plasmonic Hydrogen Detection* Ph.D. thesis, Chalmers Tekniska Hogskola (Sweden), (**2021**).

(81) Brokate, M. & Sprekels, J. in *Hysteresis and Phase Transitions* (eds Martin Brokate & Jürgen Sprekels) 150-174 (Springer New York, **1996**).https://doi.org/10.1007/978-1-4612-4048-8_5

(82) Flanagan, T. B. & Oates, W. A. The effect of hysteresis on the phase diagram of Pd-H. *Journal of the Less Common Metals* 92, 131-142 (**1983**). https://doi.org/10.1016/0022-5088(83)90234-5

(83) Lynch, J. F., Clewley, J. D., Curran, T. & Flanagan, T. B. The effect of the α-β phase change on the α phase solubility of hydrogen in palladium. *Journal of the Less Common Metals* 55, 153-163 (**1977**). https://doi.org/10.1016/0022-5088(77)90187-4

(84) Baldi, A., Narayan, T. C., Koh, A. L. & Dionne, J. A. In situ detection of hydrogen-induced phase transitions in individual palladium

nanocrystals. *Nat Mater* 13, 1143-1148 (**2014**).
https://doi.org/10.1038/nmat4086

(85) Griessen, R., Strohfeldt, N. & Giessen, H. Thermodynamics of the hybrid interaction of hydrogen with palladium nanoparticles. *Nat Mater* 15, 311-317 (**2016**). https://doi.org/10.1038/nmat4480

(86) Schwarz, R. B. & Khachaturyan, A. G. Thermodynamics of open two-phase systems with coherent interfaces. *Phys Rev Lett* 74, 2523-2526 (**1995**). https://doi.org/10.1103/PhysRevLett.74.2523

(87) Wagner, S., Uchida, H., Burlaka, V., Vlach, M., Vlcek, M., Lukac, F., Cizek, J., Baehtz, C., Bell, A. & Pundt, A. Achieving coherent phase transition in palladium–hydrogen thin films. *Scripta Materialia* 64, 978-981 (**2011**). https://doi.org/10.1016/j.scriptamat.2011.02.004

(88) Langhammer, C., Zhdanov, V. P., Zoric, I. & Kasemo, B. Size-dependent kinetics of hydriding and dehydriding of Pd nanoparticles. *Phys Rev Lett* 104, 135502 (**2010**).
https://doi.org/10.1103/PhysRevLett.104.135502

(89) Alekseeva, S., Strach, M., Nilsson, S., Fritzsche, J., Zhdanov, V. P. & Langhammer, C. Grain-growth mediated hydrogen sorption kinetics and compensation effect in single Pd nanoparticles. *Nat Commun* 12, 5427 (**2021**). https://doi.org/10.1038/s41467-021-25660-x

(90) Delmelle, R., Amin-Ahmadi, B., Sinnaeve, M., Idrissi, H., Pardoen, T., Schryvers, D. & Proost, J. Effect of structural defects on the hydriding kinetics of nanocrystalline Pd thin films. *International Journal of Hydrogen Energy* 40, 7335-7347 (**2015**).
https://doi.org/10.1016/j.ijhydene.2015.04.017

(91) Alekseeva, S., Fanta, A., Iandolo, B., Antosiewicz, T. J., Nugroho, F. A. A., Wagner, J. B., Burrows, A., Zhdanov, V. P. & Langhammer, C. Grain boundary mediated hydriding phase transformations in individual polycrystalline metal nanoparticles. *Nat Commun* 8, 1084 (**2017**).
https://doi.org/10.1038/s41467-017-00879-9

(92) Chattopadhyay, K. & Goswami, R. Melting and superheating of metals and alloys. *Progress in Materials Science* 42, 287-300 (**1997**).
https://doi.org/10.1016/S0079-6425(97)00030-3

(93) Koch, C., Cavin, O., McKamey, C. & Scarbrough, J. Preparation of ‘‘amorphous’’Ni60Nb40 by mechanical alloying. *Applied Physics Letters* 43, 1017-1019 (**1983**).

(94) Krutenat, R. C. & Gesick, W. R. Vapor Deposition by Liquid Phase Sputtering. *Journal of Vacuum Science and Technology* 7, S40-S44 (**1970**). https://doi.org/10.1116/1.1315917

(95) Birchenall, C. E. The mechanism of diffusion in the solid state. *Metallurgical Reviews* 3, 235-277 (**1958**). https://doi.org/10.1179/mtlr.1958.3.1.235

(96) Balogh, Z. & Schmitz, G. in *Physical Metallurgy* 387-559 (**2014**).https://doi.org/10.1016/b978-0-444-53770-6.00005-8

(97) Mehl, R. F. Rates of Diffusion in Solid Alloys. *Journal of Applied Physics* 8, 174-185 (**1937**). https://doi.org/10.1063/1.1710280

(98) Hughes, R., Schubert, W., Zipperian, T., Rodriguez, J. & Plut, T. Thin-film palladium and silver alloys and layers for metal-insulator-semiconductor sensors. *Journal of Applied Physics* 62, 1074-1083 (**1987**). https://doi.org/10.1063/1.339738

(99) Sakamoto, Y., Chen, F. L., Ura, M. & Flanagan, T. B. Thermodynamic Properties for Solution of Hydrogen in Palladium-Based Binary Alloys. *Berichte der Bunsengesellschaft für physikalische Chemie* 99, 807-820 (**1995**). https://doi.org/10.1002/bbpc.19950990605

(100) Noh, H., Luo, S., Wang, D., Clewley, J. D. & Flanagan, T. B. The effects of hydriding-dehydriding cycles on the plateau pressures and van't Hoff plots for Pd⊠Ni alloys. *Journal of Alloys and Compounds* 218, 139-142 (**1995**). https://doi.org/10.1016/0925-8388(94)01404-3

(101) Wadell, C., Nugroho, F. A., Lidstrom, E., Iandolo, B., Wagner, J. B. & Langhammer, C. Hysteresis-free nanoplasmonic Pd-Au alloy hydrogen sensors. *Nano Lett* 15, 3563-3570 (**2015**). https://doi.org/10.1021/acs.nanolett.5b01053

(102) Nugroho, F. A. A., Darmadi, I., Zhdanov, V. P. & Langhammer, C. Universal Scaling and Design Rules of Hydrogen-Induced Optical Properties in Pd and Pd-Alloy Nanoparticles. *ACS Nano* 12, 9903-9912 (**2018**). https://doi.org/10.1021/acsnano.8b02835

(103) Zhao, Z., Sevryugina, Y., Carpenter, M. A., Welch, D. & Xia, H. All-Optical Hydrogen-Sensing Materials Based on Tailored Palladium Alloy Thin Films. *Analytical Chemistry* 76, 6321-6326 (**2004**). https://doi.org/10.1021/ac0494883

(104) Allison, E. G. & Bond, G. C. The Structure and Catalytic Properties of Palladium-Silver and Palladium-Gold Alloys. *Catalysis Reviews* 7, 233-289 (**1972**). https://doi.org/10.1080/01614947208062259

(105) Okamoto, H. & Massalski, T. B. The Au−Pd (Gold-Palladium) system. *Bulletin of Alloy Phase Diagrams* 6, 229-235 (**1985**). https://doi.org/10.1007/BF02880404

(106) Namba, K., Ogura, S., Ohno, S., Di, W., Kato, K., Wilde, M., Pletikosic, I., Pervan, P., Milun, M. & Fukutani, K. Acceleration of hydrogen absorption by palladium through surface alloying with gold. *Proc Natl Acad Sci U S A* 115, 7896-7900 (**2018**). https://doi.org/10.1073/pnas.1800412115

(107) Conrad, H., Ertl, G., Koch, J. & Latta, E. E. Adsorption of CO on Pd single crystal surfaces. *Surface Science* 43, 462-480 (**1974**). https://doi.org/10.1016/0039-6028(74)90270-2

(108) Bradshaw, A. M. The structure and chemistry of adsorbed carbon monoxide. *Surface Science* 80, 215-225 (**1979**). https://doi.org/10.1016/0039-6028(79)90680-0

(109) Fonseca, S., Maia, G. & Pinto, L. M. C. Hydrogen adsorption in the presence of coadsorbed CO on Pd(111). *Electrochemistry Communications* 93, 100-103 (**2018**). https://doi.org/10.1016/j.elecom.2018.06.016

(110) Wong, Y. T. & Hoffmann, R. Chemisorption of carbon monoxide on three metal surfaces: nickel (111), palladium (111), and platinum (111): a comparative study. *The Journal of Physical Chemistry* 95, 859-867 (**1991**). https://doi.org/10.1021/j100155a069

(111) O'Brien, C. P. & Lee, I. C. The interaction of CO with PdCu hydrogen separation membranes: An operando infrared spectroscopy study. *Catalysis Today* 336, 216-222 (**2019**). https://doi.org/10.1016/j.cattod.2017.09.039

(112) Sakong, S., Mosch, C. & Gross, A. CO adsorption on Cu-Pd alloy surfaces: ligand versus ensemble effects. *Phys Chem Chem Phys* 9, 2216-2225 (**2007**). https://doi.org/10.1039/b615547b

(113) Subramanian, P. R. & Laughlin, D. E. Cu-Pd (Copper-Palladium). *Journal of Phase Equilibria* 12, 231-243 (**1991**). https://doi.org/10.1007/BF02645723

(114) Burch, R. & Buss, R. G. Absorption of hydrogen by palladium–copper alloys. Part 1.—Experimental measurements. *Journal of the Chemical Society, Faraday Transactions 1: Physical Chemistry in Condensed Phases* 71, 913-921 (**1975**). https://doi.org/10.1039/F19757100913

(115) Bannenberg, L. J., Boelsma, C., Asano, K., Schreuders, H. & Dam, B. Metal Hydride Based Optical Hydrogen Sensors. *Journal of the Physical Society of Japan* 89 (**2020**). https://doi.org/10.7566/jpsj.89.051003

(116) Semerikova, A., Chanyshev, A. D., Glazyrin, K., Pakhomova, A., Kurnosov, A., Litasov, K., Dubrovinsky, L. & Rashchenko, S. Face-Centered Cubic Platinum Hydride and Phase Diagram of PtH. *European Journal of Inorganic Chemistry* 2020, 4532-4538 (**2020**). https://doi.org/10.1002/ejic.202000849

(117) Kim, D. Y., Scheicher, R. H., Pickard, C. J., Needs, R. J. & Ahuja, R. Predicted formation of superconducting platinum-hydride crystals under pressure in the presence of molecular hydrogen. *Physical review letters* 107 11, 117002 (**2011**). https://doi.org/10.1103/PhysRevLett.107.117002

(118) Antonov, V. E., Antonova, T. E., Belash, I. T., Ponyatovskii, E. G. & Rashupkin, V. I. The Pd-Pt-H system: Phase transformations at high pressure and superconductivity. *physica status solidi (a)* 78, 137-146 (**1983**). https://doi.org/10.1002/pssa.2210780116

(119) Christmann, K., Ertl, G. & Pignet, T. Adsorption of hydrogen on a Pt(111) surface. *Surface Science* 54, 365-392 (**1976**). https://doi.org/10.1016/0039-6028(76)90232-6

(120) Christmann, K. & Ertl, G. Interaction of hydrogen with Pt(111): The role of atomic steps. *Surface Science* 60, 365-384 (**1976**). https://doi.org/10.1016/0039-6028(76)90322-8

(121) Gland, J. L., Sexton, B. A. & Fisher, G. B. Oxygen interactions with the Pt(111) surface. *Surface Science* 95, 587-602 (**1980**). https://doi.org/10.1016/0039-6028(80)90197-1

(122) van Lent, R., Auras, S. V., Cao, K., Walsh, A. J., Gleeson, M. A. & Juurlink, L. B. F. Site-specific reactivity of molecules with surface defects—the case of H2 dissociation on Pt. *Science* 363, 155-157 (**2019**). https://doi.org/doi:10.1126/science.aau6716

(123) Fair, J. A. & Madix, R. J. A molecular beam investigation of the oxidation of CO on Pt[9(111)×(100)]. *The Journal of Chemical Physics* 73, 3486-3491 (**1980**). https://doi.org/10.1063/1.440501

(124) Qiao, B., Wang, A., Yang, X., Allard, L. F., Jiang, Z., Cui, Y., Liu, J., Li, J. & Zhang, T. Single-atom catalysis of CO oxidation using Pt1/FeOx. *Nature Chemistry* 3, 634-641 (**2011**). https://doi.org/10.1038/nchem.1095

(125) Mergler, Y. J., van Aalst, A., van Delft, J. & Nieuwenhuys, B. E. CO oxidation over promoted Pt catalysts. *Applied Catalysis B:*

Environmental 10, 245-261 (**1996**). https://doi.org/10.1016/S0926-3373(96)00017-3

(126) Gorte, R., Schmidt, L. & Gland, J. L. Binding states and decomposition of NO on single crystal planes of Pt. *Surface Science* 109, 367-380 (**1981**). https://doi.org/10.1016/0039-6028(81)90494-5

(127) Katsounaros, I., Figueiredo, M. C., Chen, X., Calle-Vallejo, F. & Koper, M. T. M. Structure- and Coverage-Sensitive Mechanism of NO Reduction on Platinum Electrodes. *ACS Catalysis* 7, 4660-4667 (**2017**). https://doi.org/10.1021/acscatal.7b01069

(128) Vít, Z. & Zdražil, M. Simultaneous hydrodenitrogenation of pyridine and hydrodesulfurization of thiophene over carbon-supported platinum metal sulfides. *Journal of Catalysis* 119, 1-7 (**1989**). https://doi.org/10.1016/0021-9517(89)90129-2

(129) Pessayre, S., Geantet, C., Bacaud, R., Vrinat, M., N'Guyen, T. S., Soldo, Y., Hazemann, J. L. & Breysse, M. Platinum Doped Hydrotreating Catalysts for Deep Hydrodesulfurization of Diesel Fuels. *Industrial & Engineering Chemistry Research* 46, 3877-3883 (**2007**). https://doi.org/10.1021/ie060932x

(130) Marković, N. M., Schmidt, T. J., Stamenković, V. & Ross, P. N. Oxygen Reduction Reaction on Pt and Pt Bimetallic Surfaces: A Selective Review. *Fuel Cells* 1, 105-116 (**2001**). https://doi.org/10.1002/1615-6854(200107)1:2<105::Aid-fuce105>3.0.Co;2-9

(131) Fassihi, M., Zhdanov, V. P., Rinnemo, M., Keck, K. E. & Kasemo, B. A Theoretical and Experimental Study of Catalytic Ignition in the Hydrogen-Oxygen Reaction on Platinum. *Journal of Catalysis* 141, 438-452 (**1993**). https://doi.org/10.1006/jcat.1993.1153

(132) Sheng, W., Gasteiger, H. A. & Shao-Horn, Y. Hydrogen Oxidation and Evolution Reaction Kinetics on Platinum: Acid vs Alkaline Electrolytes. *Journal of The Electrochemical Society* 157, B1529 (**2010**). https://doi.org/10.1149/1.3483106

(133) Chen, Z., Hu, K., Yang, P., Fu, X., Wang, Z., Yang, S., Xiong, J., Zhang, X., Hu, Y. & Gu, H. Hydrogen sensors based on Pt-decorated SnO2 nanorods with fast and sensitive room-temperature sensing performance. *Journal of Alloys and Compounds* 811, 152086-152086 (**2019**). https://doi.org/10.1016/J.JALLCOM.2019.152086

(134) Gottam, S. R., Tsai, C. T., Wang, L. W., Wang, C. T., Lin, C. C. & Chu, S. Y. Highly sensitive hydrogen gas sensor based on a MoS2-Pt

nanoparticle composite. *Applied Surface Science* 506, 144981-144981 (**2020**). https://doi.org/10.1016/j.apsusc.2019.144981

(135) Rajoua, K., Baklouti, L. & Favier, F. Platinum for hydrogen sensing: surface and grain boundary scattering antagonistic effects in Pt@Au core-shell nanoparticle assemblies prepared using a Langmuir-Blodgett method. *Phys Chem Chem Phys* 20, 383-394 (**2017**). https://doi.org/10.1039/c7cp06645g

(136) Cao, F., Zhao, P., Wang, Z., Zhang, X., Zheng, H., Wang, J., Zhou, D., Hu, Y. & Gu, H. An Ultrasensitive and Ultraselective Hydrogen Sensor Based on Defect-Dominated Electron Scattering in Pt Nanowire Arrays. *Advanced Materials Interfaces* 6 (**2018**). https://doi.org/10.1002/admi.201801304

(137) Mu, X., Liu, S., Chen, L. & Mu, S. Alkaline Hydrogen Oxidation Reaction Catalysts: Insight into Catalytic Mechanisms, Classification, Activity Regulation and Challenges. *Small Structures* 4 (**2023**). https://doi.org/10.1002/sstr.202200281

(138) Nolan, P. D., Lutz, B. R., Tanaka, P. L., Davis, J. E. & Mullins, C. B. Molecularly chemisorbed intermediates to oxygen adsorption on Pt(111): A molecular beam and electron energy-loss spectroscopy study. *The Journal of Chemical Physics* 111, 3696-3704 (**1999**). https://doi.org/10.1063/1.479649

(139) Hellsing, B., Kasemo, B. & Zhdanov, V. P. Kinetics of the hydrogen-oxygen reaction on platinum. *Journal of Catalysis* 132, 210-228 (**1991**). https://doi.org/10.1016/0021-9517(91)90258-6

(140) Borodin, D., Schwarzer, M., Hahn, H. W., Fingerhut, J., Wang, Y., Auerbach, D. J., Guo, H., Schroeder, J., Kitsopoulos, T. N. & Wodtke, A. M. The puzzle of rapid hydrogen oxidation on Pt(111). *Molecular Physics* 119, e1966533 (**2021**). https://doi.org/10.1080/00268976.2021.1966533

(141) Wahnström, T., Fridell, E., Ljungström, S., Hellsing, B., Kasemo, B. & Rosén, A. Determination of the activation energy for OH desorption in the H2 + O2 reaction on Polycrystalline Platinum. *Surface Science* 223, L905-L912 (**1989**). https://doi.org/10.1016/0039-6028(89)90662-6

(142) El-Shafie, M. Hydrogen production by water electrolysis technologies: A review. *Results in Engineering* 20, 101426 (**2023**). https://doi.org/10.1016/j.rineng.2023.101426

(143) Ji, M. & Wei, Z. A Review of Water Management in Polymer Electrolyte Membrane Fuel Cells. *Energies* 2, 1057-1106 (**2009**). https://doi.org/10.3390/en20401057

(144) Meng, S., Wang, E. G. & Gao, S. Water adsorption on metal surfaces: A general picture from density functional theory studies. *Physical Review B* 69 (**2004**). https://doi.org/10.1103/PhysRevB.69.195404

(145) Thiel, P. A. & Madey, T. E. The interaction of water with solid surfaces: fundamental aspects. *Surface Science Reports* 7, 211-385 (**1987**). https://doi.org/10.1016/0167-5729(87)90001-X

(146) Anderson, A. B. Reactions and structures of water on clean and oxygen covered Pt(111) and Fe(100). *Surface Science* 105, 159-176 (**1981**). https://doi.org/10.1016/0039-6028(81)90154-0

(147) Cao, Y. & Chen, Z.-X. Theoretical studies on the adsorption and decomposition of H2O on Pd(111) surface. *Surface Science* 600, 4572-4583 (**2006**). https://doi.org/10.1016/j.susc.2006.07.028

(148) Ungerer, M. J., Santos-Carballal, D., Cadi-Essadek, A., van Sittert, C. G. C. E. & de Leeuw, N. H. Interaction of H2O with the Platinum Pt (001), (011), and (111) Surfaces: A Density Functional Theory Study with Long-Range Dispersion Corrections. *The Journal of Physical Chemistry C* 123, 27465-27476 (**2019**). https://doi.org/10.1021/acs.jpcc.9b06136

(149) Kolb, M. J., Calle-Vallejo, F., Juurlink, L. B. F. & Koper, M. T. M. Density functional theory study of adsorption of H2O, H, O, and OH on stepped platinum surfaces. *The Journal of Chemical Physics* 140 (**2014**). https://doi.org/10.1063/1.4869749

(150) Dekura, S., Kobayashi, H., Kusada, K. & Kitagawa, H. Hydrogen in Palladium and Storage Properties of Related Nanomaterials: Size, Shape, Alloying, and Metal-Organic Framework Coating Effects. *Chemphyschem* 20, 1158-1176 (**2019**). https://doi.org/10.1002/cphc.201900109

(151) Chernov, I. P., Koroteev, Y. M., Silkin, V. M. & Tyurin, Y. I. Evolution of the electron structure and excitation spectrum in palladium as a result of hydrogen absorption. *Doklady Physics* 53, 318-322 (**2008**). https://doi.org/10.1134/s1028335808060086

(152) McLachlan, D. S. & Burger, J. P. An analysis of the electrical conductivity of the two phase Pd Hx system. *Solid State Communications* 65, 159-161 (**1988**). https://doi.org/https://doi.org/10.1016/0038-1098(88)90678-3

(153) Sakamoto, Y., Takai, K., Takashima, I. & Imada, M. Electrical resistance measurements as a function of composition of palladium - hydrogen(deuterium) systems by a gas phase method. *Journal of Physics: Condensed Matter* 8, 3399 (**1996**). https://doi.org/10.1088/0953-8984/8/19/015

(154) Palm, K. J., Murray, J. B., Narayan, T. C. & Munday, J. N. Dynamic Optical Properties of Metal Hydrides. *ACS Photonics* 5, 4677-4686 (**2018**). https://doi.org/10.1021/acsphotonics.8b01243

(155) Rahm, J. M., Tiburski, C., Rossi, T. P., Nugroho, F. A. A., Nilsson, S., Langhammer, C. & Erhart, P. A Library of Late Transition Metal Alloy Dielectric Functions for Nanophotonic Applications. *Advanced Functional Materials* 30 (**2020**). https://doi.org/10.1002/adfm.202002122

(156) Nautiyal, T., Youn, S. J. & Kim, K. S. Effect of dimensionality on the electronic structure of Cu, Ag, and Au. *Physical Review B* 68 (**2003**). https://doi.org/10.1103/PhysRevB.68.033407

(157) Légaré, P. A theoretical study of H surface and subsurface species on Pt(1 1 1). *Surface Science* 559, 169-178 (**2004**). https://doi.org/10.1016/j.susc.2004.04.013

(158) Eslamibidgoli, M. J. & Eikerling, M. H. Atomistic Mechanism of Pt Extraction at Oxidized Surfaces: Insights from DFT. *Electrocatalysis* 7, 345-354 (**2016**). https://doi.org/10.1007/s12678-016-0313-2

(159) Hammer, B. & Nørskov, J. K. Electronic factors determining the reactivity of metal surfaces. *Surface Science* 343, 211-220 (**1995**). https://doi.org/10.1016/0039-6028(96)80007-0

(160) Vehviläinen, T., Salo, P., Ala-Nissila, T. & Ying, S. C. Electronic properties of H on vicinal Pt surfaces: First-principles study. *Physical Review B* 80 (**2009**). https://doi.org/10.1103/PhysRevB.80.035403

(161) Behafarid, F., Ono, L. K., Mostafa, S., Croy, J. R., Shafai, G., Hong, S., Rahman, T. S., Bare, S. R. & Cuenya, B. R. Electronic properties and charge transfer phenomena in Pt nanoparticles on gamma-Al2O3: size, shape, support, and adsorbate effects. *Phys Chem Chem Phys* 14, 11766-11779 (**2012**). https://doi.org/10.1039/c2cp41928a

(162) Hamada, I. & Morikawa, Y. Density-Functional Analysis of Hydrogen on Pt(111): Electric Field, Solvent, and Coverage Effects. *The Journal of Physical Chemistry C* 112, 10889-10898 (**2008**). https://doi.org/10.1021/jp8028787

(163) Maier, S. *Plasmonics: Fundamentals and Applications*. 1st edn, (Springer New York, NY, **2007**).https://doi.org/https://doi.org/10.1007/0-387-37825-1

(164) Barber, D. J. & Freestone, I. C. An investigation of the origin of the colour of the Lycurgus Cup by analytical transmission electron microscopy. *Archaeometry* 32, 33-45 (**1990**). https://doi.org/10.1111/j.1475-4754.1990.tb01079.x

(165) The Lycurgus Cup, *The Trustees of the British Museum,* <*https://www.britishmuseum.org/collection/object/H_1958-1202-1?selectedImageId=36154001*>*, (*Accessed on*:*February 12, 2025)

(166) Mayer, K. M. & Hafner, J. H. Localized surface plasmon resonance sensors. *Chem Rev* 111, 3828-3857 (**2011**). https://doi.org/10.1021/cr100313v

(167) Lee, K.-S. & El-Sayed, M. A. Gold and Silver Nanoparticles in Sensing and Imaging: Sensitivity of Plasmon Response to Size, Shape, and Metal Composition. *The Journal of Physical Chemistry B* 110, 19220-19225 (**2006**). https://doi.org/10.1021/jp062536y

(168) Hu, J., Wang, C., Yang, S., Zhou, F., Li, Z. & Kan, C. Surface plasmon resonance in periodic hexagonal lattice arrays of silver nanodisks. *Journal of Nanomaterials* 2013, 838191 (**2013**). https://doi.org/10.1155/2013/838191

(169) Zijlstra, P., Paulo, P. M. R. & Orrit, M. Optical detection of single non-absorbing molecules using the surface plasmon resonance of a gold nanorod. *Nature Nanotechnology* 7, 379-382 (**2012**). https://doi.org/10.1038/nnano.2012.51

(170) Chen, S., Svedendahl, M., Van Duyne, R. P. & Käll, M. Plasmon-Enhanced Colorimetric ELISA with Single Molecule Sensitivity. *Nano Letters* 11, 1826-1830 (**2011**). https://doi.org/10.1021/nl2006092

(171) Unser, S., Bruzas, I., He, J. & Sagle, L. Localized surface plasmon resonance biosensing: current challenges and approaches. *Sensors* 15, 15684-15716 (**2015**). https://doi.org/10.3390/s150715684

(172) Bingham, J. M., Anker, J. N., Kreno, L. E. & Van Duyne, R. P. Gas sensing with high-resolution localized surface plasmon resonance spectroscopy. *Journal of the American Chemical Society* 132, 17358-17359 (**2010**). https://doi.org/10.1021/ja1074272

(173) Syrenova, S., Wadell, C. & Langhammer, C. Shrinking-hole colloidal lithography: self-aligned nanofabrication of complex plasmonic nanoantennas. *Nano Lett* 14, 2655-2663 (**2014**). https://doi.org/10.1021/nl500514y

(174) Wadell, C., Antosiewicz, T. J. & Langhammer, C. Optical absorption engineering in stacked plasmonic Au-SiO(2)-Pd nanoantennas. *Nano Lett* 12, 4784-4790 (**2012**). https://doi.org/10.1021/nl3022187

(175) Dahlin, A. B., Tegenfeldt, J. O. & Höök, F. Improving the Instrumental Resolution of Sensors Based on Localized Surface Plasmon

Resonance. *Analytical Chemistry* 78, 4416-4423 (**2006**). https://doi.org/10.1021/ac0601967

(176) Brauns, E., Morsbach, E., Schnurpfeil, G., Bäumer, M. & Lang, W. A miniaturized catalytic gas sensor for hydrogen detection based on stabilized nanoparticles as catalytic layer. *Sensors and Actuators B: Chemical* 187, 420-425 (**2013**). https://doi.org/10.1016/j.snb.2013.01.037

(177) Brauns, E., Morsbach, E., Kunz, S., Bäumer, M. & Lang, W. A fast and sensitive catalytic gas sensors for hydrogen detection based on stabilized nanoparticles as catalytic layer. *Sensors and Actuators, B: Chemical* 193, 895-903 (**2014**). https://doi.org/10.1016/j.snb.2013.11.048

(178) Turing, A. M. I.—Computing Machinery and Intelligence. *Mind* LIX, 433-460 (**1950**). https://doi.org/10.1093/mind/LIX.236.433

(179) LeCun, Y., Boser, B., Denker, J. S., Henderson, D., Howard, R. E., Hubbard, W. & Jackel, L. D. Backpropagation Applied to Handwritten Zip Code Recognition. *Neural Computation* 1, 541-551 (**1989**). https://doi.org/10.1162/neco.1989.1.4.541

(180) Krizhevsky, A., Sutskever, I. & Hinton, G. E. Imagenet classification with deep convolutional neural networks. *Communications of the ACM* 60, 84-90 (**2017**). https://doi.org/10.1145/3065386

(181) Kasneci, E., Sessler, K., Küchemann, S., Bannert, M., Dementieva, D., Fischer, F., Gasser, U., Groh, G., Günnemann, S., Hüllermeier, E., Krusche, S., Kutyniok, G., Michaeli, T., Nerdel, C., Pfeffer, J., Poquet, O., Sailer, M., Schmidt, A., Seidel, T., Stadler, M., Weller, J., Kuhn, J. & Kasneci, G. ChatGPT for good? On opportunities and challenges of large language models for education. *Learning and Individual Differences* 103, 102274 (**2023**). https://doi.org/10.1016/j.lindif.2023.102274

(182) Enjellina, Beyan, E. V. P. & Anastasya Gisela Cinintya, R. A Review of AI Image Generator: Influences, Challenges, and Future Prospects for Architectural Field. *Journal of Artificial Intelligence in Architecture* 2, 53-65 (**2023**). https://doi.org/10.24002/jarina.v2i1.6662

(183) Mika, W. The Emergence of Deepfake Technology: A Review. *Technology Innovation Management Review* 9 (**2019**). https://doi.org/10.22215/timreview/1282

(184) Bachute, M. R. & Subhedar, J. M. Autonomous Driving Architectures: Insights of Machine Learning and Deep Learning Algorithms. *Machine Learning with Applications* 6, 100164 (**2021**). https://doi.org/10.1016/j.mlwa.2021.100164

(185) Suganyadevi, S., Seethalakshmi, V. & Balasamy, K. A review on deep learning in medical image analysis. *International Journal of Multimedia Information Retrieval* 11, 19-38 (**2022**). https://doi.org/10.1007/s13735-021-00218-1

(186) Jumper, J., Evans, R., Pritzel, A., Green, T., Figurnov, M., Ronneberger, O., Tunyasuvunakool, K., Bates, R., Žídek, A., Potapenko, A., Bridgland, A., Meyer, C., Kohl, S. A. A., Ballard, A. J., Cowie, A., Romera-Paredes, B., Nikolov, S., Jain, R., Adler, J., Back, T., Petersen, S., Reiman, D., Clancy, E., Zielinski, M., Steinegger, M., Pacholska, M., Berghammer, T., Bodenstein, S., Silver, D., Vinyals, O., Senior, A. W., Kavukcuoglu, K., Kohli, P. & Hassabis, D. Highly accurate protein structure prediction with AlphaFold. *Nature* 596, 583-589 (**2021**). https://doi.org/10.1038/s41586-021-03819-2

(187) Carrasco-Davis, R., Cabrera-Vives, G., Förster, F., Estévez, P. A., Huijse, P., Protopapas, P., Reyes, I., Martínez-Palomera, J. & Donoso, C. Deep Learning for Image Sequence Classification of Astronomical Events. *Publications of the Astronomical Society of the Pacific* 131, 108006 (**2019**). https://doi.org/10.1088/1538-3873/aaef12

(188) Bochenek, B. & Ustrnul, Z. Machine Learning in Weather Prediction and Climate Analyses—Applications and Perspectives. *Atmosphere* 13, 180 (**2022**). https://doi.org/10.3390/atmos13020180

(189) Choudhary, K., DeCost, B., Chen, C., Jain, A., Tavazza, F., Cohn, R., Park, C. W., Choudhary, A., Agrawal, A., Billinge, S. J. L., Holm, E., Ong, S. P. & Wolverton, C. Recent advances and applications of deep learning methods in materials science. *npj Computational Materials* 8, 59 (**2022**). https://doi.org/10.1038/s41524-022-00734-6

(190) Hellman, A. A brief overview of deep generative models and how they can be used to discover new electrode materials. *Current Opinion in Electrochemistry* 49, 101629 (**2025**). https://doi.org/10.1016/j.coelec.2024.101629

(191) Veritasium. The Most Useful Thing AI Has Ever Done. (**2025**). <https://www.youtube.com/watch?v=P_fHJIYENdI>.

(192) Samuel, A. L. Some Studies in Machine Learning Using the Game of Checkers. *IBM Journal of Research and Development* 3, 210-229 (**1959**). https://doi.org/10.1147/rd.33.0210

(193) Sze, V., Chen, Y.-H., Yang, T.-J. & Emer, J. S. Efficient Processing of Deep Neural Networks: A Tutorial and Survey. *Proceedings of the IEEE* 105, 2295-2329 (**2017**). https://doi.org/10.1109/jproc.2017.2761740

(194) Malcolm, K. & Casco-Rodriguez, J. A Comprehensive Review of Spiking Neural Networks: Interpretation, Optimization, Efficiency, and Best Practices. *ArXiv* abs/2303.10780 (**2023**). https://arxiv.org/abs/2303.10780

(195) Merolla, P. A., Arthur, J. V., Alvarez-Icaza, R., Cassidy, A. S., Sawada, J., Akopyan, F., Jackson, B. L., Imam, N., Guo, C., Nakamura, Y., Brezzo, B., Vo, I., Esser, S. K., Appuswamy, R., Taba, B., Amir, A., Flickner, M. D., Risk, W. P., Manohar, R. & Modha, D. S. A million spiking-neuron integrated circuit with a scalable communication network and interface. *Science* 345, 668-673 (**2014**). https://doi.org/doi:10.1126/science.1254642

(196) Alom, M. Z., Taha, T. M., Yakopcic, C., Westberg, S., Sidike, P., Nasrin, M. S., Van Esesn, B. C., Awwal, A. A. S. & Asari, V. K. The history began from alexnet: A comprehensive survey on deep learning approaches. *arXiv preprint arXiv:1803.01164* (**2018**). https://arxiv.org/abs/1803.01164

(197) Li, Z., Liu, F., Yang, W., Peng, S. & Zhou, J. A Survey of Convolutional Neural Networks: Analysis, Applications, and Prospects. *IEEE Trans Neural Netw Learn Syst* 33, 6999-7019 (**2022**). https://doi.org/10.1109/TNNLS.2021.3084827

(198) Zhu, Y., Wang, M., Yin, X., Zhang, J., Meijering, E. & Hu, J. Deep Learning in Diverse Intelligent Sensor Based Systems. *Sensors (Basel)* 23 (**2022**). https://doi.org/10.3390/s23010062

(199) Grigorescu, S., Trasnea, B., Cocias, T. & Macesanu, G. A survey of deep learning techniques for autonomous driving. *Journal of Field Robotics* 37, 362-386 (**2020**). https://doi.org/https://doi.org/10.1002/rob.21918

(200) Wang, M. & Deng, W. Deep face recognition: A survey. *Neurocomputing* 429, 215-244 (**2021**). https://doi.org/10.1016/j.neucom.2020.10.081

(201) Fei, C., Liu, R., Li, Z., Wang, T. & Baig, F. N. in *Computational Intelligence in Healthcare* (eds Amit Kumar Manocha, Shruti Jain, Mandeep Singh, & Sudip Paul) 105-160 (Springer International Publishing, **2021**).https://doi.org/10.1007/978-3-030-68723-6_6

(202) Yuan, Q., Shen, H., Li, T., Li, Z., Li, S., Jiang, Y., Xu, H., Tan, W., Yang, Q., Wang, J., Gao, J. & Zhang, L. Deep learning in environmental remote sensing: Achievements and challenges. *Remote Sensing of Environment* 241, 111716 (**2020**). https://doi.org/10.1016/j.rse.2020.111716

(203) Cho, S. Y., Lee, Y., Lee, S., Kang, H., Kim, J., Choi, J., Ryu, J., Joo, H., Jung, H. T. & Kim, J. Finding Hidden Signals in Chemical Sensors Using Deep Learning. *Anal Chem* 92, 6529-6537 (**2020**). https://doi.org/10.1021/acs.analchem.0c00137

(204) Lin, X., Cheng, M., Chen, X., Zhang, J., Zhao, Y. & Ai, B. Unlocking Predictive Capability and Enhancing Sensing Performances of Plasmonic Hydrogen Sensors via Phase Space Reconstruction and Convolutional Neural Networks. *ACS Sens* 9, 3877-3888 (**2024**). https://doi.org/10.1021/acssensors.3c02651

(205) Van Houdt, G., Mosquera, C. & Nápoles, G. A review on the long short-term memory model. *Artificial Intelligence Review* 53, 5929-5955 (**2020**). https://doi.org/10.1007/s10462-020-09838-1

(206) Vaswani, A., Shazeer, N., Parmar, N., Uszkoreit, J., Jones, L., Gomez, A. N., Kaiser, Ł. & Polosukhin, I. Attention is all you need. *Advances in neural information processing systems* 30 (**2017**). https://proceedings.neurips.cc/paper_files/paper/2017/file/3f5ee243547dee91fbd053c1c4a845aa-Paper.pdf

(207) Islam, S., Elmekki, H., Elsebai, A., Bentahar, J., Drawel, N., Rjoub, G. & Pedrycz, W. A Comprehensive Survey on Applications of Transformers for Deep Learning Tasks. *ArXiv* abs/2306.07303 (**2023**). https://arxiv.org/abs/2306.07303

(208) T, T., Haryono, W., Zailani, A. U., Djaksana, Y. M., Rosmawarni, N. & Arianti, N. D. Transformers in Machine Learning: Literature Review. *Jurnal Penelitian Pendidikan IPA* 9, 604-610 (**2023**). https://doi.org/10.29303/jppipa.v9i9.5040

(209) Flanagan, T. B. in *Hydrides for Energy Storage* (eds A. F. Andresen & A. J. Maeland) 135-150 (Pergamon, **1978**).https://doi.org/10.1016/B978-0-08-022715-3.50019-9

(210) Ioffe, S. Batch normalization: Accelerating deep network training by reducing internal covariate shift. *arXiv preprint arXiv:1502.03167* (**2015**). https://arxiv.org/abs/1502.03167

(211) Srivastava, N., Hinton, G., Krizhevsky, A., Sutskever, I. & Salakhutdinov, R. Dropout: a simple way to prevent neural networks from overfitting. *The journal of machine learning research* 15, 1929-1958 (**2014**). http://jmlr.org/papers/v15/srivastava14a.html

(212) Fredriksson, H., Alaverdyan, Y., Dmitriev, A., Langhammer, C., Sutherland, D. S., Zäch, M. & Kasemo, B. Hole–Mask Colloidal

Lithography. *Advanced Materials* 19, 4297-4302 (**2007**). https://doi.org/10.1002/adma.200700680

(213) Ul-Hamid, A. *A beginners' guide to scanning electron microscopy*. Vol. 1 (Springer, **2018**),

(214) *Transmission Electron Microscope*, Encyclopædia Britannica <https://www.britannica.com/technology/transmission-electron-microscope#/media/1/602949/110686> (Accessed on: February 19, 2025).

(215) Grob, R. L. & Barry, E. F. *Modern practice of gas chromatography*. (John Wiley & Sons, **2004**),

(216) *Mass Spectrometry*, MKS Instruments <https://www.mks.com/n/mass-spectrometry> (Accessed on: February 21, 2025).